Development and application of field-based multiscale modeling techniques for optimizing the performance of polymer nanodevices

Dissertation
zur Erlangung
des Doktorgrades der Naturwissenschaften
(Dr. rer. nat.)
an der Fakultät für
-Chemie und Pharmazie-
der Universität Regensburg

vorgelegt von
Sergii Donets
aus Khust, Ukraine
April 2014

Dedicated to my parents, Elena and Sergey.

Die vorliegende Arbeit wurde in der Zeit von September 2010 bis April 2014 unter Anleitung von Herrn PD. Dr. Stephan A. Bäurle am Institut für Physikalische und Theoretische Chemie der Universität Regensburg angefertigt.

Promotionsgesuch eingereicht am: 23.04.2014
Tag des Kolloquiums: 27.05.2014

Prüfungsausschuss:
Prof. Dr. Arno Pfitzner (Vorsitzender)
PD. Dr. Stephan Bäurle
Prof. Dr. Bernhard Dick
Prof. Dr. Klaus Richter

Folgende Ergebnisse dieser Arbeit sind bereits veröffentlicht bzw. eingereicht worden:

1. A. Pershin, S. Donets und S. A. Baeurle, "A new multiscale modeling method for simulating the loss processes in polymer solar cell nanodevices" J. Chem. Phys. 136, 194102 (2012); doi: 10.1063/1.4712622

2. S. Donets, A. Pershin, M. J. A. Christlmaier und S. A. Baeurle, "A multiscale modeling study of loss processes in block-copolymer-based solar cell nanodevices" J. Chem. Phys. 138, 094901 (2013); doi: 10.1063/1.4792366

3. A. Pershin, S. Donets und S. A. Baeurle, "Performance enhancement of block-copolymer solar cells through tapering the donor-acceptor interface: A multiscale study" Polymer 55, 1507 (2014); doi: 10.1016/j.polymer.2014.01.052

4. A. Pershin, S. Donets und S. A. Baeurle, "Photocurrent contribution from inter-segmental mixing in donor-acceptor-type polymer solar cells: A theoretical study" eingereicht (2014)

Noch zu erwartende Publikationen aus der Doktorarbeit:

1. S. Donets, A. Pershin und S. A. Baeurle, "Optimizing and improving the performance of polymer solar cells by using a multiscale field-based simulation technique", in Vorbereitung

2. S. Donets, A. Pershin und S. A. Baeurle, "Simulating polymer solar cell nanodevices using cost-efficient multiscale parameterization", in Vorbereitung

Acknowledgments

First of all, I would like to thank my supervisor PD. Dr. Stephan Bäurle for his support, insight, useful comments, remarks and invaluable assistance. Furthermore, I would like to acknowledge the head of the chair Professor Dr. Bernhard Dick for providing a stimulating research environment and the facilities to complete my Ph.D. thesis. A special thanks goes to all the members of my research group, namely, Anton Pershin, Emanuel Peter, Ivan Stambolic and Martin Christlmaier, for help and support during this difficult time. I would also like to thank all the people from the chair for the support, invaluable comments and friendly discussions. I gratefully acknowledge the funding source, Deutsche Forschungsgemeinschaft (DFG) Grant No. BA 2256/3-1, that made my Ph.D. possible. Finally, I would like to express my deepest gratitude to my family and my beloved Alexandra Morozova for their faithful support, encouragement and infinite love. Thank you!

Contents

Chapter 1

Introduction

1.1 Organic electronics

Organic devices have attracted considerable attention in the past decade due to their great perspective in light weight, flexible and large area applications and the low fabrication costs [1, 2]. There are many different fields, in which they might be competitive with silicon technology, increasing their suitability for commercial applications [1] and, thus, their value for modern societies, like in the field of energy, information and communication [3]. Examples of organic electronic devices include organic thin-film transistors (OTFT), organic light-emitting diodes (OLED), organic photovoltaics (OPV), radio-frequency identification (RFID), nano-capacitors, sensors, memories, and more [1, 3]. The number of applications continue to grow as the technology mature and as the global challenges require more sophisticated electronic devices. For instance, the OPV technology has generated significant interest in the last few years, due to the foreseeable shortage of fossil fuels as well as the necessity of limiting CO_2 emission [4]. However, it is worth noting that the OPV devices differ substantially from their inorganic counterparts in their operation principles, as well as in their methods of production [4]. A major advantage of OPVs is that they can be fabricated using simple and low-cost production procedures, such as spin-coating, evaporation and printing techniques [3]. Moreover, their light weight and mechanical flexibility confer them the potential to be easily integrable within consumer electronic devices, as illustrated in Fig. 1.1 [2, 4]. For this purpose, technologies such as roll-to-roll printing or spray coating technique, have recently been devised and prove to be useful for depositing OPV materials on various kind of substrates such as plastic, glass and others [3].

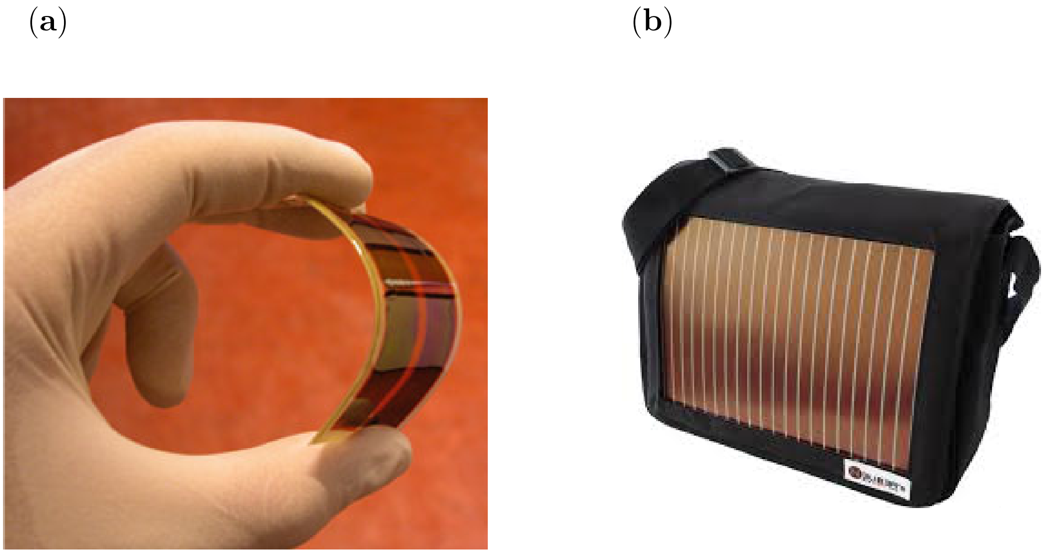

Figure 1.1: (a) Organic solar cell printed on a flexible plastic substrate (reproduced from [4]). (b) Plastic solar panel integrated into a bag for powering consumer electronic devices (Neuber's Energy Sun-Bag).

1.2 Organic solar cells: problems and perspectives

Converting solar energy into electricity is one of the most important research challenges nowadays. Good efficiencies have already been achieved by using inorganic solar cells. For instance, an efficiency of 25 % has been realized with crystalline silicon solar cells, while a five junction cell of GaAs/InP has provided a value of 38.8 % [5]. However, a problem of latter examples is that they are very expensive in terms of both materials and techniques [6]. As an alternative, organic-based photovoltaics represent a potentially cheap and easily handable technology. Unfortunately, to this day the efficiency of OPV cells is still significantly lower compared to inorganic PV cells [6]. In order to enhance their performance, new materials with low band gap and device architectures have to be developed. The low power conversion efficiencies are mainly attributed to loss phenomena occurring during the photovoltaic process, such as photon loss, exciton loss and charge-carrier loss [7].

Nowadays, a large variety of experimental tools are available for characterizing the structure and measuring the efficiency of OPV devices. For instance, the grazing incidence X-ray scattering (GIXS), to characterize the morphology of the active layer, in combination with space-charge limited-current-measurement technique, to characterize the charge transport in the device, can provide useful information about morphology and electronic structure of polymer molecules in bulk heterojunction solar cells [8]. Another technique, the time-resolved electrostatic force microscopy (EFM) enables the measurement of photoexcited charge creation in organic thin films with a spatial resolution better than 100 nm [132]. These results have been found to correlate with the external quantum efficiencies (EQE), in case of a series of polymer blends, composed of poly(9,9dioctylfluorene-co-bis-N,N-(4-butylphenyl)-bis-N,N-phenyl-1,4-phenylenediamide) PFB and poly(9,9-dioctyl-co-benzo- thiadiazole) F8BT [132]. Moreover, it has been concluded from these experimental investigations that the domain composition of the PFB- and F8BT-phases is of crucial importance for optimizing charge-carrier transport and recombination rates within these domains. Thus, we see that, obtaining more detailed information about the local morphological characteristics of the active layer can help to improve the performance of OPV devices. However, experimentally it is difficult to distinguish between the different loss phenomena occurring during the photovoltaic process and to assess the impact of morphology and chemical details on them [118]. In this regard computer simulation techniques can contribute to a better understanding of the physical processes underlying the operation of OPV devices and support experimental investigations.

A first attempt to gain some insight into the relationship between the device morphology of an organic bulk heterojunction solar cell and its internal quantum efficiency (IQE) has been made by Watkins *et al.* [121], who proposed a dynamic Monte Carlo (DMC) model that treats exciton diffusion and charge transport in mixed donor/acceptor (D/A) structures. They have considered both disordered and ordered morphologies with different scale of phase separation and found that at an intermediate scale of phase separation a peak in the IQE is observed, which relates to an ideal compromise between exciton dissociation and charge transport. Moreover, they showed that the ordered checkered morphology exhibits a peak IQE, which is 1.5 times higher than the one of the disordered blend. In a subsequent work, Marsh *et al.* [118] have developed a DMC model, which enables to simulate dark injections at the electrodes. In this model they focused on the situation of charge separation and transport processes in organic nanostructures, but did not consider the exciton diffusion to the heterojunction. In other works, Meng *et al.* [60] and Kimber *et al.* [41] designed DMC models where they took into account all the microscopic photovoltaic processes, including the description of exciton behavior, charge transport as well as dark current injections. Moreover, Yang *et al.* [9] have proposed a DMC model, which includes in addition the effects of optical interference, to study the influence of the nanostructure on the solar cell efficiency of a device composed of copper phthalocyanine (CuPc) and C_{60}. To calculate the distribution of exciton creations inside the device, i.e. the optical absorption distribution, they used the transfer-matrix method. This enabled them to calculate the absorption efficiencies for a series of heterojunctions and, thus, to evaluate their EQE's, which were in good agreement with experimentally measured values. A similar DMC model has also been employed by Yan *et al.* [116], to investigate the influence of annealing on the device performance of PFB/F8BT bilayers. They found that with increasing annealing temperature the device performance systematically decreases, which was mainly attributed to a deteriorated separation probability of interfacial electron-hole pairs due to an increased disorder at the D/A

interface. However, the main drawback of these approaches is that the underlying techniques used for morphological generation, such as the Ising model in conjunction with Kawasaki spin-exchange dynamics or the techniques for generating idealized morphologies [41, 60, 121], do not rely on realistic polymer models and, therefore, do not allow to introduce chemical details.

A standard approach to describe a complex polymer system in a realistic fashion by computational means is to use the molecular dynamics (MD) simulation technique at atomistic resolution. However, with this technique we can only consider relatively small systems with up to 10^6 atoms in the nanosecond up to sub-microsecond time range. In order to cope with the structural-dynamical evolution of large-scale polymer systems with up to several million of atoms the transformation from the conventional particle representation to field representation can be performed by using the Hubbard-Stratonovich transformation [77, 81]. For polymers the resulting field-theoretic partition function integral can effectively be approximated by the mean-field (MF) approximation. For instance, Buxton and Clarke, in order to predict the morphologies of a diblock-copolymer system, used the Flory-Huggins Cahn-Hilliard model, which relies on the MF approximation [10]. To simulate the photovoltaic response of their devices, they utilized a two-dimensional drift-diffusion method. However, despite the low computational expense, this approach remains rather limited because it does not allow the explicit description of local particle processes, such as loss processes through charge recombination or accumulation at bottlenecks and dead-ends of the morphology. First achievements to overcome this problem have been realized in our previous work [69], where we developed a new multiscale algorithm to simulate the photovoltaic performance of DA-polymer blends, which makes use of either the time-dependent Ginzburg-Landau method (TDGL) or the self-consistent field theory (SCFT), to generate the morphologies, in conjunction with the DMC method, to mimic the elementary photovoltaic processes. In another work [115], which was carried out in our group, we introduced a new particle-based multiscale solar-cell algorithm, to take into account the chemical nature of the monomers quantum mechanically. This permitted us to study the influence of photodegradation of the F8BT monomers on the photovoltaic performance of PFB/F8BT-blend devices. Moreover, by comparing its results with the ones of a field-based solar cell algorithm, we have estimated the influence of the local segmental composition and chemical defects on the local photovoltaic properties of DA-polymer solar cells [115].

1.3 Scope of the thesis

The goal of this thesis is to develop and apply field-based multiscale modeling techniques, to better understand and improve the performance of nanodevices, used in optoelectronic applications. For this purpose, we will use the SCFT technique, to compute the polymeric morphologies, in combination with a suitable DMC algorithm, to simulate the photovoltaic processes. The application of this coupled multiscale approach will enable us to treat a large variety of polymer systems of large system size at low computational costs. To investigate the causes affecting the loss processes of elementary particles in block-copolymer systems with changing chemical characteristics and external conditions, such as the mechanical load, we will apply this DMC-SCFT method on systems composed of DA-diblock- and ADA-triblock-copolymers. Moreover, we will investigate the suitability of these polymer systems for the use as charge storage media by analyzing their charge storage capacity as well as charge loading/unloading behavior. To elucidate the external parameters influencing solar-cell efficiency, we will analyze the impact of post-production techniques, such as electric-field alignment and surface interaction optimization, on the photovoltaic performance of polymer solar cell (PSC) nanodevices. Furthermore, we will study the influence of impurity particles, which might result from the diffusion of electrode material into the active layer, on the stability and performance of diblock-copolymer solar cells. To investigate the effect of mixing of the D- and A-components on the exciton-dissociation and charge-transport efficiencies, we will extend our conventional DMC-SCFT approach, where the effect of mixing of the D- and A-components has been neglected, by introducing the composition dependence of the exciton-dissociation frequency and charge-transfer integrals into the algorithm. The new method will be called the parameterized field-based multiscale solar-cell algorithm. In addition, to evaluate the influence of chemical changes through degradation of the polymer structure on the efficiency of PSCs, we will perform parameterized field-based calculations by taking into account the effect of photo-oxidation of the fluorene moieties. Finally, to investigate the impact of the architecture and composition of the full nanodevice on its absorption efficiency and EQE, we will combine the parameterized field-based solar-cell algorithm with a modified version of the transfer-matrix method, which is used to determine the optical absorption distribution within the photoactive layer. The new method will be called the bulk heterojunction transfer matrix(BTM)-DMC-SCFT, which will enable us to take into account all major effects, affecting the performance of full nanodevices at moderate computational costs.

To attain these goals, this thesis has been organized in the following way. In Chapter 2, the SCFT technique is introduced, whereas in Chapter 3 an overview of basic working principles of organic solar cells as well as theories, describing the creation and transport of the elementary particles within the active layer of organic solar cells, is presented. In Chapter 4 a detailed description of the DMC algorithm is provided. Next, in Chapter 5 the loss phenomena of block-copolymer-based solar cells as well as their suitability to be used as charge storage media, are discussed in detail. Afterwards, in Chapter 6 possible ways for improving the photovoltaic performance as well as the influence of impurity particles on the stability and efficiency of polymer bulk heterojunctions are analyzed, whereas in Chapter 7 the influence of chemical details on photovoltaic performance is investigated. In Chapter 8 the results of full device calculations of polymer-based solar cells are presented and the thesis is completed with a summary and conclusions in Chapter 9.

Chapter 2

Self-consistent field theory

2.1 Ideal chain models

In this chapter we introduce the SCFT for computing the polymeric morphologies used within this thesis. In ideal chain models only short-range interactions are taken into account. Regardless of their particular form, all ideal chain models exhibit universal scaling properties [11]. One of the simplest ideal chain models is the lattice model, depicted in Fig. 2.1 (a). In this model a polymer chain is described by a set of inter-linked monomers, which are placed sequentially on the spatial lattice [12]. It is assumed that the lattice has a lattice constant b_0.

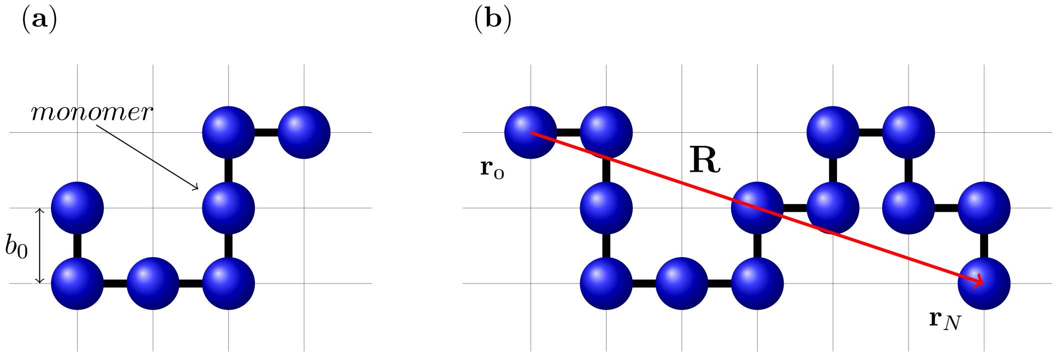

Figure 2.1: (a) Lattice model of polymers. (b) End-to-end vector (**R**) of a polymer chain.

One of the measures of the average size of a polymer chain can be characterized by the length of the vector **R** between two end monomers of the chain (see Fig. 2.1 (b)). The average end-to-end distance of an ideal or Gaussian chain scales with the degree of polymerization N as:

$$\sqrt{\left\langle |\mathbf{R}|^2 \right\rangle} = \sqrt{\left\langle |\mathbf{r}_N - \mathbf{r}_o|^2 \right\rangle} = b_0 N^{\nu}, \quad \nu = 1/2, \quad N \to \infty, \tag{2.1}$$

where each bond connecting the monomers is assumed to have a length b_0, whereas ν is a universal scaling exponent. The universality means that it does not depend on the chemical structure of the polymer chain and the level of coarse-graining. It is possible to show that the probability distribution of the end-to-end vector obeys the Gaussian distribution [12]:

$$P(\mathbf{R}) = \left(\frac{3}{2\pi N b_0^2}\right)^{3/2} \exp\left(-\frac{3\,|\mathbf{R}|^2}{2N b_0^2}\right). \tag{2.2}$$

Another important class of ideal chain models is a bead-spring model, which is a useful starting point for studying the physical properties of polymers on large scales. The transformation from lattice model to the bead-spring model can be done by grouping several monomers into larger units. The procedure, where the number of units is reduced from N monomers down to M segments is referred to as coarse-graining [14]. In such a way we are eliminating the information concerning microscopic degrees of freedom. When we define the coarse-grained segment the model parameters change as $N \to N/m = M$ and $b = \sqrt{m} b_0$. An important characteristic of the bead-spring model is that the probability distribution of the end-to-end vector of the coarse-grained polymer chain also obeys the Gaussian distribution, similar to Eq. (2.2). In statistics, this property is known as the central limiting theorem, which states that a sum of any large number of independent random variables tends to obey the Gaussian distribution [12, 14].

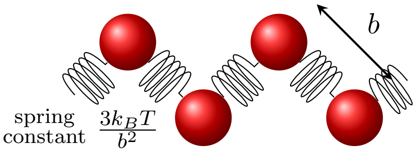

Figure 2.2: Bead-spring model.

In the bead-spring model the particles along the coarse-grained chain are considered to be connected by a harmonic spring (see Fig. 2.2), whose potential energy is given by [11, 12, 13]:

$$U_{bond}(\mathbf{b}) = \frac{3k_BT}{2b^2} |\mathbf{b}|^2 , \tag{2.3}$$

where $\mathbf{b}$ is a bond vector, k_B is Boltzmann's constant and T the system temperature. Since the spring constant depends on the temperature, the parameter b in this potential can be interpreted as an average of the square of the bond length:

$$\left\langle |\mathbf{b}|^2 \right\rangle = \frac{\int d\mathbf{b} \, |\mathbf{b}|^2 \exp\left[-\beta U_{bond}(\mathbf{b})\right]}{\int d\mathbf{b} \exp\left[-\beta U_{bond}(\mathbf{b})\right]} = b^2, \tag{2.4}$$

and, thus, b can be identified as the average bond length between the coarse-grained segments or the effective bond length.

Now, if we consider a linear chain composed of $N+1$ segments connected by the above mentioned bond potential, the Hamiltonian of this polymer chain can be written as [12]:

$$H = \frac{3k_BT}{2b^2} \sum_{i=0}^{N-1} |\mathbf{r}_i - \mathbf{r}_{i+1}|^2 + W(\mathbf{r}_0, \mathbf{r}_1, ..., \mathbf{r}_N) \equiv H_0 + W, \tag{2.5}$$

where $\mathbf{r}_i$ is a position vector of the i-th segment. The term denoted by H_0 is the Hamiltonian of an ideal chain, whereas the term W is the interaction potential, which depends on the chain conformation, including interactions between the segments or the effects of an external field.

2.2 Ideal chain statistics

As was already mentioned previously, in ideal chain models only the effects of segment connectivity are taken into account. In other words, an ideal chain has no long-range interactions between the segments. In this case, the Hamiltonian of the bead-spring model of the ideal chain is given by the first term of the right hand side of the Eq. (2.5) [12]:

$$H = H_0 = \frac{3k_B T}{2b^2} \sum_{i=0}^{N-1} |\mathbf{r}_i - \mathbf{r}_{i+\mathbf{1}}|^2 . \tag{2.6}$$

By using the canonical ensemble, where the total number of particles (N), the total volume (V) and the temperature (T) of the system are fixed, the probability of finding the conformation $\{\mathbf{r}_o, ..., \mathbf{r}_N\}$ of the ideal chain is defined as [12]:

$$P(\{\mathbf{r}_i\}) = \frac{1}{Z_0} \exp(-\beta H_0) = \frac{1}{Z_0} \exp\left(-\frac{3}{2b^2} \sum_{i=0}^{N-1} |\mathbf{r}_i - \mathbf{r}_{i+\mathbf{1}}|^2 \right), \tag{2.7}$$

where Z_0 is a partition function of the chain

$$Z_0 = \int d\mathbf{r}_o ... \int d\mathbf{r}_N \exp[-\beta H_0(\mathbf{r}_o, ..., \mathbf{r}_N)]. \tag{2.8}$$

After having performed the integration using the variable transformation from the position vectors $\{\mathbf{r}_i\}$ to the bond vectors $\{\mathbf{b}_i\}$ and the formula for the Gaussian integral, we obtain the following quantity of Z_0:

$$Z_0 = V \left(\frac{2\pi b^2}{3} \right)^{3N/2} , \tag{2.9}$$

which defines the total number of possible conformations of an ideal chain composed of $N + 1$ segments confined in a box with the volume V.

2.3 Path-integral formalism for an ideal chain

The distribution function of the chain conformation in Eq. (2.7) is a function in $3(N+1)$-dimensional configuration space. By using the path-integral formalism, it is possible to rewrite this function in a more tractable form. For the sake of simplicity, it is convenient to start from the lattice model of the polymer chain. In order to calculate the statistical weight, we consider a subchain, which is a part of the whole Gaussian chain. The end segments of this subchain, specified by the indices i' and i, are fixed at the sites $\mathbf{r}'$ and $\mathbf{r}$, respectively. The statistical weight of this subchain is defined as $Q(i', \mathbf{r}'; i, \mathbf{r})$ and, due to the connectivity, relates to $Q(i', \mathbf{r}'; i+1, \mathbf{r})$ through the following recurrence formula [15]:

$$Q(i', \mathbf{r}'; i+1, \mathbf{r}) = \frac{1}{z} \sum_{\mathbf{r}''} Q(i', \mathbf{r}'; i, \mathbf{r}''), \tag{2.10}$$

where z is a number of nearest neighbor sites and for a three dimensional lattice $z = 6$, whereas $\mathbf{r}''$ is one of the possible positions of the nearest neighbor sites to $\mathbf{r}$.

By going from the discretized expression of Eq. (2.10) to a continuum formula, we have to subtract $Q(i', \mathbf{r}'; i, \mathbf{r})$ from both sides of Eq. (2.10), to obtain the following expression:

$$Q(i', \mathbf{r}'; i+1, \mathbf{r}) - Q(i', \mathbf{r}'; i, \mathbf{r}) = \frac{1}{z} \sum_{\mathbf{r}''} Q(i', \mathbf{r}'; i, \mathbf{r}'') - Q(i', \mathbf{r}'; i, \mathbf{r}). \tag{2.11}$$

By afterwards taking the continuum limit, where $\Delta i \to 0$, the left hand side of Eq. (2.11) becomes a derivative of $Q(i', \mathbf{r}'; i, \mathbf{r})$ and the right hand side of Eq. (2.11) becomes the Laplacian. Then, replacing the discrete index i by a continuous parameter s and taking the limit $\Delta s \to 0$, Eq. (2.11) reduces to the three dimensional diffusion equation [15]:

$$\frac{\partial}{\partial s} Q(s', \mathbf{r}'; s, \mathbf{r}) = \frac{b_0^2}{6} \nabla^2 Q(s', \mathbf{r}'; s, \mathbf{r}), \tag{2.12}$$

where the parameter s corresponds to time and the factor before the Laplacian can be regarded as the diffusion constant $D = b_0^2/6$.

The solution of Eq. (2.12) under the initial condition that the end segment is fixed at the position $\mathbf{r}'$, is given by:

$$Q(s', \mathbf{r}'; s, \mathbf{r}) = \left(\frac{3}{2\pi |s-s'| b_0^2} \right)^{3/2} \exp\left(-\frac{3|\mathbf{r}-\mathbf{r}'|^2}{2|s-s'| b_0^2} \right), \tag{2.13}$$

which again proves that the ideal chain obeys Gaussian statistics [15].

2.4 The mean-field approximation

If a polymer chain possesses strong segment-segment interactions between different type of segments or segment-object interactions, the polymer chain is no longer an ideal Gaussian chain [15]. In such a situation we have to take into account the interaction term W in the Hamiltonian in Eq. (2.5). Due to the nonlinearity of this term, the probability distribution of the chain conformation can no longer be calculated exactly and we have to rely on the approximate theory [12], which is in our case the mean-field theory.

In a polymer melt, the interaction between segments is screened out as a result of both the incompressibility condition and the ability of polymer chains to interpenetrate one another. Due to the screening effect, the segment density fluctuations among the polymer chains are suppressed and each polymer chain in the polymer melt obeys ideal chain statistics. Mean-field approximation assumes that the correlations between a single chain, which is referred to as a tagged chain, and the other chains are neglected. Under this assumption, the conformation of the tagged chain can be approximated as an ideal chain in an external mean field $V(\mathbf{r})$ generated by the surrounding polymer chains (see Fig. 2.3 (b)).

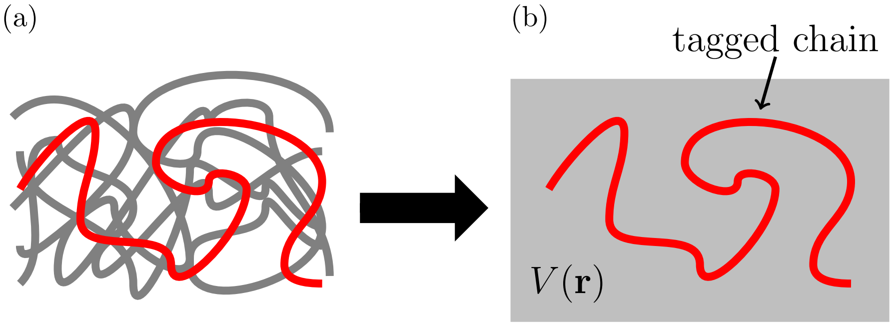

Figure 2.3: (a) An interacting many-chain system; (b) An ideal single chain in an external mean field $V(\mathbf{r})$ generated by the surrounding polymer chains.

By considering the system composed of several species, the mean-field acting on the tagged segment at position $\mathbf{r}$ is given by [12]:

$$V_K(\mathbf{r}) = k_B T \sum_{K'} \chi_{KK'} \phi_{K'}(\mathbf{r}) + \gamma(\mathbf{r}), \tag{2.14}$$

where $\chi_{KK'}$ is the Flory-Huggins interaction parameter between K- and K'-type segments, $\phi_{K'}(\mathbf{r})$ is the volume fraction of K-type segments at position $\mathbf{r}$, whereas $\gamma(\mathbf{r})$ is the constraint force due to external conditions.

In the next section we will describe the technique, which is used to calculate the equilibrium conformation of the tagged chain in an average external potential field.

2.5 Path-integral formalism for a chain in a mean field

In the mean-field approximation, which is also known as self-consistent field theory (SCFT), the conformations of the tagged chain are evaluated with the use of the path-integral technique, where the segment-segment and segment-object interactions are treated as external fields, acting on the ideal Gaussian chain [15].

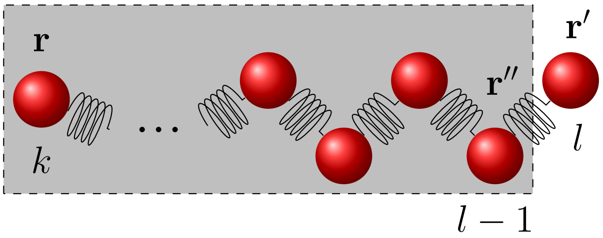

Figure 2.4: Subchain representation for the path-integral formalism. The subchain is splitted into two parts for the purpose of derivation of a recurrence formula.

As in section 2.3, we focus on the subchain, which is assumed to be in equilibrium in the self-consistent field $V(\mathbf{r})$ (see Fig. 2.4), whose end segments are specified by the indices k and l and are fixed at positions $\mathbf{r}$ and $\mathbf{r}'$, respectively. The whole polymer chain composed of K-type segments with indices $(0, ..., N)$. When we substitute the interaction between the tagged segment and the self-consistent field (Eq. (2.14)) instead of W in Eq. (2.5), then the Hamiltonian of this subchain is given by:

$$H = H_0 + W = \frac{3k_BT}{2b^2} \sum_{i=k}^{l-1} |\mathbf{r}_i - \mathbf{r}_{i+1}|^2 + \sum_{i=k}^{l} V_K(\mathbf{r}_i). \tag{2.15}$$

The Boltzmann factor of this Hamiltonian defines the statistical weight of the subchain, having a certain conformation, and is given by:

$$\exp(-\beta H) = \exp\left[-\frac{3}{2b^2} \sum_{i=k}^{l-1} |\mathbf{r}_i - \mathbf{r}_{i+1}|^2 - \beta \sum_{i=k}^{l} V_K(\mathbf{r}_i)\right]. \tag{2.16}$$

If both ends of the subchain are fixed at positions $\mathbf{r}$ and $\mathbf{r}'$, the total statistical weight can be expressed in path-integral form as [12]:

$$Q_K(k,\mathbf{r};l,\mathbf{r}') \equiv \frac{V}{Z_0(|l-k|)}\sum \exp\left[-\frac{3}{2b^2}\sum_{i=k}^{l-1}|\mathbf{r}_i-\mathbf{r}_{i+\mathbf{1}}|^2-\beta\sum_{i=k}^{l}V_K(\mathbf{r}_i)\right], \tag{2.17}$$

where the sum is taken over all possible conformations, which satisfy the condition that $\mathbf{r}_k = \mathbf{r}$ and $\mathbf{r}_l = \mathbf{r}'$, whereas V is the volume of the system, which accounts for the translational degree of freedom of the center of mass of the chain. Moreover, $Z_0(|l-k|)$ is the partition function defined in Eq. (2.9), which represents the total number of possible conformations realized by an ideal subchain composed of $|l-k|$ segments. By means of a Chapman-Kolmogorov relation:

$$Q_K(s,\mathbf{r};s',\mathbf{r}') = \int d\mathbf{r}'' Q_K(s,\mathbf{r};s'',\mathbf{r}'')Q_K(s'',\mathbf{r}'';s',\mathbf{r}'), \tag{2.18}$$

which shows that the conformations of the subchains that have no common segments are statistically independent, it is possible to rewrite Eq. (2.17) in a more tractable form as a recurrence formula [12]. For this purpose, the subchain has to be splitted into two parts (see Fig. 2.4), where the last segment is treated separately from the other segments (i.e., $i = k, ..., l-1$ and $i = l-1, l$). As a result, Eq. (2.17) takes the form:

$$Q_K(k,\mathbf{r};l,\mathbf{r}') = \frac{V}{Z_0(1)}\int d\mathbf{r}'' Q_K(k,\mathbf{r};l-1,\mathbf{r}'')\exp\left[-\frac{3}{2b^2}|\mathbf{r}''-\mathbf{r}'|^2-\beta V_K(\mathbf{r}')\right]. \tag{2.19}$$

After series of mathematical manipulations and integration, by taking a continuum limit of the discrete Gaussian chain model, where the discrete index i has been replaced by a continuous parameter s, and the limit $\Delta s \to 0$, we finally can write the following equation, which is called the Edwards equation [12, 15, 16]:

$$\frac{\partial}{\partial s}Q(s',\mathbf{r}';s,\mathbf{r}) = \left[\frac{b^2}{6}\nabla^2-\beta V_K(\mathbf{r})\right]Q(s',\mathbf{r}';s,\mathbf{r}). \tag{2.20}$$

Due to the term containing $V_K(\mathbf{r})$, this is no longer a simple diffusion equation as Eq. (2.12), but it is a basic equation for calculating the path-integral.

In the next section we will made use of the continuous Gaussian chain model, to describe a general procedure for the SCFT method on the example of a diblock-copolymer melt. It is important to note, that in the continuous Gaussian chain model the polymer chain is viewed as a continuous Gaussian filament and obeys the same Gaussian statistics as the discrete bead-spring model [11]. Besides, the advantage of this model is that it allows calculations to be performed with partial differential equations, such as Eq. (2.20) [11].

2.6 General SCFT procedure

Up to now, we have been discussing a derivation of the general equations of the SCFT. In this section, we briefly review the SCF theory for a melt composed of AD-diblock copolymers [7, 16], for which, due to the screening effect between the monomers, we can assume Gaussian statistics for the chain conformation. Within this approximation, each polymer chain consists of N_A segments of A-type and N_D segments of D-type with their respective statistical segment lengths b_A and b_D, which means that the total number of statistical segments of a chain is $N = N_A + N_D$. To distinguish each segment, we consider that the configuration of the α-th chain can be described by a space curve $\mathbf{r}_\alpha(s)$ parameterized by the chain contour variable s, where the ranges $0 \leq s \leq N_A$ and $N_A \leq s \leq N$ describe, respectively, the A-block and D-block with $s = 0$ as the free end of the A-block and $s = N$ as the other free end of the D-block (see Fig. 2.5). Let us next define the partition function integral $Q(s', \mathbf{r}'; s, \mathbf{r})$, representing the equilibrium statistical weight of a subchain between the sth- and s'th-segment with $0 \leq s' \leq s \leq N$ that is fixed at the positions $\mathbf{r}$ and $\mathbf{r}'$. This statistical weight can be evaluated within the mean-field approximation by solving the following diffusion-type partial differential equation [7]:

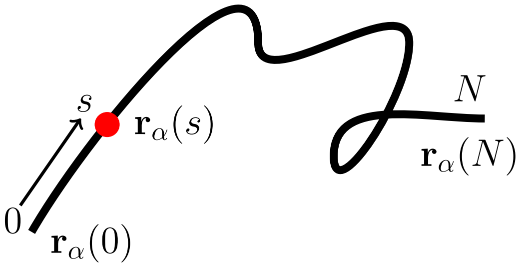

Figure 2.5: The continuous Gaussian chain model.

$$\frac{\partial}{\partial s} Q(s', \mathbf{r}'; s, \mathbf{r}) = \begin{cases} \left[\frac{b^2}{6}\nabla^2 - \beta V_A(\mathbf{r})\right] Q(s', \mathbf{r}'; s, \mathbf{r}), & 0 \leq s \leq N_A, \\ \left[\frac{b^2}{6}\nabla^2 - \beta V_D(\mathbf{r})\right] Q(s', \mathbf{r}'; s, \mathbf{r}), & N_A \leq s \leq N, \end{cases} \tag{2.21}$$

where $\beta = 1/(k_B T)$ and $V_A(\mathbf{r})$ as well as $V_D(\mathbf{r})$ are external potentials, acting on A- or D-type segments at position $\mathbf{r}$. The latter functions represent mean-field potentials, resulting from the interaction between the segments as well as from enforcing the incompressibility condition, and are obtained in a self-consistent fashion. Moreover, the initial condition for Eq. (2.21) is given by $Q(0, \mathbf{r}'; 0, \mathbf{r}) = \delta(\mathbf{r} - \mathbf{r}')$. Because the two ends of the block copolymer are not equivalent, we need to introduce an additional statistical weight $Q^*(s', \mathbf{r}'; s, \mathbf{r})$, which is calculated in the opposite direction along the chain starting from the free end $s = N$. To reduce the computational expense, the integrated statistical weights are defined in the following as:

$$\begin{aligned} q(s,\mathbf{r}) &= \int d\mathbf{r}' Q(0,\mathbf{r}';s,\mathbf{r}), \\ q^*(s,\mathbf{r}) &= \int d\mathbf{r}' Q^*(0,\mathbf{r}';s,\mathbf{r}). \end{aligned} \tag{2.22}$$

These latter weights can be proven to satisfy Eq. (2.21) similarly as the non-integrated ones. This then leads to the following diffusion equation:

$$\frac{\partial}{\partial s} q(s,\mathbf{r}) = \begin{cases} \left[\frac{b^2}{6}\nabla^2 - \beta V_A(\mathbf{r})\right] q(s,\mathbf{r}), & 0 \leq s \leq N_A, \\ \left[\frac{b^2}{6}\nabla^2 - \beta V_D(\mathbf{r})\right] q(s,\mathbf{r}), & N_A \leq s \leq N, \end{cases} \tag{2.23}$$

with the initial condition $q(0,\mathbf{r}) = 1$. Analogous expressions can be formulated for $q^*(s,\mathbf{r})$. By using the definitions in Eqs. (2.22), the volume fractions of the A- and D-type segments at position $\mathbf{r}$ can be written as:

$$\phi_A(\mathbf{r}) = C \int_0^{N_A} ds q(s,\mathbf{r}) q^*(N-s,\mathbf{r}), \tag{2.24}$$

$$\phi_D(\mathbf{r}) = C \int_{N_A}^{N} ds q(s,\mathbf{r}) q^*(N-s,\mathbf{r}), \tag{2.25}$$

where the normalization constant in the canonical ensemble is given by:

$$C = \frac{V}{\int d\mathbf{r} \int ds q(s,\mathbf{r}) q^*(N-s,\mathbf{r})} = \frac{V}{NZ}, \tag{2.26}$$

with V as the total volume of the system and Z as the single-chain partition function. The external potential $V_K(\mathbf{r})$ of a K-type segment ($K = A$ or D) can be decomposed into two terms in the following way [7]:

$$V_K(\mathbf{r}) = \sum_{K'} \epsilon_{KK'} \phi_{K'}(\mathbf{r}) - \mu_K(\mathbf{r}) = W_K(\mathbf{r}) - \mu_K(\mathbf{r}), \tag{2.27}$$

where the first term represents the interaction energy between the segments with $\epsilon_{KK'}$ as the nearest-neighbor pair-interaction energy between a K-type and K'-type segment. The latter quantity is related to the Flory-Huggins interaction parameter through the following expression $\chi_{AD} = N_{ns}\beta[\epsilon_{AD}(1/2)(\epsilon_{AA} + \epsilon_{DD})]$, where N_{ns} is the number of nearest-neighbor sites. Moreover, the function $\mu_K(\mathbf{r})$ is the chemical potential of the K-type segment, which represents a

Lagrange multiplier that enforces a constraint imposed on the system, such as the incompressibility condition. To obtain the volume fractions of the equilibrium nanostructured morphologies, the previous system of equations has to be solved in an iterative manner. First of all, the potential fields $V_A(\mathbf{r})$ and $V_D(\mathbf{r})$ are determined from the volume fractions $\phi_A(\mathbf{r})$ and $\phi_D(\mathbf{r})$ by making use of Eq. (2.27). Afterwards, the weights $q(s,\mathbf{r})$ and $q^*(s,\mathbf{r})$ are calculated by solving Eqs. (2.23) that contain the fields $V_A(\mathbf{r})$ and $V_D(\mathbf{r})$. Finally, the new volume fractions $\phi_A(\mathbf{r})$ and $\phi_D(\mathbf{r})$ are calculated from the weights $q(s,\mathbf{r})$ and $q^*(s,\mathbf{r})$ through Eqs. (2.24) and (2.25). The procedure is repeated until a self-consistent solution is reached. In Fig. 2.6 we show the basic scheme of the SCF theory.

After the self-consistent solution is obtained, the Helmholtz free energy of the system can be calculated as follows:

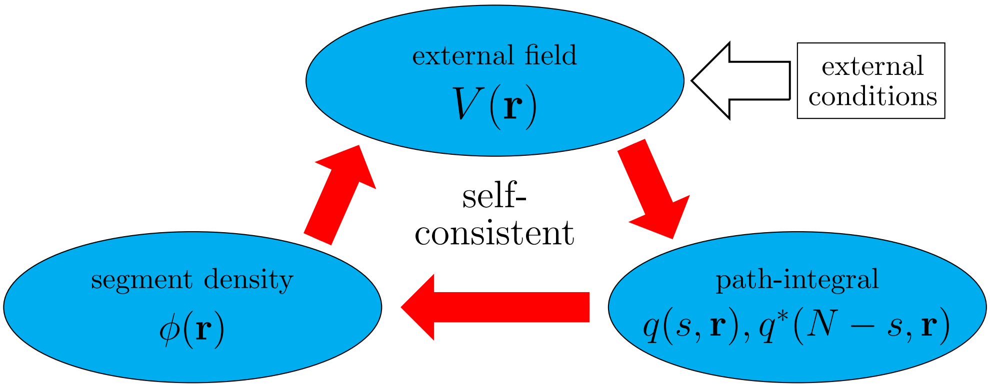

Figure 2.6: The basic scheme of the iterative procedure of the SCFT.

$$F = -k_B T M_K \ln Z + \frac{1}{2}\sum_K \sum_{K'} \int d\mathbf{r} \epsilon_{KK'} \phi_K(\mathbf{r}) \phi_{K'}(\mathbf{r}) - \sum_K \int d\mathbf{r} V_K(\mathbf{r}) \phi_K(\mathbf{r}), \tag{2.28}$$

where M_K is a total number of K-type chains in the system. This quantity relates to the average number density of K-type segments $\bar{\phi}_K$ through the equation:

$$M_K = \frac{V\bar{\phi}_K}{N_K + 1}, \tag{2.29}$$

where V is the system volume and N_K is the total number of K-type segments.

2.6.1 Static calculation

In order to get the equilibrium state in the static SCF calculation, the two fields $W_K(\mathbf{r})$ and $\mu_K(\mathbf{r})$ in Eq. (2.27) are updated simultaneously, according to the following iterative scheme:

$$W_K(\mathbf{r}) \to W_K(\mathbf{r}) + \alpha_W \left\{ \sum_{K'} \epsilon_{KK'} \phi_{K'}(\mathbf{r}) - W_K(\mathbf{r}) \right\}, \tag{2.30}$$

$$\mu_K(\mathbf{r}) = \mu_K(\mathbf{r}) - \alpha_V \left\{ 1 - \sum_{K} \phi_K(\mathbf{r}) \right\}, \tag{2.31}$$

where α_W and α_V are appropriately chosen constants between 0 and 1. By introducing updated $W_K(\mathbf{r})$ and $\mu_K(\mathbf{r})$ into Eq. (2.27), the path-integral is recalculated. The iteration procedure, illustrated in Fig. 2.6, is repeated until the fields are converged and the incompressibility condition is fulfilled within a certain error [15, 17].

2.6.2 Dynamic calculation

The dynamical mean-field method is based on the diffusion dynamics of the segments. Assuming Fick's law of linear diffusion and combining it with the conservation law for the segment density, which is expressed by the continuity equation, the time-evolution equation for the segment density can be written as follows [12, 15, 17]:

$$\frac{\partial}{\partial t}\phi_K(\mathbf{r},t) = \nabla \cdot \left[L_K(\mathbf{r},t) \left\{ \nabla \mu_K(\mathbf{r},t) + \lambda(\mathbf{r},t) \right\} \right] + \xi_K(\mathbf{r},t), \tag{2.32}$$

where $L_K(\mathbf{r},t)$ is a mobility of the K-type segment and $\lambda(\mathbf{r},t)$ is a Lagrange multiplier for the local incompressibility condition. Moreover, $\xi_K(\mathbf{r},t)$ is a random noise due to thermal fluctuations, satisfying the following fluctuation-dissipation relation:

$$\left\langle \xi_K(\mathbf{r},t)\xi_{K'}(\mathbf{r}',t') \right\rangle = 2k_BT\mathcal{L}_{KK'}(\mathbf{r},t)\nabla^2\delta(\mathbf{r}-\mathbf{r}')\delta(t-t'), \tag{2.33}$$

where $\mathcal{L}_{KK'}(\mathbf{r},t)$ is given by the local mobility coefficient $L_K(\mathbf{r},t)$ as:

$$\mathcal{L}_{KK'}(\mathbf{r},t) = L_K(\mathbf{r},t)\delta_{KK'} + \frac{L_K(\mathbf{r},t)L_{K'}(\mathbf{r},t)}{\sum_{K''} L_{K''}(\mathbf{r},t)}. \tag{2.34}$$

The segment density distribution profiles $\{\phi_K(\mathbf{r})\}$ are obtained by the integration of the time-evolution equation. In the next time step, the chemical potential $\mu_K(\mathbf{r})$ is evaluated from the given segment density distribution $\phi_K^{target}(\mathbf{r})$. After the initialization of $W_K(\mathbf{r})$ and $\mu_K(\mathbf{r})$

with 0, the following iteration scheme is used [17]:

$$W_K(\mathbf{r}) \to W_K(\mathbf{r}) + \alpha_W \left\{ W_K^{target}(\mathbf{r}) - W_K(\mathbf{r}) \right\}, \tag{2.35}$$

$$\mu_K(\mathbf{r}) = \mu_K(\mathbf{r}) - \alpha_V \left\{ \phi_K^{target}(\mathbf{r}) - \phi_K(\mathbf{r}) \right\}, \tag{2.36}$$

where $W_K^{target}(\mathbf{r}) = \sum_{K'} \epsilon_{KK'} \phi_{K'}^{target}(\mathbf{r})$. This procedure is repeated until $W_K(\mathbf{r})$ and $\mu_K(\mathbf{r})$ have converged within a certain error.

Chapter 3

Theoretical background for organic photovoltaics

3.1 Basic working principles of organic solar cells

3.1.1 Brief history

One of the first reported investigations about organic (excitonic) photovoltaic cells dates back to 1959, when Kallman and Pope discovered that the single crystals of an anthracene can be used to produce the photo-voltage [18]. Despite an extremely low efficiency of 0.1 %, this discovery gave a boost to subsequent years of research. Attempts to improve the efficiency of a single-layer organic solar cells were unsuccessful, mainly due to the reason that strongly bound excitons were formed, which are difficult to split into free charges, in order to produce a current.

The next breakthrough in the field of OPVs was done by Tang in the mid eighties, when he introduced the concept of a bilayer heterojunction and demonstrated relatively high efficiencies of around ~ 1 % [19, 20]. In this concept an electron donor material (D) and an electron acceptor material (A) were brought together and sandwiched between the electrodes. The interface between these two thin organic layers played a critical role in determining the photovoltaic properties. The improved efficiency resulted from the increased exciton dissociation at the planar D/A interface, which relates to the different electron affinities of the two materials. After a fast process of charge transfer and spatial separation of the electron and hole, the charges are able to migrate towards their respective electrodes to generate a photocurrent. The main limitation of the two-layer OPV cells is that the exciton diffusion length in organic semiconductors is typically less than 10 nm, which causes that a large number of excitons are lost on the way to the heterojunction [18, 19]. However, for the effective absorption of the incident light, a layer thickness of the absorbing material has to be much more than the diffusion length of the excitons. For this reason the device efficiencies for many years were limited to around ~ 1 %.

To overcome the problem with exciton diffusion length, Yu *et al.* [21] in 1995 proposed to mix conducting polymers with buckminsterfullerene, to obtain interpenetrating network of donor and acceptor materials. Such device structure is called a bulk heterojunction (BHJ). For this system they reported a power conversion efficiency of about 2.9 %. The substantial enhancement in efficiency with the bicontinuous network material results from the large increase in the interfacial area, which causes the reduction in the distance the excitons have to travel to reach the interface [21]. The disadvantages of the BHJ are that it is more difficult to separate Coulomb bound charge-carrier pairs and that percolation paths to the electrodes are not always present, due to the increased disorder of the material [36].

Nevertheless, the concept of BHJ has become popular, which essentially relates to the fact that the power conversion efficiencies of organic BHJ solar cells over the last few decades have increased significantly from ~ 1 % to more than 10 %, demonstrating their great potential in the field of cost-efficient photovoltaics [18, 29].

3.1.2 Organic solar cell architecture

A typical organic solar cell consists of at least five distinct layers, as depicted in Fig. 3.1.

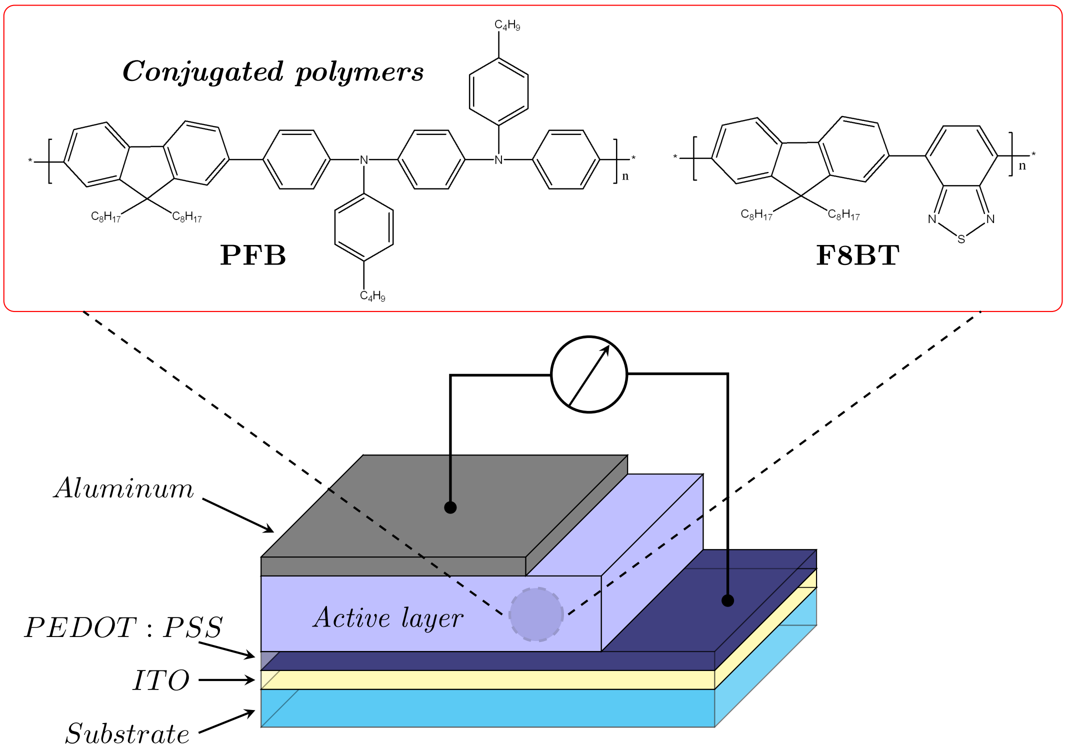

Figure 3.1: Diagram of the architecture of a polymer solar cell. The active layer either consists of a bilayer or a blend of donor- and acceptor-polymers. The inset shows the chemical structures of donor- and acceptor-type polymers composed of PFB and F8BT, respectively.

One of the electrodes must be transparent, to allow the photoexcitation of the active materials. The glass or plastic (some flexible transparent polymer) may be used as a substrate. Suitable substrates should fulfill following requirements [4]:

1. Low cost;
2. Chemical and thermal stability;
3. Mechanical and environmental stability;
4. High optical transparency.

Currently the most frequently used substrate is glass. Nevertheless, flexible plastic substrates have become popular in production of solution-processed organic photovoltaics, using roll-to-roll methods [4, 22]. As illustrated in Fig. 3.1, on top of the substrate is laid one of the electrodes, which is a transparent conductive oxide, called indium-doped tin oxide (ITO). The ITO electrode is normally coated with a conducting polymer. The most commonly used material for this purpose is a mixture of poly(3,4-ethylenedioxythiophene):poly(styrene sulfonate) ($PEDOT : PSS$), which helps to smooth out the roughness of ITO surface and to increase its work function [4]. Moreover, it serves as a hole transporter and exciton blocker [31]. Next, on top of the $PEDOT : PSS$ the active layer is deposited, which either consists of a bilayer or a blend of donor- and acceptor-polymers. For instance, PFB and F8BT are donor- and acceptor-materials, commonly used. Their chemical structures are illustrated in Fig. 3.1. This layer is responsible for light absorption, exciton generation and dissociation at heterojunction with subsequent transport of the charge carriers to the respective electrodes [31]. Finally, the second electrode is put on top of the active layer, often with an additional very thin buffer layer (Ca or LiF, not shown in Fig. 3.1), which keeps electrode material (normally Al) from diffusing into the photoactive layer [18]. Both Al from the cathode and In from the anode can diffuse as impurities into the active layer, which can contribute to the degradation of the device [86]. This issue will be discussed in section 6.6.

3.1.3 The solar spectrum

To achieve a high efficiency, the solar cell needs to absorb a large portion of the light of the solar spectrum. The total power density received at the top of the Earth's atmosphere is approximately 1360 Wm^{-2} for the extraterrestrial spectrum [23]. When light is passing through the atmosphere, a large part of this energy is absorbed and scattered by different atmospheric constituents. In the infrared region of the spectrum the absorption is almost entirely caused by H_2O (absorbs light at 900, 1100, 1400 and 1900 nm) and CO_2 (absorbs light at 1800 and 2600 nm), as well as by dust, whereas in the ultraviolet region of the spectrum the light is cutted off by oxygen, ozone and nitrogen (light below 300 nm) [24].

The absorption increases with the length traveled within the atmosphere. In order to take into account the dependence of the light intensity on the optical path length through the atmosphere, a new term, called "Air Mass" (AMn), is introduced:

$$n = \frac{\text{optical path length to the sun}}{\text{optical path length when the sun is directly overhead}} = \frac{1}{\cos(\theta)}, \tag{3.1}$$

where θ is the zenith angle in degrees. The spectrum outside the atmosphere is referred to as AM 0 and that on the surface of the Earth for normal incidence is referred to as AM 1 [24]. A typical solar spectrum at which solar cells are measured is AM 1.5, which corresponds to an angle of incidence of solar radiation of 48° relative to the surface normal [24]. The power density received in this case is:

$$P_{AM1.5} = 1000\ Wm^{-2}. \tag{3.2}$$

In Fig. 3.2, we show the AM 0 and AM 1.5 solar spectra, alongside with the black body spectrum for $T = 5760\ K$. We deduce from the graph that the greatest solar irradiance is close to the visible range of wavelengths (300 - 800 nm).

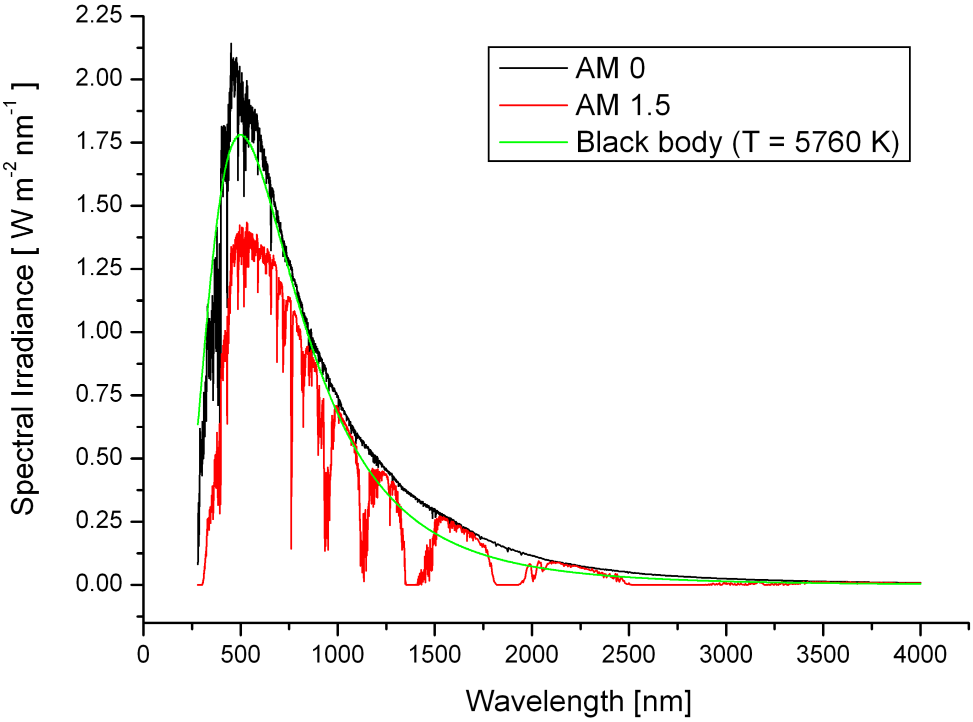

Figure 3.2: American Society for Testing and Materials (ASTM). The extraterrestrial solar spectrum (AM 0), the terrestrial solar spectrum (AM 1.5) and the black body spectrum at $T = 5760\ K$ (reproduced from [25, 37]).

It is clear that for the construction of an efficient device the absorption spectrum of the active layer must closely match the incident solar spectrum. A problem is that absorption of polymer blends strongly depends on the characteristics of their mesoscopic structure, precluding transferability among different experimental measurements. In section 4.4, we will introduce a transfer-matrix formalism to calculate the spatial distribution of absorbed power as a function of thickness and wavelength, depending on the optical constants of the respective nanophases in the active layer, which takes into account optical interference effects [137].

3.1.4 Operational principles

In a PSC the main fraction of the light is absorbed in the donor material. If a photon has an energy ($h\nu$) larger than the energy gap (E_g) of the material, the photon is absorbed. Upon photon absorption an electron in the organic semiconductor is excited from the highest occupied molecular orbital (HOMO) into the lowest unoccupied molecular orbital (LUMO) (see Fig. 3.3). This has some analogy with the process of exciting an electron from the valence band to the conduction band in case of inorganic semiconductors [26]. However, due to the low dielectric constant of organic semiconductors (typically between 3 and 4), strong Coulomb attraction of an electron-hole pair leads to the creation of a bound electron-hole pair, which is called an exciton. The created exciton diffuses and must reach a D/A interface within its lifetime to undergo the dissociation, otherwise it will recombine by emitting a photon or decay via thermalization (non-radiative recombination) [27, 28].

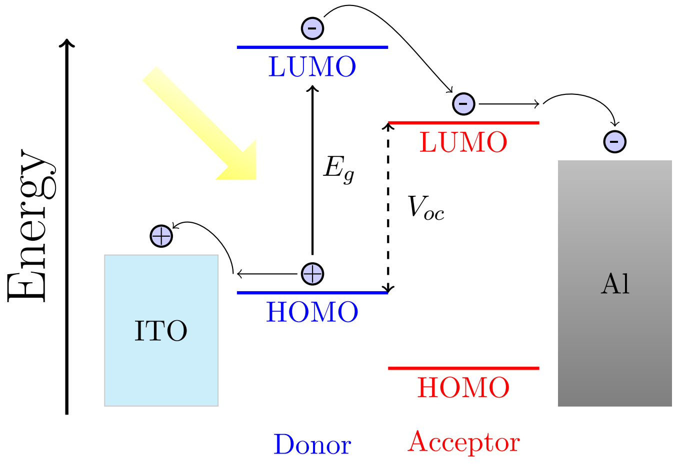

Figure 3.3: Schematic energy diagram of an organic heterojunction solar cell. The active layer consists of a donor and an acceptor material.

The exciton binding energy of organic semiconductors ranges between 0.1 and 1.4 eV, and is much higher compared to the ones of inorganic semiconductors with binding energies of a few meV [26]. Since their exciton binding energy exceeds the thermal energy at room temperature, the photogenerated excitons are only hardly separated into electrons and holes. To provide the necessary energetic driving force for charge separation, the energy offset between the LUMO of the donor and the acceptor (ΔLUMO) should be greater than the exciton binding energy [29]. If this condition is fulfilled, the photoinduced charge transfer of the electron from the LUMO of the donor to the LUMO of the acceptor become energetically favorable. The positively charged hole remains on the donor material. This photoinduced charge transfer takes place at a time scale of $\sim$ 50 fs [26, 27]. The competing processes, like photoluminescence and recombination of the charges, take place at much larger time scales, i.e. in the nanosecond and microsecond time ranges, respectively [27]. As a result, this allows efficient exciton dissociation at the heterojunction. Once the charges have been successfully separated, they have to travel to the respective electrodes within their lifetimes, where they are collected, contributing to a current in the external circuit. The potential difference of a high work function anode and low work function cathode creates a built-in electric field, which serves as a driving force for the charge transport within the PSC. During the charge transport throughout the bulk of the active layer, non-geminate recombination may occur between independently generated electrons and holes. This process is called bimolecular charge recombination.

The primary parameter, reflecting the charge transport properties of photovoltaic cells, is the external quantum efficiency (EQE), which is also called IPCE (Incident Photon to Current Efficiency). The EQE is defined as the number of electron-hole pairs flowing in the external circuit to the number of incident photons [30]:

$$\eta_{EQE} = \eta_A \cdot \eta_{IQE}, \tag{3.3}$$

where η_A is the absorption efficiency, whereas η_{IQE} is the internal quantum efficiency (IQE), which considers only absorbed photons. Therefore, the IQE is defined as the number of carriers collected at the electrodes to the number of photons absorbed in the device [30, 31] and can be expressed as:

$$\eta_{IQE} = \eta_{EDE} \cdot \eta_{CTE} = \frac{(n_e^g + n_h^g)}{2n_{ex}^g} \cdot \frac{(n_e^c + n_h^c)}{(n_e^g + n_h^g)} = \frac{(n_e^c + n_h^c)}{2n_{ex}^g}, \tag{3.4}$$

where η_{EDE} and η_{CTE} are the exciton dissociation and charge transport efficiencies, respectively. In the previous equation n_e^g, n_e^c and n_h^g, n_h^c represent the number of electrons and holes generated in the bulk and collected at the electrodes respectively, whereas n_{ex}^g represents the number of generated excitons. The factor of 2 in Eq. (3.4) accounts for the fact that the splitting of one exciton generates two charges [32].

3.1.5 Current-voltage characteristic

Current-voltage $(I - V)$ characteristic under illumination is a common way to characterize the performance of organic photovoltaic cells. As illustrated in Fig. 3.4, in the dark the cell behaves as a diode. At short-circuit condition, there is no current and at sufficiently large forward bias across the terminals the dark current is generated, resulting from carriers injected from the electrodes. When the device is exposed to light, the incident photons generate a photocurrent and the $I-V$ curve shifts downward (red solid line in Fig. 3.4). The current that flows through

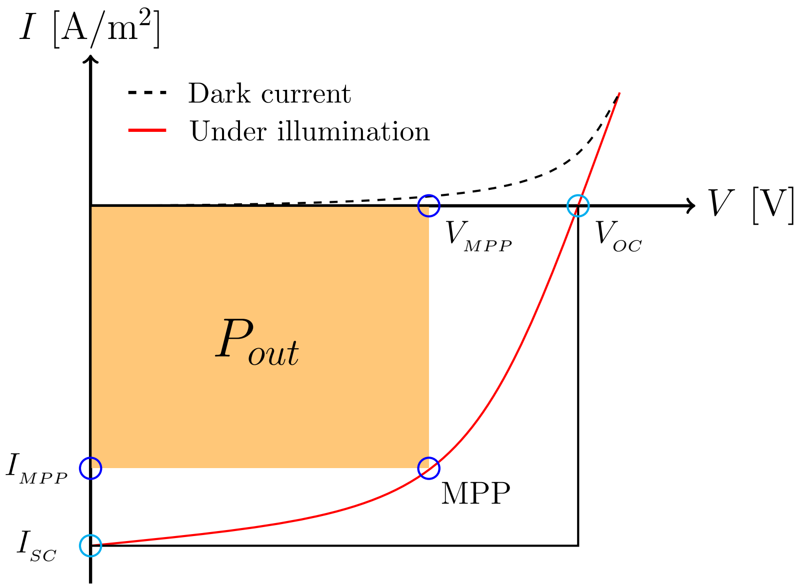

Figure 3.4: Schematic current-voltage characteristic of a polymer solar cell under illumination (red solid line) and in the dark (dashed line). Circles on the graph indicate key points: I_{SC} – the short-circuit current; V_{OC} – the open-circuit voltage; MPP – the maximum power point; I_{MPP} and V_{MPP} are the values of photocurrent and voltage for which the output power is maximum.

the illuminated solar cell, when there is no external resistance (at zero applied voltage, $V = 0$ V), is called the short-circuit current (I_{SC}). This is the maximum current that the cell is able to produce [31]. On the other hand, the maximum possible voltage (beyond which the solar cell no longer provides power) the photovoltaic cell can supply is the voltage, where the current under illumination is zero ($I = 0$ A/m^2), and is termed open-circuit voltage (V_{OC}). It is approximately limited by the energy offset between the HOMO of the donor and the LUMO of the acceptor (see Fig. 3.3) [28]. At any value of external load between the I_{SC} and V_{OC}, the solar cell is doing work at a rate $P = I \cdot V$, which defines the output power at the operating point [37]. The point where the magnitude of the product of photocurrent and voltage is maximum is designated as the maximum power point (MPP), and the power at this point is equal to $P_{out} = I_{MPP} \cdot V_{MPP}$. The ratio between the maximum power output to its theoretical power output is called the fill factor (FF):

$$FF = \frac{I_{MPP}V_{MPP}}{I_{SC}V_{OC}}, \tag{3.5}$$

which defines the squareness of the $I-V$ curve. The FF also can be seen as an area ratio of the filled and unfilled rectangles (see Fig. 3.4). The above mentioned parameters can be used to calculate the power conversion efficiency (PCE), which determines the percentage of the solar energy harvested by the cell that is converted into usable electrical power:

$$PCE = \frac{P_{out}}{P_{in}} = \frac{I_{SC} V_{OC} FF}{P_{in}}, \tag{3.6}$$

where P_{in} is the incident light power radiated by the sun or by the standard instruments for solar-cell device testing [28].

3.2 Semiconducting polymers

Conventional polymers such as plastics, rubbers, etc., have substantial electrical resistance and are either insulators or very poor electrical conductors [33, 34]. However, with the discovery of the conductive properties of polyacetylene in the 1970s, polymers have received considerable attention in the field of organic electronics [33]. They can either be semiconductors or conductors. From the band theory, it is well-established that the size of the energy band gap determines whether the polymer is a conductor, semiconductor or insulator [35]. The conductivity in polymer-based semiconductors relates to conjugation, resulting from the alternation of single and double bonds between neighboring carbon atoms [36]. The overlap of the p_z electron wavefunctions leads to delocalization and formation of π orbitals. Due to the Peierls instability, there are two delocalized energy bands: the bonding (π) and anti-bonding (π^*) orbitals [36]. The energy gap between the HOMO in the π-band and the LUMO in the π^*-band determines the semiconducting nature of the system [37]. Due to the amorphous nature of the polymers, the delocalization length of the π orbitals is limited to a definite conjugation length. This causes that the charges become localized on small segments of the polymer chain, which are called conjugated segments [37]. The random fluctuation in conjugation length of the polymer chains creates a disordered distribution of electronic states between segments. This energetic disorder can be approximated by the Gaussian density of states (DOS) [38]. Here, it should be noted, that excitons are also subjected to localization and energetic disorder but in a different way than charges [37]. An exciton is confined to a chromophore, which has a length of typically 5 monomers [39]. The energetic disorder of chromophores can also reasonably be approximated by the Gaussian distribution, as described in detail in Ref. [37].

3.3 Energy transport

3.3.1 Exciton formation

Let us now consider that an unexcited organic molecule, in which electronic spins are paired (opposite spins), is in the ground singlet state, $\mathrm{S_0}$. Upon photon absorption the molecule is excited and an electron is promoted from the $\mathrm{S_0}$ state into a new state of higher energy. If the transition occurs without change of spin, the new excited state is also a singlet state, $\mathrm{S_1}$, or higher excited singlet states $\mathrm{S_n}$. The transition of an electron between states of unlike multiplicity ($\mathrm{S_1} \rightarrow \mathrm{T_1}$) is spin-forbidden and occurs only because of spin-orbit coupling, which allows for intersystem crossing. Due to the low dielectric constant of common organic materials ($\varepsilon_r \sim$ 3 - 4), Coulomb bound electron-hole pairs are created upon light absorption, which are called excitons. It has been shown by Narayan *et al.* [40] that singlet excitons diffuse and dissociate faster than triplet excitons at heterojunctions of organic solids, due to a lower binding energy. Besides, because of higher diffusion coefficient, the singlet excitons have a higher diffusion length than the triplet excitons, which has been investigated using Förster and Dexter energy transfer models, respectively [40].

3.3.2 Exciton transport

The efficiency of the exciton dissociation process strongly depends on the exciton transport within the material of interest and is usually modeled using Förster resonance energy transfer theory (FRET) [42, 44]. FRET is a long-range mechanism and refers to the non-radiative energy transfer of an electronic excitation from a donor molecule to an acceptor molecule and does not require physical contact between them [45]:

$$\mathrm{D}^* + \mathrm{A} \rightarrow \mathrm{D} + \mathrm{A}^*$$

This energy transfer arises from a dipole-dipole interaction between the electronic states of the donor and the acceptor molecules. Since the energy must be conserved, the energy gain of the acceptor must be the same as the energy loss of the donor [43]. The rate of energy transfer, which was determined by Förster, is given by [43]:

$$\omega_{ET} = \omega_e \left(\frac{r_0}{r}\right)^6, \tag{3.7}$$

where $\omega_e = 1/\tau_0$ with τ_0 as the fluorescence lifetime of the exciton, r_0 is the exciton localization radius (the Förster radius) and r is the distance between donor and acceptor. The Förster radius defines a critical distance at which the fluorescence probability is equal to the energy transfer probability. It is given by [43]:

$$r_0^6 = \frac{9000 \ln(10) \phi_{\kappa^2}}{128\pi^5 n^4 N_A} \int_0^\infty \epsilon(\nu) F(\nu) \frac{d\nu}{\nu^4}, \tag{3.8}$$

where ϕ is the fluorescence quantum yield, whereas κ is the orientation factor between donor and acceptor, N_A and n are Avogadro's number and refractive index, respectively. $\epsilon(\nu)$ is the fluorescence spectrum of the donor, which is normalized to its peak, whereas ν is the frequency of light and F is the absorption spectrum of the acceptor. Bässler *et al.* [46] have found that the Förster radius of $r_0 \sim 3$ nm is in good agreement between experiment and simulations for polyfluorene film.

The simplest version of FRET theory (Eq. (3.7)) has proven to be very successful in simulating the exciton diffusion in organic semiconductors [47]. However, in some cases this theory gives a fairly high mobility of the excitons [48]. The main problem is that the model in Eq. (3.7) does not consider the effects of inhomogeneous broadening and energetic disorder on the energy transfer, which sometimes leads to considerable errors in prediction of exciton diffusion parameters [43, 48]. A more convenient way to calculate the hopping rate, at which the exciton hop from current site i to a nearby site j, is provided by [41, 42]:

$$\omega_{ij} = \omega_e \left(\frac{r_0}{r_{ij}} \right)^6 f(E_i, E_j), \tag{3.9}$$

where $f(E_i, E_j)$ is the Boltzmann factor, which accounts for energetic disorder by considering that:

$$f(E_i, E_j) = \begin{cases} \exp\left(-\frac{\Delta E_{ij}}{k_B T}\right) & \text{for } E_j > E_i, \\ 1 & \text{for } E_j < E_i, \end{cases} \tag{3.10}$$

with E_i and E_j as the energy levels of sites i and j. The energy levels of all hopping sites are assumed to be randomly assigned according to a Gaussian distribution, as depicted in Fig. 3.5 [43]. The energetic disorder of the material is quantified by the standard deviation, σ, of the Gaussian distribution, which typically is in the range between 50 and 150 meV for organic semiconductors. Here, it should be noted, that restricting exciton hopping to a nearest neighbor can lead to energetically unfavorable hops, whereas hopping to sites outside the range of the nearest neighbors may be more efficient from the point of view of energetic barrier [37]. Therefore, in the work presented throughout this thesis, the excitons were allowed to jump within a radius

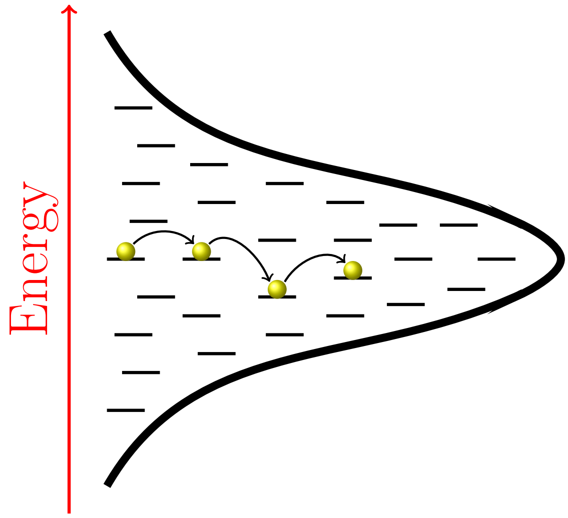

Figure 3.5: Energetic disorder of the intrinsic density of states (DOS) which is approximated by the Gaussian distribution with the standard deviation, σ.

of 3 nm in the hole- and electron-conducting phase. This range agreed with the experimentally and theoretically determined value for the Förster radius of $\sim$ 3 nm [46].

Upon light absorption, only singlet excitons are created and the triplet excitons can only be created through intersystem crossing. But for typical organic systems, such as blend of P3HT:PCBM, the intersystem crossing is irrelevant, since the overall rate for diffusion and subsequent dissociation of the singlet excitons is much higher than the intersystem crossing and therefore no triplets are formed [43, 49]. Thus, singlet excitons are the dominant exciton species in the system and FRET theory is the preferred approach to describe exciton behavior in PSCs [43].

3.4 Charge transport

In disordered systems, such as organic semiconductors, charge transport occurs through the hopping processes. There are two well-established approaches to calculate the hopping rate of charge carriers from occupied to unoccupied states: (1) model of Miller and Abrahams [50] and (2) model of Marcus [119]. Both models are used in different context and are not exactly equivalent. The Miller-Abrahams model is purely empirical and based on a phonon-assisted tunneling mechanism [51], whereas the Marcus equation is based on the polaronic effect and results from a full analytical analysis of molecular charge transport [37].

3.4.1 Miller-Abrahams equation

According to the Miller-Abrahams expression the hopping rate between sites i and j is defined as follows [50, 51]:

$$\omega_{ij} = \omega_0 \exp(-2\gamma r_{ij}) f(E_i, E_j), \tag{3.11}$$

where the prefactor ω_0 is the attempt-to-hop frequency or the maximum hopping rate, r_{ij} is the distance between sites i and j and γ is the constant, which specifies the extent to which the charges are localized and is taken as 2 nm^{-1} [121]. The last term $f(E_i, E_j)$ is the Boltzmann factor, defined in Eq. (3.10):

$$f(E_i, E_j) = \begin{cases} \exp\left(-\frac{\Delta E_{ij}}{k_B T}\right) & \text{for } E_j > E_i, \\ 1 & \text{for } E_j < E_i, \end{cases} \tag{3.12}$$

where E_i and E_j are the energy levels of the respective sites, while $k_B T$ is the thermal energy.

3.4.2 Marcus equation

The transition rate for polarons as determined by Marcus theory is given by the following equation [119, 124, 123]:

$$\omega_{ij} = \frac{2\pi}{\hbar} J_{ij}^2 \frac{1}{\sqrt{4\pi\lambda k_B T}} \exp\left[-\frac{(\Delta G_{ij}^0 + \lambda)^2}{4\lambda k_B T}\right], \tag{3.13}$$

where J_{ij}^2 is the transfer integral, i.e. the wavefunction overlap between sites i and j. λ is the intermolecular reorganization energy related to the polaron relaxation. ΔG_{ij}^0 is the difference in the Gibbs free energy before and after the reaction (see Fig. 3.6), whereas $k_B T$ is the thermal energy. In the following we will briefly describe the physical meaning of the transfer integral and reorganization energy.

3.4.3 The electronic coupling and reorganization energy

The expression for the Marcus rate 3.13 can be factorized into an electronic and a vibrational contributions as follows [52]:

$$\omega_{ij} = \frac{2\pi}{\hbar} J_{ij}^2 \cdot FCWD, \tag{3.14}$$

Here, $J_{ij} = \langle \psi_i \,|J|\, \psi_j \rangle$ is the electronic coupling matrix element, often called transfer integral, where ψ_i and ψ_j are the wavefunctions of the two charge-localized states (before and after the charge transfer) and J is the electronic Hamiltonian of the system (see Fig. 3.6) [37, 124]. The electronic coupling term largely depends upon the orbital overlap between adjacent molecules, and as so it needs to be large for a higher mobilities [53].

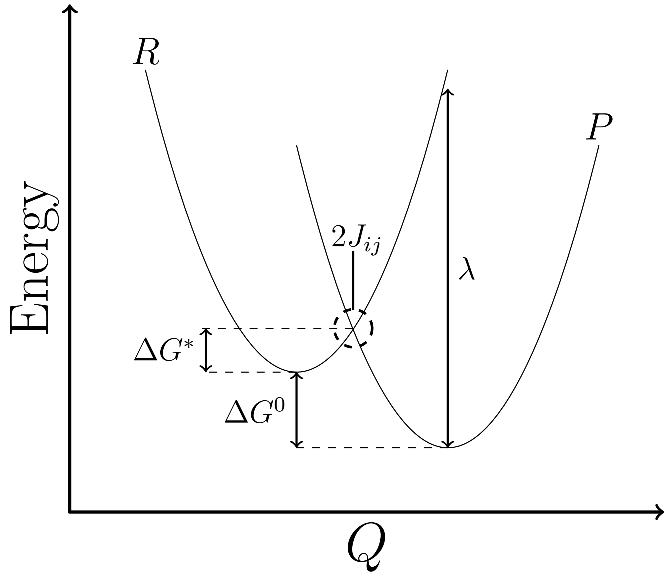

Figure 3.6: Potential energy surfaces for the reactant (R) and the product (P) of the system with the Gibbs free energy of reaction ΔG^0 as a function of reaction coordinate Q (which is a measure of the amount of charge that is transferred). The energy barrier ΔG^* required to reach the transition state and the reorganization energy λ are also illustrated.

On the other hand, $FCWD$ denotes the Franck-Condon weighted density of states. This factor accounts for the physical deformation of the polymer chain when an electron or hole hops from charged, relaxed unit to an adjacent neutral unit [37, 53]. As illustrated in Fig. 3.6, the charge transfer can be viewed as a thermal activation (with activation energy ΔG^*) of the system from the minimum of curve R to the crossing point of the diabatic curves R and P prior to electron (hole) transfer, and then relax into its new ground state (minimum of curve P) [124].

One of the key quantities that controls the charge transfer rates is the reorganization energy λ. This is the energy required to reorganize all molecules, which are involved in the reaction, on going from one ground state to another. In other words, this is the energy required to force the reactant (R) to adopt the same state configuration as the product (P), as illustrated in Fig.

3.6. The lower the reorganization energy, the smaller the geometry relaxations and the higher the charge transfer rate.

By assuming that both R and P parabolas are of equal shape, we can obtain the following relation between three energies involved in the reaction:

$$\Delta G^{*} = \frac{\left(\lambda + \Delta G^{0}\right)^{2}}{4\lambda}, \tag{3.15}$$

which shows the quadratic dependence of the free energy of activation on the free energy of reaction [54]. Besides, this relation shows that only two energies are required in the final expression for the rate constant.

Chapter 4

The dynamic Monte Carlo model

4.1 Introduction

With numerical approaches it is possible to obtain useful information about the microscopic processes underlying photocurrent generation in PSCs. There are several model types, such as drift-diffusion, Master Equation and dynamic Monte Carlo, that have received considerable attention due to their ability to reproduce many experimental characteristics and identifying the main factors responsible for device efficiency [37, 55]. For instance, drift-diffusion models are used to describe charge transport by solving coupled differential equations. The main lack of these models is that they are not able to take full account of the effect of three-dimensional morphologies and they do not consider multiple stages of exciton dissociation process [37]. Another alternative to investigate charge transport is the Master Equation approach. This approach describes steady-state occupational probabilities of sites on a lattice in terms of the Pauli Master Equation [56]. After being solved, this equation provides intrinsic quantities of solar cell systems, like mobility and current. However, it has several disadvantages. First of all, this model works only for the low charge carrier densities [55]. Furthermore, it is not possible to treat Coulomb interactions due to the fact that the model describes only occupational probabilities [56]. On the other hand, all previously mentioned limitations can be overcome by using dynamic Monte Carlo (DMC). Although the DMC is computationally more expensive than other models, this method treats explicitly all correlation effects and, since being designed to account for multiple reaction types, it is more appropriate for full device calculations with multiple particle types [37, 55].

4.2 The first reaction method

A popular technique to simulate the performance of OPV devices is exact mesoscopic Monte Carlo (MMC) [57]. However, this approach is inefficient to simulate photovoltaic processes on large scale morphologies, because the number of particles in the system (excitons, electrons or holes) typically is in the range of 100, and for each particle one must calculate all possible events, such as hopping, dissociation, recombination and extraction, taking into account morphologically and energetically disordered landscape [57]. To simplify the simulations, one might consider to use the Gillespie's first reaction method (FRM) [58]. In cope of this method the behavior of each particle is calculated just once, when a process associated with a particle is first enabled and not updated when the local landscape of the potential changes as other charge carriers move around [57, 118]. This approximation reduces time of a run by several orders of magnitude and agrees with the exact simulation within an error of ~ 2 - 6 % [57].

The FRM methodology uses the solution of the Master Equation. In the general case the Master Equation can be written as:

$$\frac{dP}{dt} = -\omega P(t), \tag{4.1}$$

and the final solution to this equation in terms of the waiting time ($t_{i\to j}$) can be re-written as (for the detailed derivation see Ref. [37]):

$$t_{i\to j} = -\ln(X)\frac{1}{\omega_{i\to j}}, \tag{4.2}$$

where X is a random number in the interval [0,1] and $\omega_{i\to j}$ is a characteristic rate of the process being considered. The FRM approach implies that all allowed events are stored in the queue in order of ascending waiting times. During each iteration of the algorithm, the event with the shortest time interval $t_{i\to j}$ is executed at ($first\ reaction$):

$$t_{i\to j} = \{t_1, t_2, ..., t_N\}. \tag{4.3}$$

When the first reaction takes place, the particle location will be updated and the total simulation time will be incremented by t. Newly enabled events are then found and inserted into the queue in the correct position in correspondence to assigned waiting times. This iterative procedure is repeated before we reach a predetermined number of generated excitons by the light absorption.

4.3 General DMC algorithm

To simulate the photovoltaic process [69], we assumed that three types of elementary particles are present in the PSC device, i.e. electrons, holes and excitons. Depending on the nature and environment of the elementary particles, they can exhibit the following algorithmic steps:

1. Exciton generation by light absorption;
2. Exciton motion within the material through diffusion or exciton annihilation;
3. Exciton dissociation at the D/A heterojunction with creation of an electron and a hole;
4. Charge recombination or charge motion under the influence of the built-in electric field resulting from the difference between the electrode work functions;
5. Charge collection at the appropriate electrodes.

In simulation studies throughout this thesis, we considered systems composed of DA-diblock copolymers, ADA-triblock copolymers and AD-blend, where the A- and D-blocks correspond to the acceptor and donor component, respectively. To accomplish the dynamical evolution of the elementary particles, we used the first-reaction method [58, 59, 60], which was described above. Moreover, we assumed that the particle motion within the system occurs through hopping between different lattice sites. These hopping processes together with the other available processes, given in the summary of algorithmic steps listed previously, constituted the sequence of configurational changes that can take place during the system's evolution through phase space.

4.3.1 Exciton-associated processes

The excitons enter the system at randomly chosen sites in the lattice with a constant rate of ω_{cre}, which in each particular case has been determined from the AM 1.5 solar spectrum with an illumination of 90 mW/cm^2 and the absorption spectrum of the given polymer material [41, 60, 61]. Once created, the exciton may diffuse, recombine or dissociate. The exciton hopping rate from lattice site i to a nearby site j has been calculated through Eq. (3.9). Note that the excitons on the lattice were allowed to jump within a radius of 3 nm in either the hole- or electron-conducting phase. When the exciton become localized on any of the sites in the system, it automatically assigned corresponding energy associated with a given site. These energies are drawn from a Gaussian distribution of width σ (see section 3.3.2). The prefactor $\omega_e r_0^6$ in Eq. (3.9) as well as exciton recombination rate ω_{dec} were selected in such a way that, for each particular system, the experimental values of exciton diffusion length and lifetime were reproduced. On meeting the D/A interface before recombining, the exciton may dissociate with generation of a bound electron-hole pair with a rate ω_{exs}. Following the dissociation, the charge pair can be separated and both charges are then able to hop away from each other or they can recombine to the ground state.

4.3.2 Electron- and hole-associated processes

Once separated, the charge carriers must be assigned one of the following events: movement by nearest neighbor hops, charge recombination or extraction by the corresponding electrode. When a charge is placed in a solid, its interaction with vibrational modes of the system causes surrounding atoms to relax around this charge and, hence, this leads to the deformation of the surrounding chains [37, 56]. As a result, the microscopic properties of these chains are also changing. Such an effect is described by the coupling between the charge and its associated phonon cloud, which leads to the formation of a quasi-particle called polaron [37]. As these polaronic effects are important within the active layer of the morphology, a more preferable will be to use the Marcus hopping formalism than the Miller-Abrahams [56]. The rate of hopping of charge carriers between nearest-neighbor lattice sites is then calculated using following formula [118, 119]:

$$\omega_{ij} = V_{hop} \exp\left[-\frac{(\Delta E_{ij} + \lambda)^2}{4\lambda k_B T}\right], \tag{4.4}$$

where

$$\Delta E_{ij} = E_j - E_i = \Delta E_{ij}^C + \Delta E_{ij}^I + \Delta E_{ij}^F + \Delta E_{ij}^\sigma, \tag{4.5}$$

denotes the difference between the energies of hopping sites j and i, whereas k_B is Boltzmann's constant and λ is the reorganization energy corresponding to twice the polaronic binding energy (see section 3.4).

In the previous equation, ΔE_{ij}^C represents the energy difference between the Coulombic interaction energies of the charges at site j and i with all other charges within a cutoff radius [41]:

$$\Delta E_{ij}^C = E_j^C - E_i^C, \tag{4.6}$$

with

$$\Delta E_i^C = \sum_{j=1}^{n} \frac{qe}{4\pi\varepsilon_0\varepsilon_r r_{ij}}, \tag{4.7}$$

where n is the total number of other charges in the system within the cutoff r_c and e is the elementary charge with $q = +e$ for electron-electron and hole-hole repulsion as well as $q = e$ for electron-hole attraction. The parameters $\varepsilon_0\varepsilon_r$ designate the dielectric constant with ε_0 as the vacuum permittivity and ε_r the relative permittivity. We treated the long-range tail of the electrostatic contribution by cutting the Coulomb potential at r_c and shifting the function to zero as well as using periodic boundary conditions, applied in direction of the electrodes.

The contribution of the polarization of the electrodes (image charge effect) was included through [41]:

$$\Delta E_{ij}^I = \frac{e^2}{16\pi\varepsilon_0\varepsilon_r}\left(\frac{1}{x_i} - \frac{1}{x_j}\right), \tag{4.8}$$

where x_i and x_j denote the distances from the respective electrodes. This term ensures that the potential at each electrode is fixed.

Another important contribution to the energy relates to the action of the external and internal electrical fields on the charges and was taken into account as follows:

$$\Delta E_{ij}^{F} = e[\mathcal{E}_{ext} - \mathcal{E}_{int}](x_i - x_j), \tag{4.9}$$

where $\mathcal{E}_{ext}$ represents the external electrical field arising from an applied external voltage, and under short-circuit conditions equals to zero ($\mathcal{E}_{ext} = 0\ \mathrm{Vm}^{-1}$). The internal electrical field, which is caused by the built-in voltage arising from the difference in electrode work functions $\Delta\phi_w$, was included through $\mathcal{E}_{int} = \Delta\phi_w/d$, where d defines the distance between the electrodes. The built-in field under short-circuit conditions drives the electrons and holes toward the respective electrodes.

In addition, to take into account the effect of energetic disorder of the material on the charges, we added the following contribution:

$$\Delta E_{ij}^{\sigma} = E_j^{\sigma} - E_i^{\sigma}, \tag{4.10}$$

where E_i^{σ} is the energy from the Gaussian density of states (DOS) distribution and σ is the corresponding standard deviation.

The prefactor V_{hop} was obtained as follows. Assuming a purely diffusive charge transport, the mobility can be described by a simple diffusion equation [37]:

$$\left\langle x^2 \right\rangle = nDt, \tag{4.11}$$

where $\left\langle x^2 \right\rangle$ is the mean square displacement, n depends on the dimensionality and can be 2, 4 or 6, whereas D and t are the diffusion coefficient and the time, respectively. The mobility is related to the diffusion coefficient by the Einstein-Smoluchowski relation as following [37]:

$$\mu = \frac{eD}{k_B T}. \tag{4.12}$$

Assuming a nearest neighbor hopping with a lattice constant a, taking $n = 6$ and using $a^2 =$

$6D/\omega$, the hopping rate can be written in the following way [37, 121]:

$$\omega = \frac{6D}{a^2} = \frac{6\mu k_B T}{ea^2}. \tag{4.13}$$

Under isoenergetic site condition, for a given combination of μ, T, a and equating Eqs. (3.13) and (4.13), the prefactor for the Marcus equation can be determined as follows [32, 37, 118, 121]:

$$V_{hop} = \frac{6k_B T \mu_{e/h}}{ea^2} \exp\left[\frac{\lambda}{4k_B T}\right], \tag{4.14}$$

where $\mu_{e/h}$ defines the mobility of the electrons/holes in both polymer species. Here it should be noted, that in our simulations, where it is not specifically stated, we assumed the electrons and holes to have equal mobilities. In addition, we ensured that, if an electron and a hole are located on adjacent sites, they can recombine with the rate w_{rec}.

Besides the generation of charges by the exciton dissociation, charges can enter the system by the injection from the electrodes. The charges are injected from the Fermi levels of the electrodes to the correct polymer type (electrons to electron-conducting, holes to hole-conducting). To calculate the rate of hopping of charge carrier from the electrode into the polymer we used the conventional Miller-Abrahams expression [62, 63] (see section 3.4), because the Marcus theory, which takes into account polaronic effects, is not applicable to injection processes [37]. Following the same procedure as it was done above for Marcus equation, using Eq. (3.11), the Einstein relationship and $a^2 = 6D/\omega$ for isoenergetic material, we obtain the maximum hopping rate of electrons (holes):

$$\omega_0 = \omega_{e/h} = \frac{6k_B T \mu_{e/h}}{qa^2} \exp(2\gamma a). \tag{4.15}$$

After having defined unoccupied site in the correct polymer for the injection and calculated the waiting time, the injection event is inserted into the queue. Finally, when the charge is injected, it will move by nearest neighbor hops as a normal charge in correspondence with above described mechanism.

In the calculations, we set the system temperature to $T = 298$ K. All the simulations were run up to the predetermined number of generated excitons. Moreover, we considered the system to be equilibrated, when the deviations in the values of the exciton dissociation efficiency, charge transport efficiency and exciton lifetime did not exceed the preset error of 0.01 % within a certain time span in the production phase of the simulation.

In Fig. 4.1 we have sketched all possible events in our DMC model, which can take place when simulating photovoltaic processes in organic solar cells.

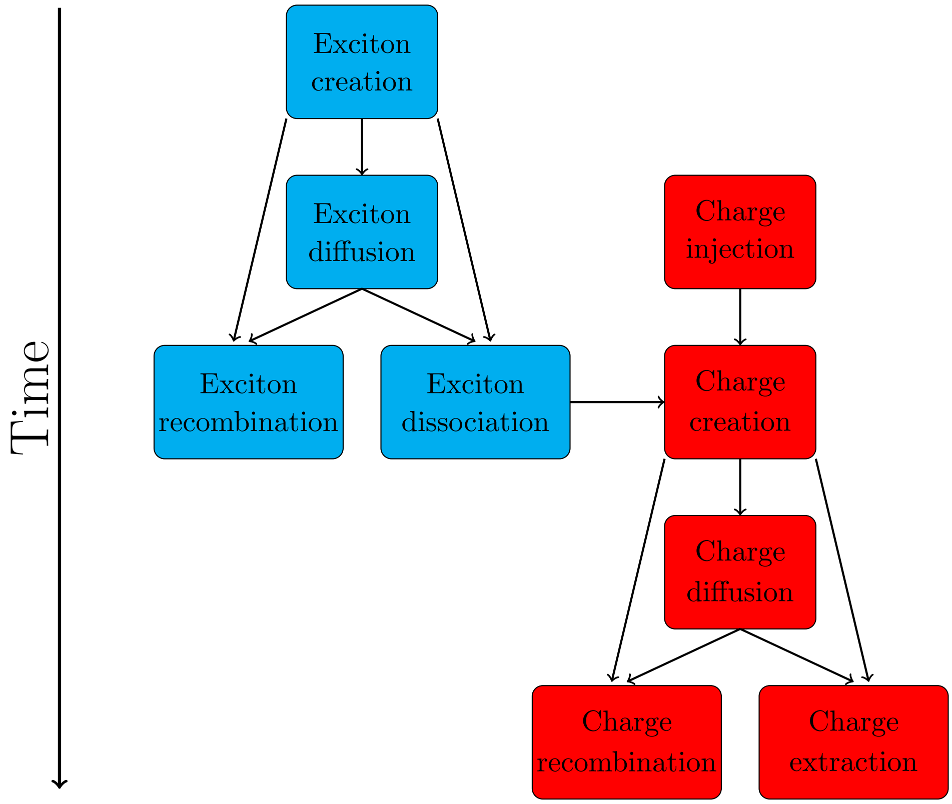

Figure 4.1: Schematic representation of all possible events in our dynamic Monte Carlo model.

4.3.3 DMC-SCFT algorithm

To compute the photovoltaic properties of both blend and block-copolymer systems considered in this thesis, we make use of our recently developed multiscale solar cell algorithm, which relies on the coupling of a mesoscopic SCFT approach, to generate the nanoscale morphologies of the polymer systems under consideration, with a suitable DMC algorithm, to model the elementary photovoltaic processes [7, 69]. The devices were discretized into a lattice of hopping sites (Cartesian grid), each of which has either electron- or hole-transporting character in conjunction with a lattice constant of $a_0 = 1$ nm. At each lattice site we imposed a single occupancy constrain for the elementary particles. Moreover, we assumed that the majority component determines whether the site is either part of the electron-conducting or hole-conducting phase. This is an approximation, which fails in systems, where there is a strong mixing of the donor and acceptor segments, resulting in a broad interfacial region. In the second part of the thesis we present techniques to avoid this approximation by parameterizing the exciton dissociation rates as well as charge transfer rates as a function of volume fractions of both components using particle-based simulations at atomistic and quantum level. We called this method parameterized field-based approach. Besides, in order to take into account the absorption of the different phases and of the electrode materials, we further extended our approach by including results from the transfer-matrix calculations to determine the distribution of exciton creations within the photoactive layer. This method was named full-device DMC-SCFT approach.

4.4 Transfer-matrix method

The transmission and reflection by the electrodes, as well as an absorption by the electrode materials, influencing an actual optical absorption distribution, which is directly dependent on the distribution of the optical electric field inside the device [136]. In this regard, to determine the distribution of exciton creations as a function of position in the photovoltaic device and introduce it as an input parameter into our DMC algorithm, we performed optical electric field calculations using transfer-matrix method. The detailed description of the method is laid out below. As described in Fig. 4.2, the multilayer stack used in the optical electric field calculations consists of m layers ($j = 1, ..., m$ corresponds to the active layers of the morphology) embedded between two semi-infinite layers ($j = 0$) and ($j = m + 1$) with a thickness of each layer, d_m. The photovoltaic device is assumed to be illuminated from left in the direction z along the surface normal. Optical properties of each layer are described by its complex index of refraction:

$$\bar{n}_j = n_j + i \cdot k_j, \tag{4.16}$$

which is a function of wavelength of the incident light. For simplicity, it is assumed that the materials are homogeneous and isotropic and the interfaces between the layers of the solar cell are assumed to be optically flat [30].

At the interface between adjacent layers j and k, the propagation of the optical electric field is described by the interface matrix I_{jk} as follows [30]:

$$\begin{bmatrix} \bar{E}_j^+ \\ \bar{E}_j^- \end{bmatrix} = I_{jk} \begin{bmatrix} \bar{E}_k^+ \\ \bar{E}_k^- \end{bmatrix} = \begin{bmatrix} \frac{1}{t_{jk}} & \frac{r_{jk}}{t_{jk}} \\ \frac{r_{jk}}{t_{jk}} & \frac{1}{t_{jk}} \end{bmatrix} \begin{bmatrix} \bar{E}_k^+ \\ \bar{E}_k^- \end{bmatrix}, \tag{4.17}$$

where $\bar{E}_j^+$, $\bar{E}_k^+$ and $\bar{E}_j^-$, $\bar{E}_k^-$ are the components of the electric field propagating in the positive and negative z directions, respectively, whereas r_{jk} and t_{jk} are the Frensel complex reflection and transmission coefficients at interface jk. For light with the electric field perpendicular to

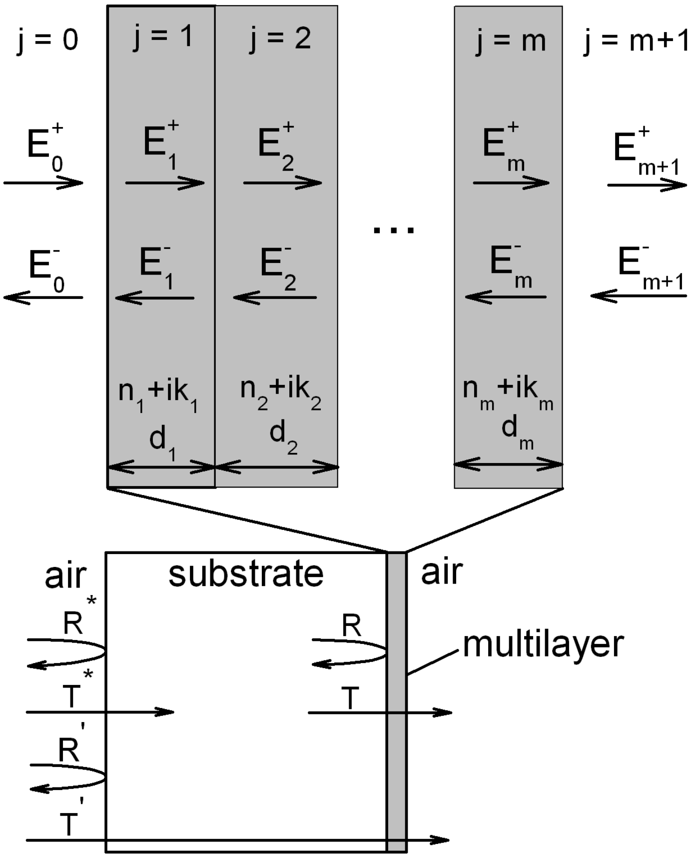

Figure 4.2: Geometry of multilayer stack used for the optical electric field calculations [30]. The multilayer structure has m layers between the transparent substrate (j = 0) and air (j = m + 1) with a thickness of each layer d_m. The optical electric field at any point in layer j is represented by two components: E_j^+ propagating in the positive direction and E_j^- propagating in the negative direction.

the plane of incidence the Frensel complex reflection and transmission coefficients are [136]:

$$r_{jk} = \frac{(\bar{n}_j - \bar{n}_k)}{(\bar{n}_j + \bar{n}_k)}, \tag{4.18}$$

$$t_{jk} = \frac{2\bar{n}_j}{(\bar{n}_j + \bar{n}_k)}. \tag{4.19}$$

The absorption and phase shift are occurring when the E-field is propagating through a layer j. This can be described by the layer matrix L_j:

$$L_j = \begin{bmatrix} e^{-i\xi_j d_j} & 0 \\ 0 & e^{i\xi_j d_j} \end{bmatrix}, \tag{4.20}$$

where $\xi_j d_j$ is the layer phase thickness with $\xi_j = (2\pi/\lambda)\bar{n}_j$. The E-field at ambient and substrate sides are related via the total system transfer matrix (scattering matrix) S as:

$$\begin{bmatrix} \bar{E}_0^+ \\ \bar{E}_0^- \end{bmatrix} = S \begin{bmatrix} \bar{E}_{m+1}^+ \\ \bar{E}_{m+1}^- \end{bmatrix}, \tag{4.21}$$

where

$$S = \begin{bmatrix} S_{11} & S_{12} \\ S_{21} & S_{22} \end{bmatrix} = \left(\prod_{n=1}^{m} I_{(n-1)n} L_n \right) \cdot I_{m(m+1)}. \tag{4.22}$$

The resulting reflection and transmission coefficients for the total layered structure can be expressed using Eq. (4.21) as [136]:

$$r = \frac{\bar{E}_0^-}{\bar{E}_0^+} = \frac{S_{21}}{S_{11}}, \tag{4.23}$$

$$t = \frac{\bar{E}_{m+1}^+}{\bar{E}_0^+} = \frac{1}{S_{11}}. \tag{4.24}$$

The effect of the substrate, i. e. the reflectance and transmittance at the air/substrate and substrate/multilayer interfaces, is included by correcting the transmissivity (T) and reflectivity (R), rather than describe the glass substrate directly with the transfer-matrix method. The corrected transmissivity and reflectivity are denoted as $T^{'}$ and $R^{'}$, respectively:

$$R^{'} = \frac{R^* + R}{1 + R^* R}, \tag{4.25}$$

$$T^{'} = \frac{T^* T}{1 + R^* R}, \tag{4.26}$$

with

$$R^* = \left| \frac{1 - \bar{n}_0}{1 + \bar{n}_0} \right|^2, \tag{4.27}$$

$$T^* = \left| \frac{2}{1 + \bar{n}_0} \right|^2, \tag{4.28}$$

where $\bar{n}_0$ is the refractive index of the substrate. The absorption efficiency of the PSC is then expressed as follows [30]:

$$\eta_A = 1 - T' - R'. \tag{4.29}$$

In order to obtain the internal electric field within layer j the layer system can be divided into two subsets, which means that the total multilayer transfer matrix is [30, 136]:

$$S = S_j^- L_j S_j^+, \tag{4.30}$$

with the partial system transfer matrices for layer j

$$S_j^- = \left(\prod_{n=1}^{j-1} I_{(n-1)n} L_n \right) \cdot I_{(j-1)j}, \tag{4.31}$$

and

$$S_j^+ = \left(\prod_{n=j+1}^{m} I_{(n-1)n} L_n \right) \cdot I_{(m+1)m}. \tag{4.32}$$

The internal transfer coefficient, which relates the E-field propagating in the positive direction to the incident plane wave can be expressed as:

$$t_j^+ = \frac{\bar{E}_j^+}{\bar{E}_0^+} = \frac{\frac{1}{S_{j11}^-}}{1 + \frac{S_{j12}^- S_{j21}^+}{S_{j11}^- S_{j11}^+} e^{i2\xi_j d_j}}, \tag{4.33}$$

and similarly for the E-field propagating in the negative direction:

$$t_j^- = \frac{\bar{E}_j^-}{\bar{E}_0^+} = t_j^+ \frac{S_{j21}^+}{S_{j11}^+} e^{i2\xi_j d_j}. \tag{4.34}$$

The total electric field at an arbitrary position within layers j in terms of the incident plane wave $\bar{E}_0^+$ is given by [30, 136]:

$$\bar{E}_j(z) = \bar{E}_j^+(z) + \bar{E}_j^-(z) = (t_j^+ e^{i\xi_j z} + t_j^- e^{-i\xi_j z})\bar{E}_0^+. \tag{4.35}$$

The quantity that is of interest in the case of photovoltaic devices is the energy dissipation of the electromagnetic field in the material [136]. Thus, the time averaged absorbed power as a function of position is given by the following equation:

$$Q_j(z) = \frac{4\pi c \varepsilon_0 n_j k_j}{2\lambda} |\bar{E}_j(z)|^2, \tag{4.36}$$

where c is a speed of light, ε_0 is a permittivity of free space, λ is a wavelength, while n_j and k_j are the real and imaginary part of the complex index of refraction (see Eq. (4.16)), respectively.

To determine the exciton generation rate as a function of position in the thin film devices we used a code of the transfer-matrix method written in the group of Prof. M. D. McGehee [137]. The optical constants for the PFB and F8BT, which were determined using ellipsometry, were provided by Prof. N. Greenham [138]. We assumed that the solar cell multilayer consists of following layers:

SiO_2 | ITO | PEDOT:PSS | active layer | Al | air

After having performed the calculation and integrated the time averaged absorbed power $Q_j(z)$ over the wavelengths from 300 nm to 800 nm we obtained the position dependent exciton generation rate and according to this dependence the excitons were generated along the active layer of a PSC.

Chapter 5

Investigation of loss phenomena of block-copolymer-based solar cells

5.1 Introduction

As was already mentioned before, PSCs are a promising technology with great potential, due to their easy manufacturing, high flexibility, light weight and low production costs [64, 65]. Due to loss phenomena of the elementary particles occurring in the photovoltaic process, such as photon loss, exciton loss and charge carrier loss [68, 69], the power conversion efficiency of PSCs is still rather small compared to their inorganic counterparts with the highest efficiency reaching around 11 % [66]. These loss processes typically emerge at characteristic stages of the photovoltaic process, like e.g. photon absorption, exciton generation and diffusion to the D/A heterojunction, exciton separation and charge carrier generation at the D/A heterojunction, diffusion of the charge carriers to the respective electrodes and/or collection of the charge carriers at the electrodes [7, 69, 70]. For instance, an exciton can be lost from the system through radiative recombination, giving rise to photoluminescence, non-radiative exciton decay, providing a phonon or through the process of exciton-exciton annihilation, where upon the collision of two excitons one is annihilated, whereas the other used the energy from the collision to be promoted to a higher energy level [71, 72, 73]. Another type of small-scale annihilation phenomena, reducing the power conversion efficiency of PSCs, are related to charge carrier losses. These can be caused by the processes of charge recombination or charge trapping, in which charges are caught in a defect of the chain conformation or mesoscale morphology and may affect the free charges in close proximity [7, 74, 75, 76]. This leads to a lower charge carrier mobility and, ultimately, to a lower device performance. Despite the undeniable progress of the experimental tools in elucidating the causes deteriorating the photovoltaic performance of PSCs, it is still rather cost-intensive and time-consuming to perform extensive analyses of loss processes on a molecular or mesoscopic scale for polymer systems with changing chemical characteristics, like e.g. different molecular constitution of the monomers, chain architecture, or subjected to external influence, such as mechanical loading [7]. Further difficulties associated with the fact that experimental tools often do not provide reliable information about complex polymer systems on various length and time scales. In this regard, computer simulation techniques are a promising and powerful alternative to gain a deeper understanding of the physical processes underlying the operation of PSC nanodevices.

In the present chapter we study the causes affecting the loss processes of elementary particles involved in the photovoltaic process of PSCs with changing chemical characteristics and external conditions, imposed on the system. To this end, we apply the multiscale DMC-SCFT algorithm mentioned previously on systems composed of DA-diblock- and ADA-triblock-copolymers and compare their photovoltaic performance as a function of the interaction strength between the monomers, chain architecture as well as external mechanical loadings. Finally, we investigate the suitability of these polymer systems for the purpose of charge storage by analyzing their charge storage capacity as well as charge loading/unloading behavior.

5.2 Simulation details

In following calculations we considered systems composed of symmetric AB-diblock copolymers with polymerization indices $N_A = N_B = 20$ and of symmetric ABA-triblock copolymers with polymerization indices $N_A = 10$ and $N_B = 20$ [7]. In both cases we chose the statistical segment lengths as $b_A = b_B = b$. Moreover, we took a discrete lattice of size 64 × 64 with a spatial mesh width of Δ x = Δ y = 1 in units of b. For the numerical integration of the differential equation (see Eq. (2.23)), we used a contour step size of Δs = 1.0 and computed the free energies with a relative accuracy of 10^{-4}. For a detailed derivation of the SCFT method and description of its implementation, we refer to chapter 2. To compute the morphologies, we made use of the program package OCTA [82, 83].

To simulate the photovoltaic processes, we used our DMC algorithm for each of the morphologies. For a detailed description of the DMC-method we refer to chapter 4. In the following simulation study, we considered systems composed of ITO|AD-diblock or ADA-triblock|Al, where the A- and D-blocks consisted of (R1,R2)-substituted poly(perylene diimide-alt-dithienothiophene) ((R1,R2)-PPDI-DTT) and (R1,R3)-substituted bis (thienylene vinylene) - substituted polythiophene ((R1,R3)-biTV-PT), respectively, whereas ITO and Al correspond to the hole and electron extracting electrodes, respectively. In Fig. A.1, we visualize the chemical structures of these monomers. Moreover, we point out that R1, R2 and R3 represent alkyl substituents and that they are not connected to the π-system of the monomer cores and, thus, they do not affect the electronic structure of the polymers, which determines the parameters of the solar cell algorithm [7]. We will vary them in the following to change the effective interactions and, thus, the χ-parameter between the monomers without modifying the parameters of the solar cell algorithm. In the DMC calculations we set the system temperature to T = 298 K and used a lattice size of 64 × 64 sites in conjunction with a lattice constant of a_0= 1 nm [7]. The prefactor $\omega_e r_0^6$ = 2 nm^{6}ps^{-1} as well as exciton recombination rate ω_{dec} = 0.002 ps^{-1} were selected, to reproduce the experimental values of exciton diffusion length (∼10 nm) and lifetime (∼500 ps). By taking a reorganization energy of λ = 0.187 eV [120] and assuming that electrons and holes have equal mobilities $\mu_{e/h} = 10^{-3}$ cm^{2}V^{-1}s^{-1}, we determined the prefactor for the Marcus equation through Eq. (4.14) and set V_{hop} = 1.06 × 10^{-2}ps^{-1} for both charge carrier types. The electron-hole recombination rate was taken as $w_{rec} = 10^{-6}$ ps^{-1}. The standard deviation for the Gaussian density-of-states was chosen as σ = 0.062 eV. Moreover the Coulomb potential was cutted at r_c = 10 nm, whereas the difference in work functions of the electrodes was taken as $\Delta\phi_w$ = 0.5 V and the relative permittivity as ε_r = 3.5 [7, 32]. All the simulations were run up to 100000 generated excitons. Moreover, we considered the system to be equilibrated, when the deviations in the values of the exciton dissociation efficiency, charge transport efficiency and exciton lifetime did not exceed the preset error of 0.01 % within a certain time span in the production phase of the simulation [7].

5.3 Simulation of block-copolymer-based solar cells

We start our discussion by investigating the dependence of the photovoltaic properties of the polymer systems under consideration on the structural characteristics through varying their chemical composition and chain architecture [7]. In Fig. 5.1 we visualize the morphologies for a system of phase-separated (a) DA-diblock copolymers with block lengths $A_{20}D_{20}$ as well as (b) ADA-triblock copolymers with block lengths $A_{10}D_{20}A_{10}$ as a function of the Flory-Huggins interaction parameter χ, obtained with the static-SCFT method. From both graphs, we deduce that in the range from low up to intermediate χ-parameters the morphologies acquire an increasing degree of phase separation with decreasing interfacial length and change successively from unordered to lamellar-like structure [7]. In case of the diblock copolymer the morphology IV in Fig. 5.1 (a) possess a maximum number of continuous percolation paths to the electrodes, which are solely interrupted by a small number of dead ends. Moreover, it is worth mentioning, that starting from morphology IV up to morphology IX, we observe the creation of a growing number of dead ends and isolated inclusions. By contrast, in case of the triblock-copolymer system, a maximum number of continuous percolation paths to the electrodes is obtained for the morphology VI in Fig. 5.1 (b). Similarly as in case of the diblock-copolymer system, starting from morphology V up to morphology IX, we observe an increase in the number of defects and their transformation from dead ends to isolated inclusions. By further comparing the diblock- and triblock-copolymer morphologies and the results for the interfacial length, presented in Fig. 5.2 (c), we deduce that the phase thickness of the triblock copolymers are lower and that the triblock-copolymer nanostructures possess a larger interfacial length compared to the diblock-copolymers [7].

After having discussed the morphological aspects, in Fig. 5.2 (a,b) we analyze in the following the results for the internal quantum efficiency (IQE), exciton dissociation efficiency (EDE) and charge transport efficiency (CTE) for the systems composed of (a) DA-diblock copolymers as well as (b) ADA-triblock copolymers as a function of the χ-parameter, obtained with the DMC-SCFT method [7]. By comparing the results presented in Figs. 5.2 (a) and 5.2 (b), we conclude that the EDE of the triblock-copolymer system is always higher compared to the diblock-copolymer system over the whole range of χ-parameters. By further considering these results, we see that the difference in EDE's vanishes only in the limit of high χ-parameter. Moreover, we note that in case of the diblock-copolymer system the EDE curve reaches a minimum for the morphology V at a $\chi = 0.5$ and, then, slowly increases until $\chi = 0.9$, whereas in case of the triblock-copolymer system we observe two drops in the ranges $\chi = 0.3$ - 0.4 and $\chi = 0.6$ - 0.9. To explain the reasons for the reduction in the EDE, it is worth considering in the following the length of the DA-interface for both block-copolymer systems as a function of the Flory-Huggins interaction parameter as shown in Fig. 5.2 (c). A first aspect to note is that the interfacial length of the diblock-copolymer structures is lower compared to the triblock-copolymer structures over the

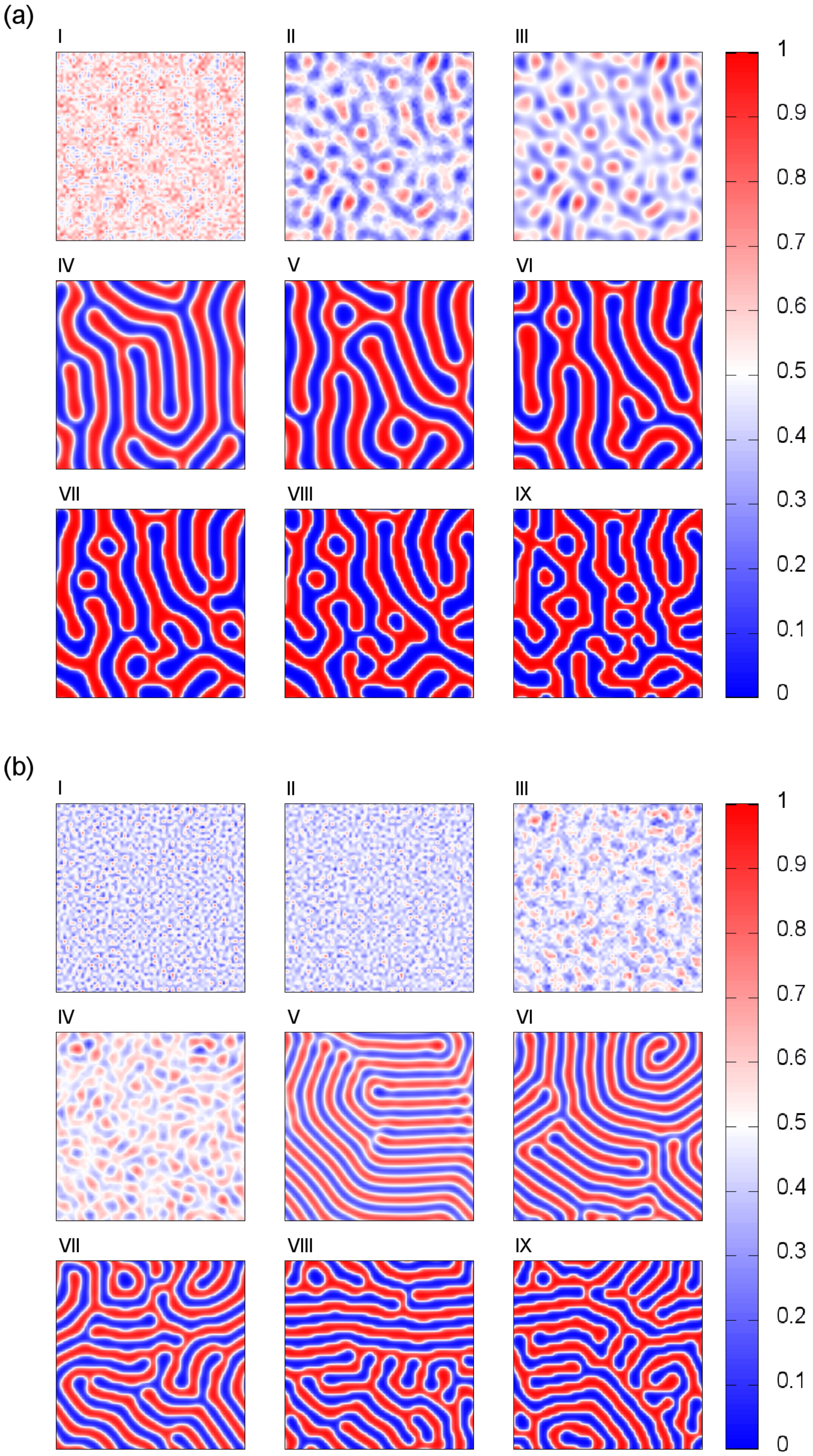

Figure 5.1: Volume fractions for a system composed of (a) $D_{20}A_{20}$-diblock copolymers or (b) $A_{10}D_{20}A_{10}$-triblock copolymers as a function of the Flory-Huggins interaction parameter, obtained with the static-SCFT method [red: majority of A phase (electron-conducting); blue: majority of D phase (hole-conducting)].

whole range of χ-parameters. As a result, the average distance the exciton has to travel before reaching the interface is lower in the latter case. Moreover, from the graph in Fig. 5.2 (c) we deduce that the difference in the EDE between diblock- and triblock-copolymer systems decreases quite strongly up to $\chi = 0.4$ and, then, undergoes only small changes up to $\chi = 0.9$. This shows that the large difference in the EDE between the triblock- and diblock-copolymer systems at low χ-parameters is partly due to the difference in size of the DA-interface, allowing a higher exciton dissociation in the former case [7]. Next, in Figs. 5.3 and 5.4 we consider

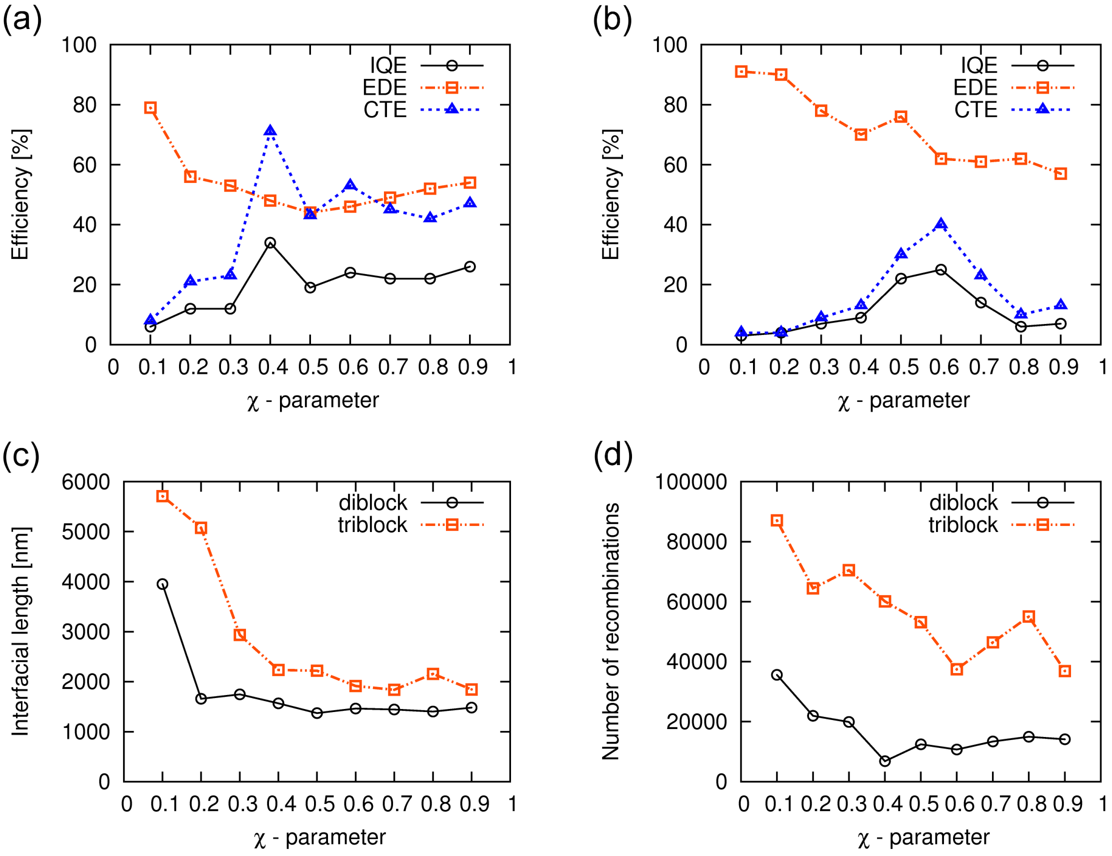

Figure 5.2: Internal quantum efficiency (black), exciton dissociation efficiency (orange), charge transport efficiency (blue) for a system composed of (a) $D_{20}A_{20}$-diblock copolymers or (b) $A_{10}D_{20}A_{10}$-triblock copolymers as a function of the Flory-Huggins interaction parameter, obtained with the DMC-SCFT method. Interfacial length (c) and total number of recombinations (d) for systems composed of $D_{20}A_{20}$-diblock copolymers (black) or $A_{10}D_{20}A_{10}$-triblock copolymers (orange) as a function of the Flory-Huggins interaction parameter.

the charge-density distribution and exciton-dissociation-frequency distribution for both block-copolymer systems as a function of the Flory-Huggins interaction parameter. These results indicate that the morphologies II-V of the diblock-copolymer system possess large regions of electron and hole accimulations, which in turn leads to a low exciton dissociation frequency, resulting in substantial charge losses [7]. By comparing these results to the corresponding morphologies in Fig. 5.1 (a), we further note that the main cause for these accumulations is that in this regime the morphologies have a large number of dead-end- and bottleneck-type of defects. We conclude from these observations that, in addition to the decrease of the interfacial length, charge accumulation in defects counteracts charge generation and, thus, provides an additional contribution to the loss of charges in case of these morphologies [7]. As a result, for a χ-value of 0.5 the EDE is decreasing to a minimum (see Fig. 5.2 (a)). By further analyzing the morphologies VI-IX in Fig. 5.3 (a), we see that the large regions of negative and positive charge accumulations vanish successively, which leads to a smooth increase of the EDE with increasing interaction parameter from $\chi = 0.6$ up to $\chi = 0.9$ as shown in Fig. 5.2 (a). Similar observations can be made for the triblock-copolymer system, where two drops in the EDE in the ranges $\chi = 0.3$ - 0.4 and $\chi = 0.6$ - 0.9 correlate well with the largest regions of electron and hole accumulations for morphologies III,IV (first drop) and VI-IX (second drop) as shown in Fig. 5.3 (b). Moreover, as can be inferred from Fig. 5.4 (b), these morphologies possess large regions, where the dissociation of excitons into free charges is very low or does not take place at all. In conclusion, we see that both the decrease of the interfacial length as well as a high charge accumulation are the primary factors for the deterioration of the EDE, which leads to an effective charge carrier loss and, thus, to a reduced IQE [7]. Next, in Figs. 5.2 (a) and 5.2 (b) we compare the CTE curves of the diblock- and triblock-copolymer systems, respectively. Starting from a χ-value of 0.1 the CTE curve for the diblock-copolymer system gradualy increases and reaches a maximum of 74 % at $\chi = 0.4$. Subsequently, the quantity starts to oscillate around a high CTE value of 50 % for a χ-parameter in the range of 0.5 - 0.9. By contrast, for the triblock-copolymer system the CTE passes through a maximum of 40 % at $\chi = 0.6$ and, then, decreases to around 10 % for higher χ-values. To elucidate the reasons for the lowering of the CTE after passing through the maxima for both block-copolymer types, we consider in the following the total number of recombinations as a function of the χ-parameter, depicted in Fig. 5.2 (d). After having analyzed these latter curves, we deduce that the minima in the total number of recombinations correlates with maxima in the CTE for both diblock and triblock copolymers. Moreover, it is worth mentioning that in case of the triblock-copolymer system the total number of recombinations possesses two minima of similar magnitude at $\chi = 0.6$ and $\chi = 0.9$, where the second minimum, however, results in a low CTE of only 15 %. To better understand the cause for such a low CTE, we analyze in Fig. 5.3 (b) the charge-density distribution for the triblock-copolymer system of the morphology IX. From this plot, we infer that the morphology IX has large regions of negative and positive charge accumulations throughout the whole nanostructure, provided by the dead-end- and bottleneck-type of defects. In contrast to this, in case of morphology VI we observe fewer regions of accumulated charges. Moreover, most of these charges are electrons and they are mainly accumulated in a spiral-like

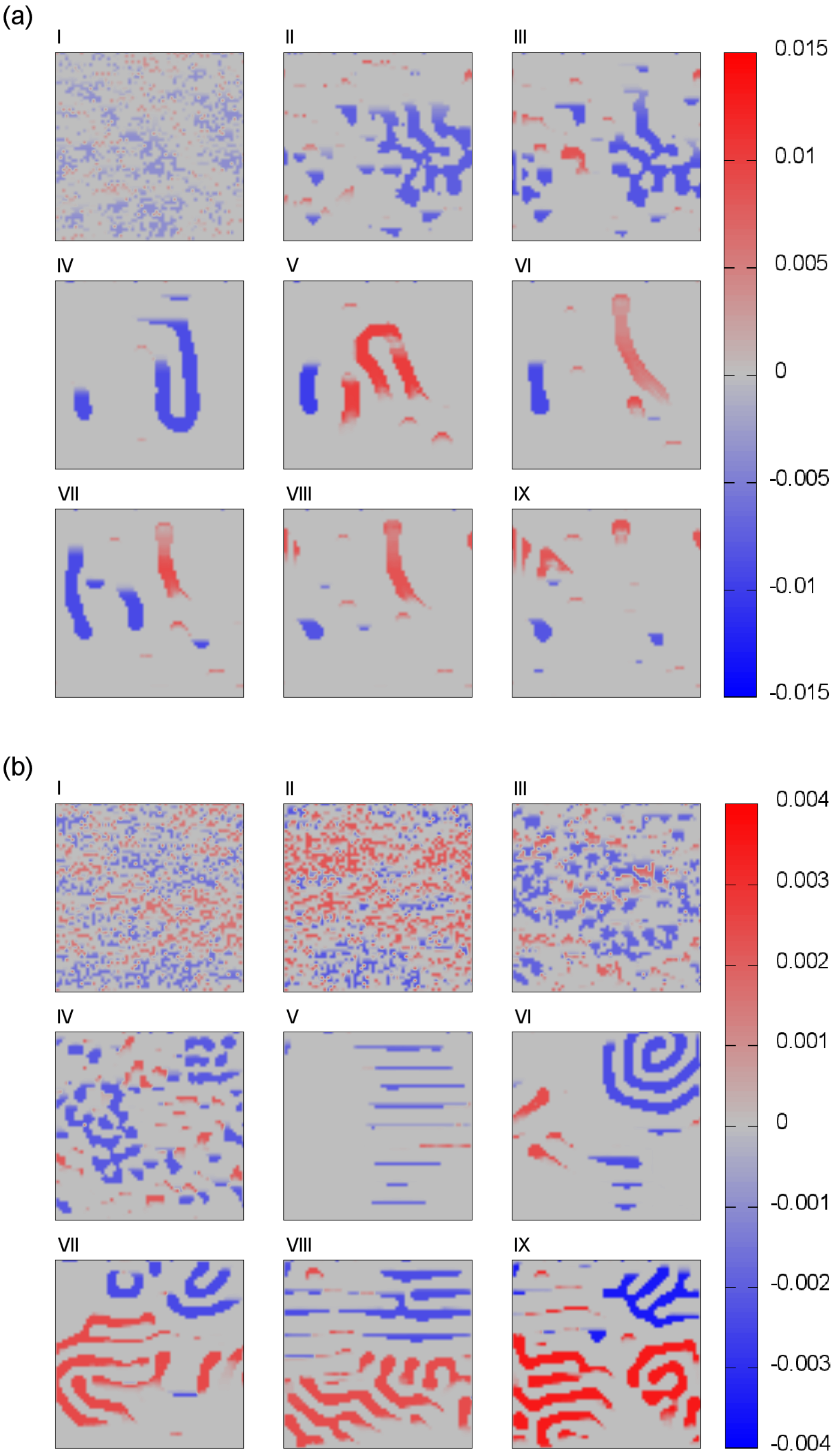

Figure 5.3: Charge density for a system composed of (a) $D_{20}A_{20}$-diblock copolymers or (b) $A_{10}D_{20}A_{10}$-triblock copolymers as a function of the Flory-Huggins interaction parameter, obtained with the DMC-SCFT method. Electrodes are applied in horizontal direction for all morphologies [blue: negative charge (electron); red: positive charge (hole)].

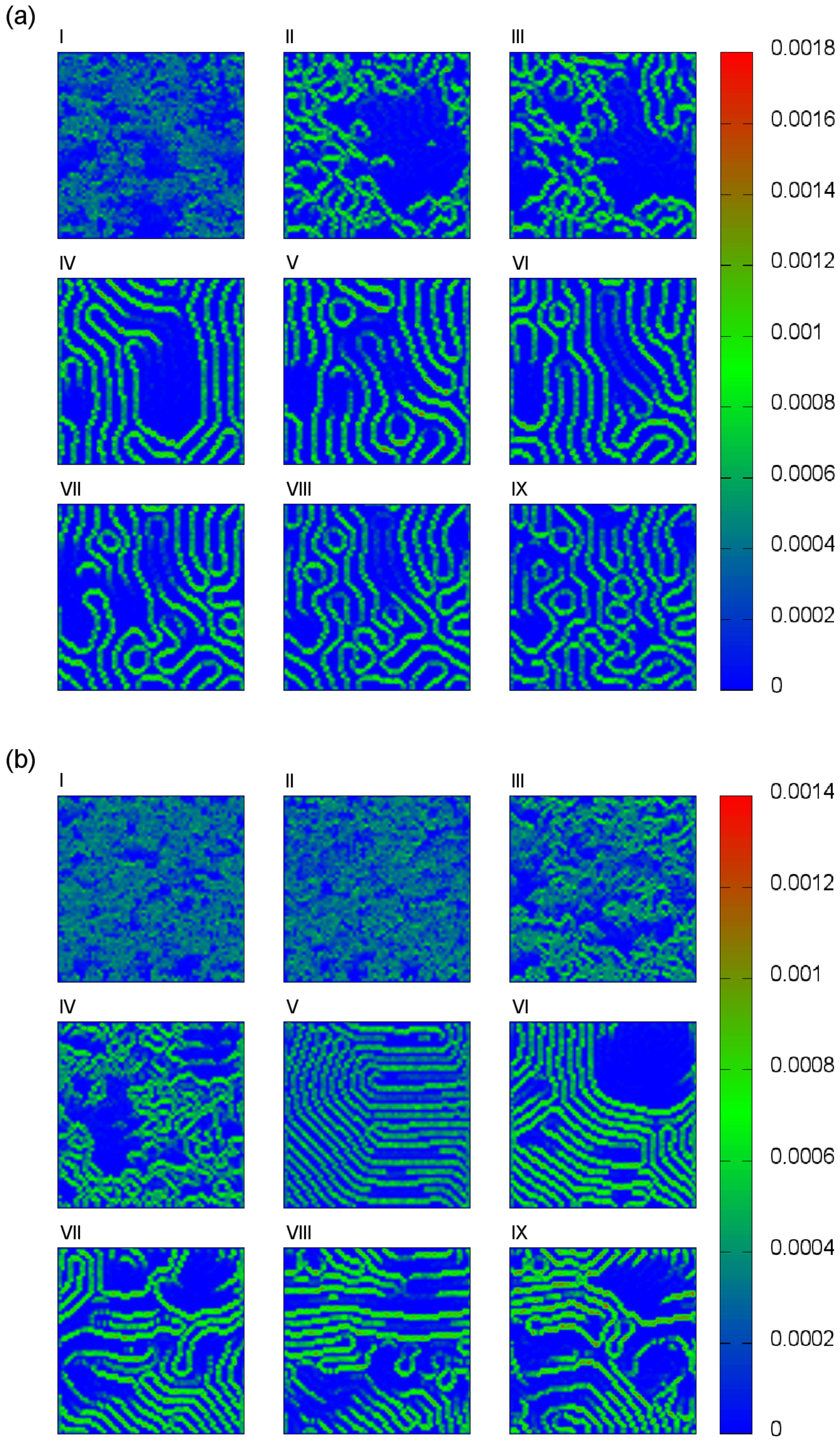

Figure 5.4: Frequency of exciton dissociation for a system composed of (a) $D_{20}A_{20}$-diblock or (b) $A_{10}D_{20}A_{10}$-triblock copolymers as a function of the Flory-Huggins interaction parameter, obtained with the DMC-SCFT method.

defect. From these findings, we conclude that these type of defects act as permanent charge traps, leading, besides the electron-hole recombinations, to additional charge losses and consequently to a further deterioration of the CTE. Moreover, we observe that charge-carrier trapping is promoted in dead-end-like nanostructures, where charges of opposite sign are captured nearby and attract each other through internal electrical fields, ultimately providing regions of strong charge accumulations as in case of the triblock-copolymer morphologies VII-IX [7].

In the following we study the physical characteristics, leading to charge trapping or charge recombination [7]. Common to both cases is that one type of charge carriers is slowed down or even fully hindered to reach the electrode by a bottleneck or dead end at the level of the mesoscale morphology, resulting in a local increase of the concentration of this charge-carrier type at this specific location [7]. Moreover, in case of the charge-trapping mechanism fast removal of charges of opposite sign in the adjacent phases and subsequent extraction at the respective electrode cause a lack of charges in this region of the defect, which disfavors the process of charge recombination with regard to the charge-accumulation process. These phases are generally characterized by direct percolation paths to one of the electrodes, allowing fast extraction of charges with opposite sign. By contrast, in case of the charge-recombination mechanism fast supply of opposite charges in adjacent phases causes a considerable number of charge recombinations, counteracting the process of charge accumulation [7]. In Fig. 5.5 (a) we show the charge-recombination number distributions of the diblock-copolymer system. From these plots, we observe a broad distribution of recombination events throughout the system for the morphologies I-III. This essentialy relates to the fact that these morphologies have a low degree of phase separation as well as a fine dispersion of D- and A-phases throughout the system, which leads to an increased number of geminate electron-hole recombinations. By further analyzing the plots in Fig. 5.5 (a), we infer that the morphology IV, which has the lowest total number of recombinations, possesses only a few localized sites with a high number of recombinations, which primary concentrate around the bottleneck-type of defects. In contrast, as was mentioned previously, with increasing χ-parameter the total number of defects increases as well, resulting in an increased number of sites, where the processes of charge recombination take place [7]. Similar observations can be made in case of the triblock-copolymer system. On one hand, by analyzing the morphologies I-IV in Fig. 5.5 (b), we observe a homogeneous distribution of charge-recombination events throughout the system, leading to a high total number of recombinations. On the other hand, with increasing χ-parameter, the degree of phase separation increases and the recombination events become more localized around the defects (see Fig. 5.5 (b)(V-IX)). In addition, by comparing the plots in Figs. 5.1 (a) and 5.1 (b) to the graphs in Figs. 5.2 (a) and 5.2 (b), we conclude that in case of both block-copolymer systems the morphologies with the largest number of continuous percolation paths and the highest degree of phase separation possess the highest CTE, i.e. morphology IV for the diblock-copolymer system and morphology VI for the triblock-copolymer system [7]. Finally, in Figs. 5.2 (a) and 5.2 (b),

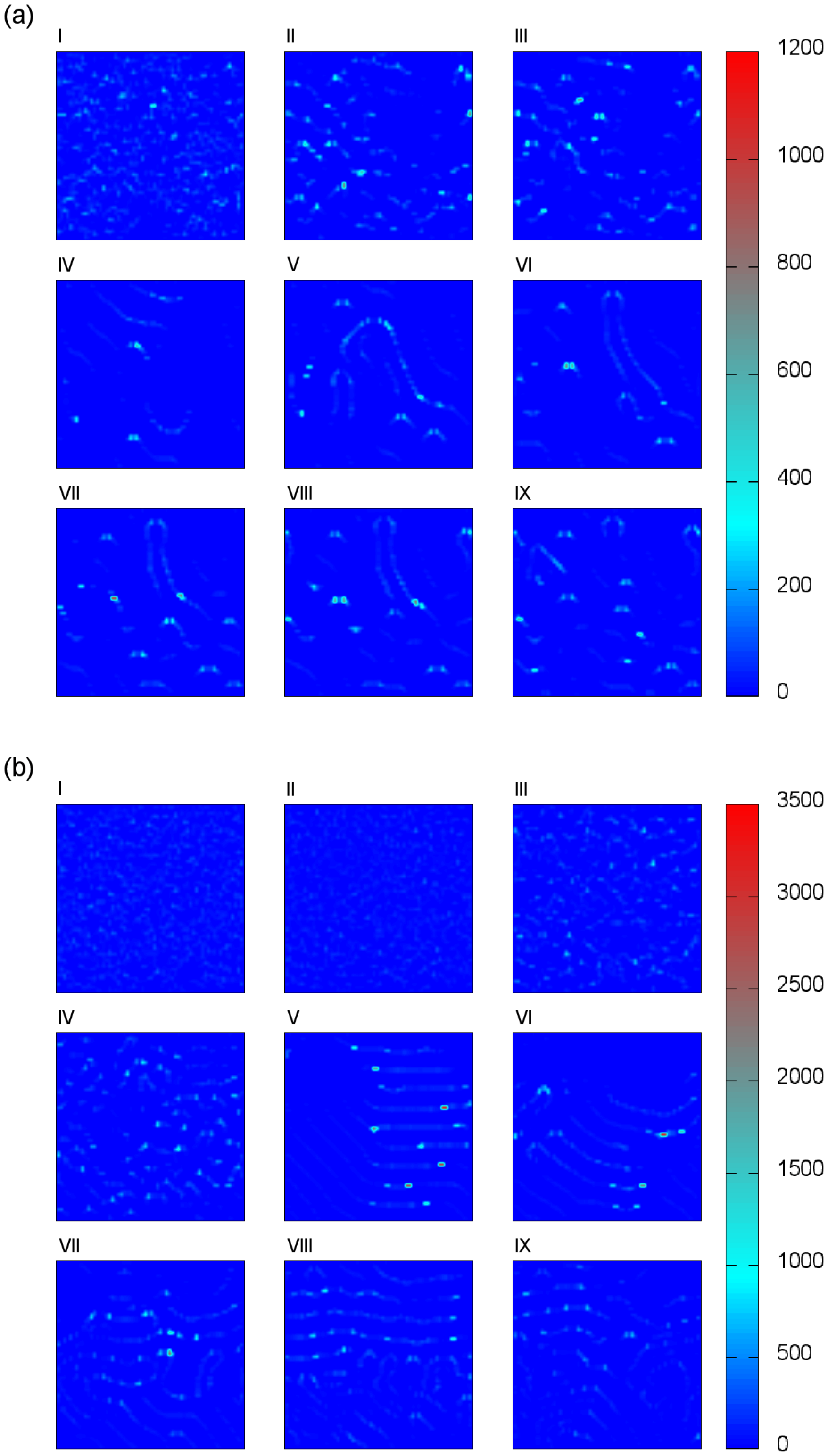

Figure 5.5: Charge-recombination number distribution for a system composed of (a) $D_{20}A_{20}$-diblock or (b) $A_{10}D_{20}A_{10}$-triblock copolymers as a function of Flory-Huggins interaction parameter, obtained with the DMC-SCFT method.

we show the values of the IQE's as a function of the Flory-Huggins interaction parameter for the diblock- and triblock-copolymer systems. By analyzing these results, we deduce that the IQE's for both block-copolymer types completely follow the functional dependence of the respective CTE's. However, both IQE curves are leveled down compared to the CTE curves by their respective EDE's. Moreover, we point out that the diblock-copolymer system has a slightly higher IQE compared to the triblock-copolymer system over the whole range of χ-parameters. This can be explained by the larger CTE in the diblock-copolymer case, which is not compensated by the higher EDE in the triblock-copolymer case [7].

5.3.1 Effect of mechanical load on the photovoltaic performance

Next, we analyze the impact of mechanical stress on the photovoltaic performance of triblock-copolymer systems, which are known to form stable networks of physical crosslinks conferring those materials useful properties for flexible nanodevice applications [7]. To this end, we show in Fig. 5.6 (a-c) the IQE, EDE and CTE for morphology VI of the triblock-copolymer system discussed previously as a function of the mechanical load at different bulk moduli of the D- and A-phases, obtained with the DMC-SCFT method. It is worth noting in this regard that, because we used the theory of linear elasticity in conjunction with the finite-element method, the mechanical loads applied here pertain to the linear regime of mechanical properties [7, 78, 79]. By analyzing the results in Fig. 5.6 (a), we infer that the IQE's of all block-copolymer systems decrease moderately at a value for the mechanical load of 0.1 $\mathrm{N/m^2}$. By increasing the mechanical load up to a value of 0.6 $\mathrm{N/m^2}$, the quantity stabilize by performing small- up to medium-sized oscillatory changes. Moreover, it is worth mentioning that the magnitude of these oscillatory changes strongly depends on the moduli of the D- and A-phases. We point out in this context that our findings are confirmed by the recent mechanical measurements of Kaltenbrunner *et al.* [7, 80] on ultrathin bulk heterojunction PSCs composed of poly(3-hexylthiophene) (P3HT) and (6,6)-phenyl-C61-butyric-acid-methyl ester (PCBM). These authors found through cyclic compression and stretching of their samples to 50 % a gradual decrease in power up to 27 % after 22 cycles, leading to a successive degradation of the photovoltaic performance of the material. By further analyzing the results in Fig. 5.6, we see that the IQE curves possess a similar functional behavior as the corresponding CTE curves. In contrast to this, the EDE's perform only moderate deviations from the initial value of 62.5 % over the whole range of mechanical loads. This demonstrates that in this range of parameters the dependence of the IQE on the mechanical changes is mainly influenced by the CTE, however it is only marginally affected by the EDE [7]. To better understand the causes for the deterioration of the CTE with increasing mechanical load, we show in Fig. 5.6 (d) the total number of recombinations as a function of the external mechanical load at different bulk moduli for the D- and A-phases. From these plots, we deduce that at small mechanical loads the curves for the total number of recombinations strongly increase for all systems with different bulk moduli and afterwards they reach a plateau, which correlates with the reduced supply of opposite charges enabling charge recombination in proximity of the dead-end- or bottleneck-type of defects. The local deformation of the nanophases,

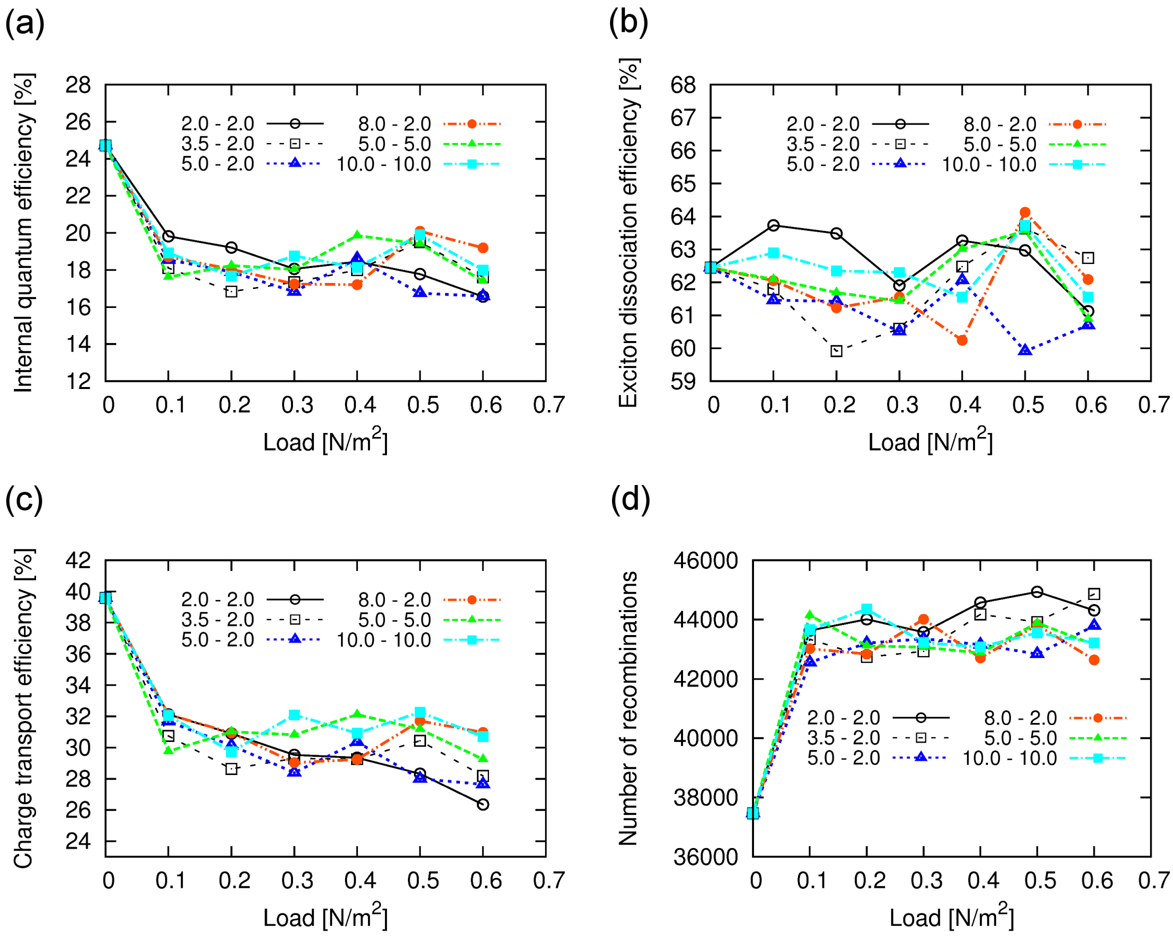

Figure 5.6: (a) Internal quantum efficiency, (b) exciton dissociation efficiency, (c) charge transport efficiency as well as (d) total number of recombinations for a system composed of $A_{10}D_{20}A_{10}$-triblock copolymers as a function of the external mechanical load at different bulk moduli for the D- and A-phases, obtained with the DMC-SCFT method. Note that the mechanical loads were applied on the morphology VI of the triblock-copolymer system, which is the morphology with the highest internal quantum efficiency.

due to the stretching of the morphologies, is strongly influencing the effectiveness and type of loss mechanism experienced by the charges in the defects [7]. In order to confirm this, we show in Figs. A.2 - A.7 the volume fractions of the strained morphologies at mechanical loads of 0.1 N/m^2 and 0.5 N/m^2 in conjunction with the corresponding charge density distributions as well as frequencies of exciton dissociation. Moreover, from Figs. 5.6 (c) and 5.6 (d) we infer that at a load of 0.5 N/m^2 the CTE curves of the morphologies with K_A= 5.0 GPa, K_D = 2.0 GPa and $K_A = 2.0$ GPa, $K_D = 2.0$ GPa possess almost the same values, despite a strongly differing number of electron-hole recombinations. This indicates that, under these conditions, a large number of charges are lost due to a loss process other than the charge-recombination process [7]. In order to find a cause for this, we consider next the charge-density distributions of the corresponding strained morphologies in Fig. A.5. By analyzing these results, we infer that in case of the morphology III there is a region of strong electron accumulation in the upper-left part of the plot, whereas in all other cases we do not observe this phenomenon. In addition, from Fig. A.3, we deduce that this region is a part of the spiral-like defect, where the transport of the electrons to the respective electrode is hindered by the dead ends. Due to the lack of opposite charges in this part of the system, charge losses due to charge recombinations become less probable, whereas charge losses due to charge trapping, going along with a deterioration of the exciton dissociation, are favored. The latter conclusion can be drawn from Fig. A.7, where a reduction of the exciton dissociation frequency is observed in the region of negative charge accumulation mentioned previously. As a consequence, these additional loss processes cause that the strained morphology III possesses the lowest EDE, CTE and IQE of all morphologies at a load of 0.5 N/m^2, whereas their effective suppression in case of morphology IV with $K_A = 8.0$ GPa, $K_D = 2.0$ GPa leads to the highest efficiencies at the same load [7].

5.3.2 Charge storage media

To conclude this chapter, we investigate in the following the suitability of the polymer systems to be used as charge storage media. It has been shown previously that in some of the nanostructured morphologies a significant amount of charges is accumulated [7]. For instance, in case of the triblock-copolymer morphology IX we observed strong negative and positive charge accumulations, as a result of attraction of the nearby captured electrons and holes through internal electric fields. By assuming that these charges could be stored for a certain period of time and afterwards regained through a change of the environmental conditions, we conjecture that these systems could be used for the purpose of charge storage. To investigate this aspect in more detail, we show in Fig. 5.7 (a) the total number of charges as a function of the charging or uncharging time during the process of charge loading or charge unloading of the morphology IX. The charging of the system is accomplished by carrying out the photovoltaic process, whereas uncharging is achieved by reversing the polarity of the net electric field after the charging process has been completed [7]. At the beginning of the charging process, we observe a significant increase in the total number of charges. Starting from a time of ~ 0.0025 s this quantity reaches a plateau with an average amount of charges of around 800. Moreover, we point out that the end of the charging process corresponds to a stationary solution of the DMC algorithm. In case of the uncharging process, by contrast, we see that the total number of charges possesses a regime of fast decrease up to a simulation time of 10^{-7} s, which is followed by a regime of slow decay in the time range from 10^{-7} s up to 10^{-6} s. In the final stage the curve attains a plateau with a total number of 350 charges, which relates to the fact that some of the charges remain trapped in the defects and, thus, cannot be extracted from the device [7]. This observation is further confirmed by the plots in Fig. 5.7 (b), where we show the charge density distributions of morphology IX, obtained after the (I) charging- and (II) uncharging-process respectively.

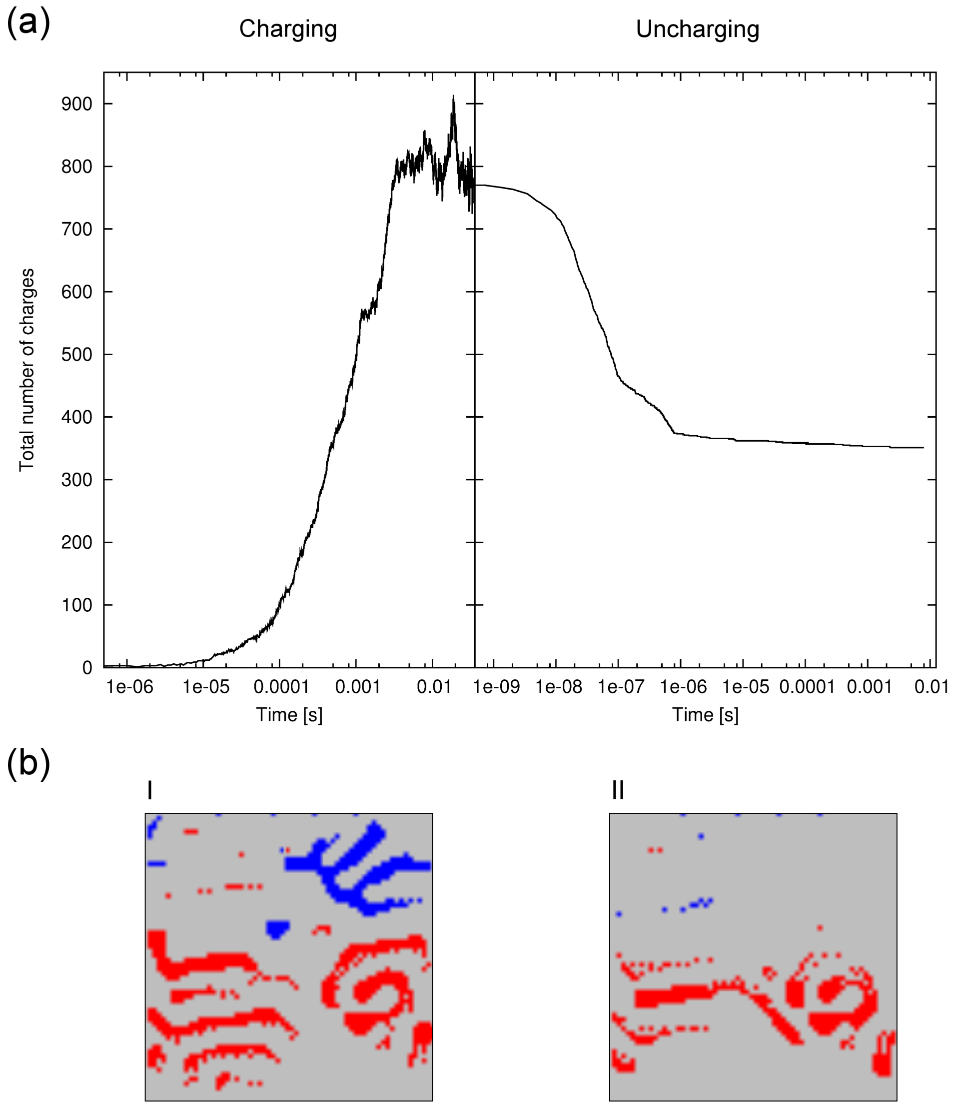

Figure 5.7: (a) Total number of charges during charging- or uncharging-process as a function of time and (b) charge density distributions after (I) charging- or (II) uncharging-process for morphology IX of a system composed of $A_{10}D_{20}A_{10}$-triblock copolymers, obtained with the DMC-SCFT method. Electrodes for this morphology were applied in horizontal direction.

As can be inferred from comparing these two figures to the corresponding morphology IX in Fig. 5.1 (b), the major part of the accumulated electrons and holes could be extracted from regions with direct percolation paths to the electrodes. In contrast to this, regions with dead-end- or bottleneck-type of defects possess a large fraction of holes, which remain captured and, as a result, these charges are hindered to reach the respective electrode. Finally, it is worth mentioning that these trapped charges can only decay through the process of charge recombination and, thus, cause a decrease of the charge storage efficiency of the device [7].

Chapter 6

Improving the solar-cell performance of polymer bulk heterojunctions

6.1 Introduction

Despite the significant progress in the development and experimental characterization of PSCs, their power conversion efficiencies are still significantly lower than their inorganic counterparts, such as silicon or CdTe [84]. One of the main causes for the low power conversion efficiency of PSCs is their low charge carrier transport efficiency to the electrodes. Charge transport can be limited by charge trapping phenomena, originating from impurities and defects [85]. For instance, during thermal deposition of aluminum cathode the hot Al atoms can diffuse into the photoactive layer, which leads to its degradation and generation of unwanted trap sites [31]. Krebs *et al.* [86] showed through time-of-light secondary ion mass spectrometry (TOF-SIMS) that both Al from the cathode and In from the anode diffuse through the entire device and, thus, contribute to the degradation of the active layer. Furthermore, due to the random distribution of the donor and acceptor material in the bulk heterojunction, these impurities may self-organize into isolated islands, resulting in a deterioration of the transport of the charge carrier to the electrodes.

Several approaches have been proposed to enhance the power conversion efficiency of PSCs by controlling the bulk heterojunction nanostructure. For example, processing parameters, such as the choice of the solvent, evaporation rate or blend composition, have a high impact on the nanoscale morphology [87]. Other useful approaches to optimize PSCs are the post-production techniques, such as thermal, solvent-assisted and vapor annealing, electric field alignment. In particular, thermal or solvent-assisted annealing leads to a vertical phase-segregation within the film, which in turn leads to the formation of better percolation pathways through the morphology, resulting in a more efficient and balanced transport of free charges to the electrodes. This effect has been investigated by electron tomography by van Bavel *et al.* [88]. However, for the industrial production of low-cost plastic solar cells it is technologically more favorable to use large area and low-temperature fabrication processes [89]. An alternative method to thermal annealing is simply to apply a direct current (DC) electric field perpendicular to the substrate. Under the influence of an electric field, the photoactive layer provides more efficient transport paths for holes and electrons through alignment of the nanophase of the morphology. This has been examined e.g. by Lin *et al.* [89], through bright-field (BF) transmission electron microscopy (TEM). Moreover, other experimental results show that polymer chains orient in direction of the applied electric field, which in turn leads to the improvement of the charge carrier mobility and photovoltaic performance [90, 91].

Finally, it is also worth mentioning that the specific interaction between the materials of an active layer and the substrate also have a strong effect on the morphology. For example, Arias *et al.* [92] developed a technique to modify the organic surfaces, like PEDOT, using microcontact printing of self-assembled monolayers (SAM). The work of Arias *et al.* together with other experimental results clearly demonstrate that surface energy control can be used to promote vertical phase separation, which leads to increased charge carrier transport to the electrodes and enhanced performance of the PSCs [67, 92, 93, 94].

Despite the progress of experimental methods in elucidating the effects influencing the photovoltaic performance of PSCs, it is still difficult to investigate the processes taking place on the local scale, due to the poor resolution and sensitivity of conventional experimental measurement tools. In this regard computer simulation techniques can provide a powerful alternative for the study of a large number of interesting phenomena, occurring in polymeric systems on various length and time scales. Besides, simulation techniques can provide reliable information for a deeper understanding of the physics of polymer nanodevices. For instance, Matsen [95] has investigated the electric field alignment of cylinder-forming diblock-copolymer systems, using SCFT. He has shown that an electric field possesses a significant stabilizing effect on a morphology, where cylinders orient perpendicularly to the plates. In another work, Chervanyov *et al.* [96] used SCFT to investigate the effect of spherical and sphero-cylindrical fillers on the order-disorder transition of a symmetric diblock-copolymer melt. They found that the particles with the smaller aspect ratio, i.e. increased cylindrical shape, have a large effect on the order-disorder transition. In our recent works [7, 69] we have extended the range of application of the field-theoretic methods to investigate the loss processes of charge carriers and excitons in nanostructured PSCs.

To elucidate the parameters influencing solar-cell performance, we will analyze in the following post-production treatments, such as electric field alignment and influence of surface interactions on the PSC nanostructures. Moreover, we will investigate the influence of impurities on the stability and performance of diblock-copolymer solar cells. To this end, we will apply the mustiscale DMC-SCFT algorithm, described in section 4.3.3, on systems composed of A_5D_{15}-diblock- and $A_3D_{12}A_3$-triblock-copolymers.

6.2 Dynamic-SCFT under the influence of an applied electric field for block-copolymers

In our study we used a dynamic-SCFT to describe the phase transformation of the block-copolymer systems as a function of time under the influence of an applied electric field [99, 100, 101]. The systems we studied were AD-type diblock- and ADA-type triblock-copolymer melts. The AD (ADA) diblock (triblock) copolymer consisted of N_A segments of A-type and N_D segments of D-type monomers. The total number of statistical segments was given by $N = N_A + N_D$ for the diblock-copolymer melt, as well as $N = 2N_A + N_D$ for the triblock-copolymer melt. Under the influence of a DC-electric field, the dynamic of the phase separation process can be described by an anisotropic diffusion type equation of the form [102]:

$$\frac{\partial}{\partial t}\phi_K(\mathbf{r},t) = L_K\nabla^2\mu_K(\mathbf{r}) + \alpha\frac{\partial^2}{\partial z^2}\phi_K(\mathbf{r},t), \tag{6.1}$$

where ϕ_K is the local volume fraction of blocks of K-type ($K = A$ or D) at position $\mathbf{r}$ and time t [99, 100, 101]. Moreover, L_K is the mobility and it is taken to be the same for all components. Note that the system is assumed to be incompressible, $\phi_A + \phi_D = 1$, and that the electric field is applied in z-direction of the box. The chemical potential of a K-type block is defined as $\mu_K = \delta F/\delta\phi_K$, where F is the free energy of the system given by [12, 100, 103]:

$$F/k_BT = -M\ln Z - \sum_K\int d\mathbf{r}\ \phi_K(\mathbf{r})V_K(\mathbf{r}) \quad + \tag{6.2}$$

$$\frac{1}{2}\sum_K\sum_{K'}\int d\mathbf{r}\chi_{KK'}\phi_K(\mathbf{r})\phi_{K'}(\mathbf{r}) \quad + \quad \sum_K\int d\mathbf{r}\chi_{KW}\phi_K(\mathbf{r})\delta(\mathbf{r}-\mathbf{R}),$$

where k_B is Boltzmann's constant and T is the absolute temperature. In this expression the first term is the contribution from the conformational entropy of the chains, where M is the total number of polymer chains in the system and Z is the partition function of a single block-copolymer chain. The second term represents the external potential $V_K(\mathbf{r})$, acting on a K-type segment at position $\mathbf{r}$. The third term includes the pair interaction between segments of different type, where $\chi_{KK'}$ is the Flory-Huggins interaction parameter, and the final term defines the interaction parameter between segments and the surfaces, with χ_{KW} as the interaction parameter of polymer blocks with the wall, where the surfaces are represented as hard walls (W), whose position $\mathbf{R}$ is specified by the Dirac delta-function δ($\mathbf{r}$ - $\mathbf{R}$) [100, 104].

We note that the uniformly applied electric field E_0 enters the diffusion equation in Eq. (6.1) through the dimensionless parameter $\tilde{\alpha}$, defined as [99, 105]:

$$\tilde{\alpha} = \frac{\alpha}{k_BTL} = \frac{\varepsilon_0(\varepsilon_A - \varepsilon_D)^2}{\varepsilon_A f + \varepsilon_B(1-f)}\frac{E_0^2\nu}{k_BT}, \tag{6.3}$$

where $\alpha = L\nu g_e$ with ν as the volume of a single polymer chain and $g_e = \varepsilon_0\varepsilon_1^2E_0^2/\bar{\varepsilon}$, where $\bar{\varepsilon} = \varepsilon|_{\phi_A=f}$ and $\varepsilon_1 = (\partial\varepsilon/\partial\phi_A)|_{\phi_A=f}$. Both parameters ε_A and ε_D correspond to the dielectric constants of pure components, while ε_0 is the vacuum permittivity and f is the average volume fraction of the K-type blocks.

To compute the morphologies of the phase transformation process at different times and equilibrium morphologies, we made use of the previously described dynamic-SCFT and already described in chapter 2 static-SCFT, respectively.

6.3 Validation of the dynamic-SCFT method

To assess the reliability of the dynamic-SCFT method, we have investigated an electric-field-induced sphere-to-cylinder transition in a diblock-copolymer melt, with a molecular architecture A_5D_{15}. After a short time when we applied an electric field with strength $\tilde{\alpha} = 0.25$, stretching of spheres into ellipsoids occurred (see Fig. 6.1 (B)). From time $t = 10$ up to time $t = 750$ the ellipsoids were further stretched resulting in the interconnection and formation of straight cylinders (see Fig. 6.1 (C)).

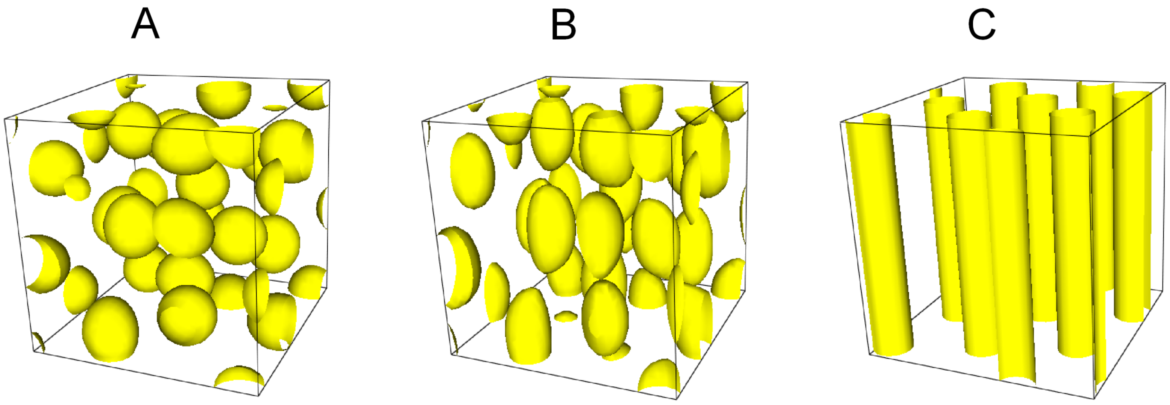

Figure 6.1: Morphologies of A_5D_{15}-diblock-copolymer system for different strength of an electric field ($\tilde{\alpha}$) obtained with a dynamic-SCFT: (a) initial structure, (b) $\tilde{\alpha} = 0.25$, $t = 10$ (c) $\tilde{\alpha} = 0.25$, $t = 750$.

Due to the conservation of volume of the A-phase, diameters of the cylinders are smaller than the diameters of the spheres. These observations agree well with the experimental results of Xu *et al.* [97, 98], who visualized with the help of cross-sectional transmission electron microscopy (TEM) the intermediate stages of the alignment process. They showed that in the first stage the spherical microdomains were deformed into the ellipsoids and, then, they were interconnected to cylinders, oriented in the direction of the field. From this observations they concluded that the electric-field-induced sphere-to-cylinder transition is an effective method for controlling the orientation of microdomains and for generating highly ordered cylindrical nanostructures.

6.4 Simulation details

In the following we provide all parameters, which were used for the SCFT calculations, presented in the section 6.5.

To study the influence of an electric field on the nanoscale structure of diblock-copolymer solar cells, we considered a system composed of polymers with a molecular architecture A_5D_{15}. For the generation of the morphology, we used a DA-interaction parameter of $\chi_{AD} = 1.0$ and a polymer segment fraction of the acceptor of $f_A = 0.25$, whereas the statistical segment length was taken as $b_A = b_D = b$ (that is taken to be unity). The simulation box was constituted of 32 × 32 × 32 grid points with a spatial mesh width of $\Delta x = \Delta y = \Delta z = 0.5$ in units of b. The periodic boundary conditions were applied along the x- , y- as well as z-direction. The contour-step size along the chain was chosen as $\Delta s = 0.25$ and the relative accuracy for the computed free energy as 10^{-4}. For the numerical integration, we used a time step of $\Delta t = 0.01$ and the mobility as $L_K = L = 1.0$.

To investigate the effect of an electric field on triblock-copolymer solar cells, we considered a system with a molecular architecture $A_3D_{12}A_3$. The simulation parameters were the same as for the case of the diblock-copolymer system mentioned previously, excepting for the enthalpic interaction parameter $\chi_{AD} = 1.338$ and the polymer segment fraction of the A-blocks $f_A = 0.33$.

In the next investigation we studied the influence of an electric field in the presence of surface interactions on a block-copolymer solar-cell system, containing $A_3D_{12}A_3$-triblock copolymers. For these calculations, we took the same parameters as for the previously mentioned triblock-copolymer system. The only difference was in the Flory-Huggins interaction parameter, for which we selected a value of $\chi = 1.65$.

In the last study we analyzed the impact of impurities on the photovoltaic performance of block-copolymer solar cells. To this end, we performed static-SCFT simulations with a diblock-copolymer melt of molecular architecture A_5D_{15}. For the calculations, we took the Flory-Huggins interaction parameter $\chi = 1.0$ and $f_A = 0.25$. Moreover, we used a simulation box of 50 × 50 × 50 grid points with a spatial mesh width of $\Delta x = \Delta y = \Delta z = 0.5$. The periodic boundary conditions were applied along the x- , y- and z-direction. The contour-step size along the chain was chosen as $\Delta s = 0.25$ and the relative accuracy for the computed free energy as 10^{-4}. In our simulations the impurities were represented as spherical particles with hard walls.

The A- and D-blocks of block-copolymer systems, considered in this chapter, consisted of poly(perylene diimide-alt-dithienothiophene) (PPDI-DTT) and bis(thienylenevinylene) - substituted polythiophene (biTV-PT), respectively. For the DMC-calculations, we used the same parameters as in chapter 5.

6.5 Di- and triblock-copolymer melt under the influence of an electric field

6.5.1 A_5D_{15}-diblock-copolymer melt

The low charge transport efficiency to the electrodes is one of the key factors limiting photovoltaic performance of PSCs. From the literature it is well known that an applied electric field can be used as a post-production treatment for the improvement of the charge transport efficiency and photovoltaic performance [89, 90, 91]. In our work the electric field post-production technique has been used to improve the efficiency of solar cells based on organic block-copolymers.

We start our discussion by considering an asymmetric diblock-copolymer system with the molecular architecture A_5D_{15}. First of all, we performed the simulation without an electric field with the parameters mentioned previously in order to generate an initial bulk structure. To this end, we let our simulation run up to a time of $t = 3000$. In Fig. 6.2 (A) we visualized the morphology obtained from the dynamic-SCFT simulation [106, 107]. This spherical structure was used as a starting configuration for the subsequent alignment simulation with an electric field. In Fig. 6.3 (a,b,c,d)(A) we show the results for the internal quantum efficiency (IQE), exciton dissociation efficiency (EDE), charge transport efficiency (CTE) and recombination efficiency (RE) for the corresponding structure, obtained with the DMC-SCFT method. Since the spherical morphology does not have any continuous percolation pathways to the electrodes the CTE as well as the IQE approach zero (see Fig. 6.3 (a,b)(A)). This results in a large number of charge-carrier losses, due to a high number of charge recombinations, as confirmed in Fig. 6.3 (d)(A), and charge accumulations. Around 93 % of generated charges recombine before reaching the electrodes, due to the lack of percolation pathways. Moreover, the accumulations lead to a strong decrease of the exciton dissociation into free charges, because they are counter-balancing the exciton generation, even though the interfacial area for the spherical structure is not the lowest (see Fig. 6.4 (a)).

Next, in Fig. 6.2 we consider the dynamic evolution of the mesoscale structure for the given diblock-copolymer system as a function of time under the influence of an external electric field with strength $\tilde{\alpha} = 0.25$. In the early stage of the alignment a disordered array of spheres stretch into ellipsoids and interconnect through the formation of deformed cylinders, resulting in the morphology B. We note that these cylinders are not oriented in the direction of the field. With increasing simulation time the cylindrical microdomains become oriented along the electric field lines, leading to the morphology with straight cylinders, as depicted in Fig. 6.2 (G). As a result of this phase transformation from the initial spherical morphology up to the final structure, the CTE is increasing from 5 % to 90 % (see Fig. 6.3 (b)). This can mainly be attributed to the increase in the number of percolation pathways, resulting in an efficient and balanced transport

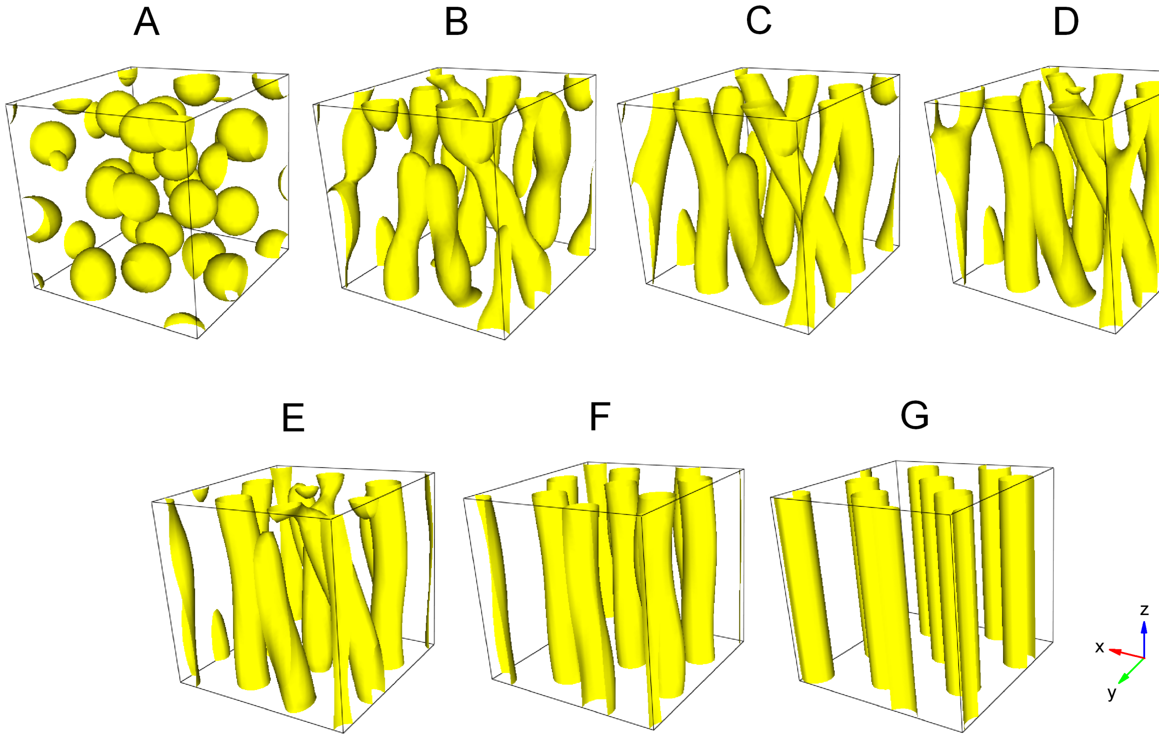

Figure 6.2: Morphologies of A_5D_{15}-diblock-copolymer system as a function of time under the influence of an electric field with strength $\tilde{\alpha} = 0.25$. Time $t =$ (A) 0; (B) 20; (C) 70; (D) 120; (E) 160; (F) 210; (G) 750. Here and in all other figures with morphologies of this chapter the iso-surface level is $\phi_A = 0.5$ and the direction of the axes as shown in the right bottom angle.

of electrons and holes to the electrodes.

Starting from time $t = 20$ up to time $t = 120$ the IQE increases (see Fig. 6.3 (a)). The main cause for the increase of the IQE comes from the rise of the CTE, which itself increases as a result of the successive alignment of the cylinders in direction of the electric-field lines (see Fig. 6.2 (B-D)). In the latter stage of the transition at time $t = 160$ (morphology: E) we observe a small decrease in the IQE mainly due to the decrease of the EDE, due to a lower interfacial area compared to the morphologies C and D (see Fig. 6.4 (a)). Moreover, it should be noted that the interfacial area in case of the morphologies C, D and E is larger compared to the interfacial area of the structure F, but, as can be seen from Fig. 6.3 (c), the difference in the EDE's for the morphologies C, D, E and F is very small. This relates to the fact that the morphologies C, D and E possess large regions of negative charge accumulations, provided by dead-end-type of defects. As a consequence, these regions are characterized by a low exciton dissociation frequency. For the structure F, we do not have such type of defects and, thus, this leads to an EDE, which is large compared to the morphology E and just slightly lower than in case of the

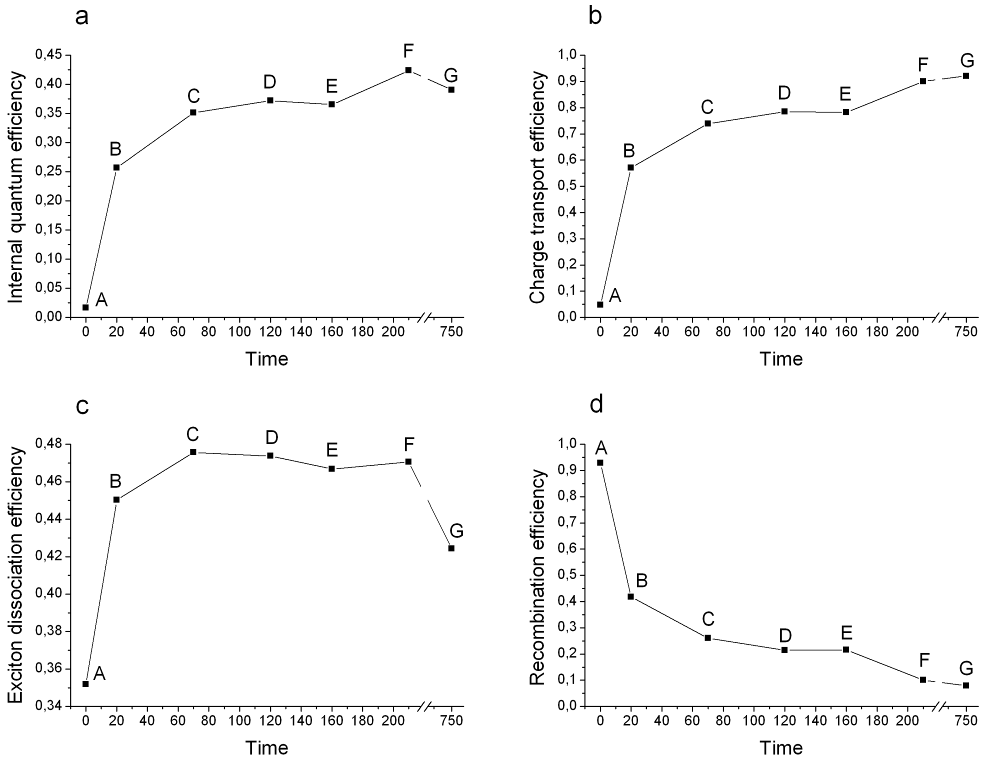

Figure 6.3: Efficiencies of A_5D_{15}-diblock-copolymer system as a function of time under the influence of an electric field with strength $\tilde{\alpha} = 0.25$. The electrodes are placed normal to the z-direction of the box.

morphologies C and D. Next, by comparing morphology F and G in Fig. 6.2, we deduce that both systems possess a cylindrical structure and both have continuous percolation paths to the electrodes. The only difference between them is that the morphology F in Fig. 6.2 is weakly curved and this fact has an impact on the CTE and EDE. From Fig. 6.2, we further infer that the CTE is higher in case of the structure G than in case of structure F, due to a lower RE (see Fig. 6.3 (b,d)(F,G)). To explain the reasons for the lowering of the RE, it is worth considering in the following the possible mechanisms of separation of a bound electron-hole pair into free charges. For the morphology G in Fig. 6.2 separation is always perpendicular to the field resulting from the difference in work functions of the electrodes, whereas the structure F in Fig. 6.2 has interfaces at angles slightly deviating from 90 °. As was recently shown by Kimber *et al.*, the charge hopping rate and angle of hop with respect to the field have a sinusoidal relationship [37]. Hence, if initial separation of charges is against the field (field-impaired separation) they have higher probability to recombine compared to the perpendicular situation and oppositely, if initial separation of charges is along the field (field-assisted separation), the probability to recombine is lower compared to the perpendicular situation [41]. Kimber *et al.* showed that the

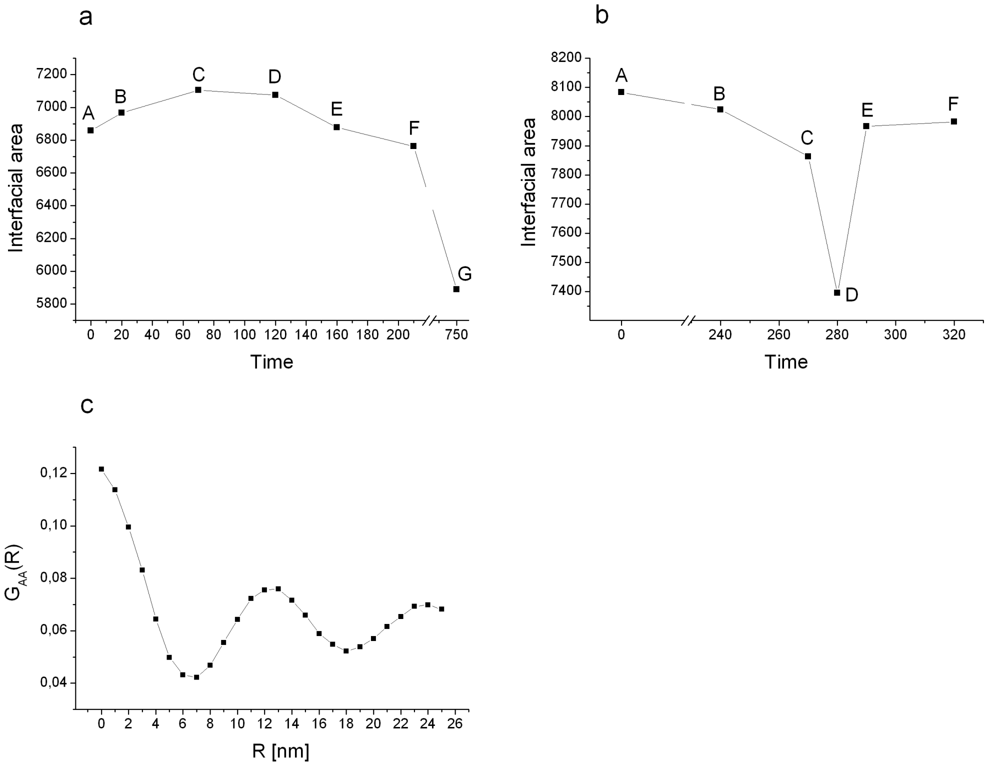

Figure 6.4: Interfacial area of A_5D_{15}-diblock-copolymer system (a) and $A_3D_{12}A_3$-triblock-copolymer system (b) as a function of time under the influence of an electric field with strength $\tilde{\alpha} = 0.25$ and $\tilde{\alpha} = 1.0$, respectively. (c) The spatial correlation function of A_5D_{15}-diblock-copolymer system consisting of perpendicular straight cylinders.

effect when the charges are trying to find a way out from the interface in case of field-impaired separation, compared to the perpendicular separation, is greater than the advantage of field-assisted separation [37, 41]. This explains why the RE is higher for the morphology F in Fig. 6.2 and the CTE is greater for the morphology G in Fig. 6.2 (see Fig. 6.3 (b,d)(F,G)). Finally we note that the IQE for the copolymer structure F in Fig. 6.2 is higher than for the structure G in Fig. 6.2 (Fig. 6.3 (a) (F,G)). The only reason for this is the difference in the EDE, which amounts to 4.6 %. This discrepancy comes from the fact that in the case of the morphology F in Fig. 6.2 the interfacial area is 1.15 times as large as in the case of the morphology G in Fig. 6.2 (see Fig. 6.4 (a)). As a result, the EDE and IQE in the former case are higher.

6.5.2 $A_3D_{12}A_3$-triblock-copolymer melt

Now, we will consider the symmetric triblock-copolymer system, which has a molecular architecture $A_3D_{12}A_3$. For the parameters given in section 6.4, the bulk structure is a spherical structure [108]. By applying a sufficiently high electric field with strength $\tilde{\alpha} = 1.0$, we observe the deformation and interconnection of the spheres into cylinders as shown in Fig. 6.5 (B). From the graph, we deduce that this structure consists of tilted straight cylinders with regard to the field direction. By comparing this morphology to the corresponding structure B in Fig. 6.2 for the diblock-copolymer system, we deduce that the diblock- and triblock-copolymer systems follow different dynamic of phase transition under the influence of an external electric field. This is because in the initial spherical structure of the triblock-copolymer system the spheres, instead of the disordered arrangement in space as in case of diblock-copolymer system, are highly symmetrically packed and they orient in the same direction as the tilted cylinders. Moreover, it is worth mentioning that the formation of the cylindrical phase in case of the triblock-copolymer system occurs at later simulation time and at higher value of the electric field than in case of the diblock-copolymer system. It is well-established that in triblock-copolymer systems the spherical microdomains can act as physical cross-links [109]. The physical cross-links are responsible for the fact that a higher electric field is required for the triblock-copolymer system compared to the diblock-copolymer case, to orient the cylinders. If the electric field is weak, the system remains in

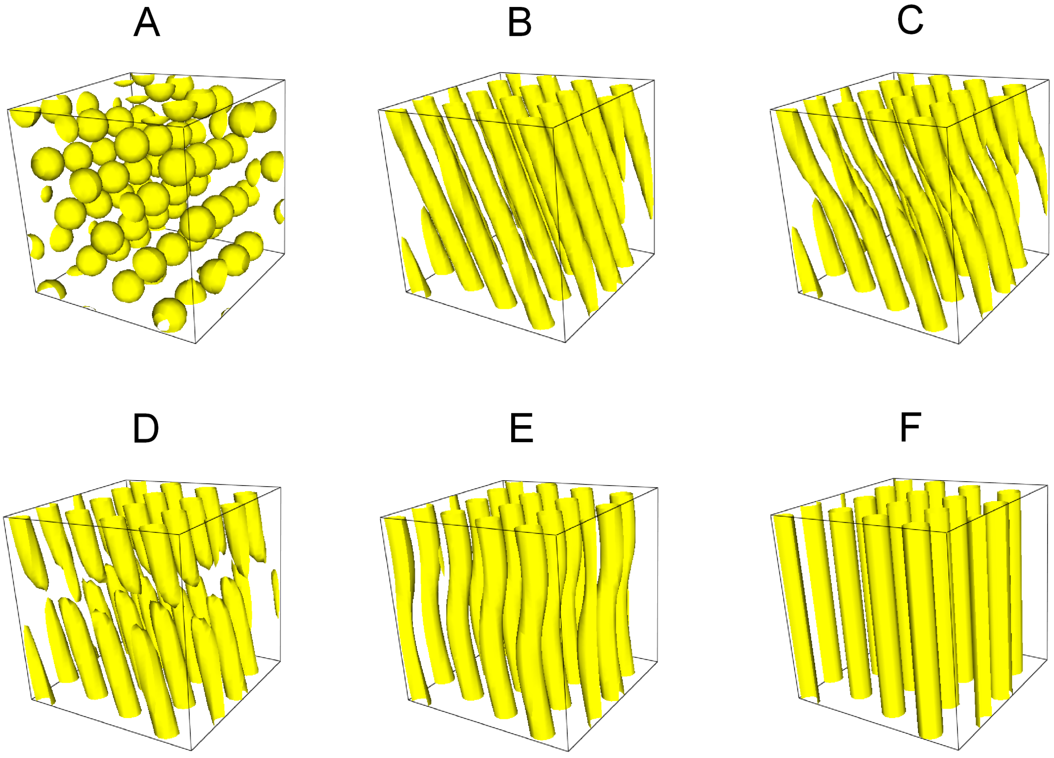

Figure 6.5: Morphologies of $A_3D_{12}A_3$-triblock-copolymer system as a function of time under the influence of an electric field with strength $\tilde{\alpha} = 1.0$. Time t = (A) 0; (B) 240; (C) 270; (D) 280; (E) 290; (F) 320.

the tilted configuration. Such a high-energy configuration has a finite life time, which depends on the electric field strength. It is worth noting that for a stronger field the life time of the high-energy configuration reduces. With increasing simulation time the tilted cylinders become thinner in the middle and finally break, as can be seen by comparing morphologies C and D in Fig. 6.5. In the next stage of the alignment we observe the interconnection of neighboring cylinders with generation of bended cylinders oriented along the electric field lines (see Fig. 6.5 (E)). In the final stage we obtain straight cylinders, which are oriented parallelly to the direction of the applied electric field (see Fig. 6.5 (F)).

After having discussed the morphological changes taking place during the sphere-to-cylinder transition of the triblock-copolymer system, we analyze next the results for the corresponding photovoltaic efficiencies. A first aspect to note is that the interfacial area of the diblock-copolymer structures is lower compared to the triblock-copolymer structures (see Fig. 6.4 (a,b)) [7]. As a result, the average distance the exciton has to travel before reaching the interface is lower in the latter case and leads to a rise in the IQE. The triblock spherical morphology has a higher value of the IQE (2.65 %) than the diblock spherical morphology (1.68 %), due to the fact that the larger interfacial area leads to an increase of the EDE, which in turn results in an increase of the IQE (see Fig. 6.3 and Fig. 6.6).

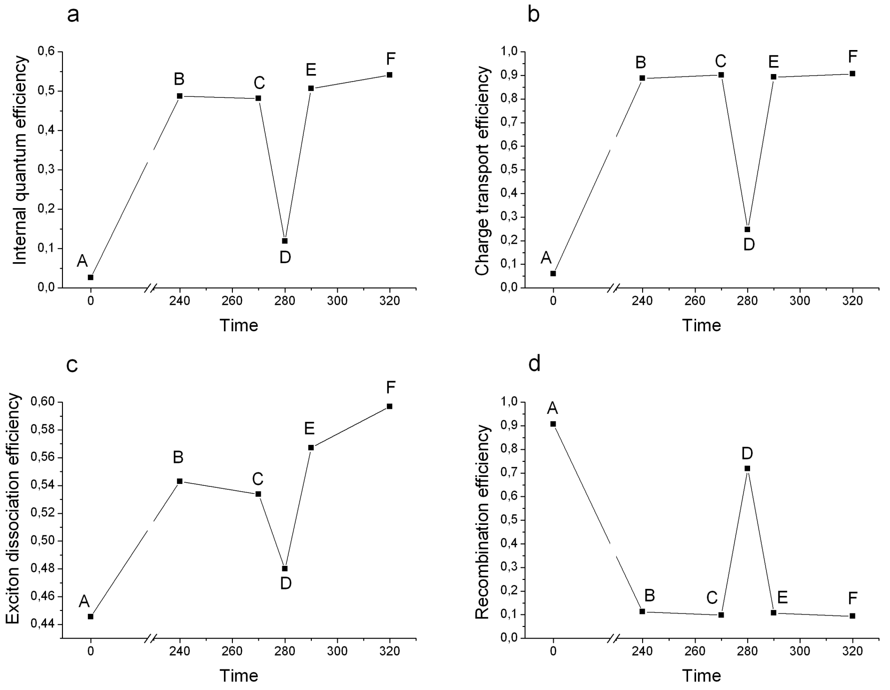

Figure 6.6: Efficiencies of $A_3D_{12}A_3$-triblock-copolymer system as a function of time under the influence of an electric field with strength $\tilde{\alpha} = 1.0$.

Next, from the graph in Figs. 6.6 (a) and 6.6 (b) we deduce that the IQE for the morphologies at times $t = 240$ and $t = 270$ possess almost the same values, even though the CTE in the latter case is higher. To find the cause for this phenomenon, we compare the EDE's for these two cases. From Fig. 6.6 (c), we inferred the reduction in the EDE from time $t = 240$ to time $t = 270$. This correlates with the lowering of the interfacial area for the structure at time $t = 270$ (see Fig. 6.4 (b)), as a result of the thinning of the cylinders in their central part (see morphology C in Fig. 6.5). For the intermediate morphology D in Fig. 6.5, where we have broken cylinders both the CTE and EDE strongly decrease (see Fig. 6.6 (b,c), $t = 280$). The occurrence of broken cylinders leads to the formation of dead-end defects and, hence, to an accumulation of electrons in these defects. As a consequence, a large number of charge losses, due to charge recombination and charge trapping is observed (see Fig. 6.6 (d), $t = 280$). Moreover, the large number of trapped charges leads to a deterioration in exciton dissociation, causing a drop in the EDE (see Fig. 6.6 (c), $t = 280$) [7]. As a result, the nanostructure with broken cylinders possesses a local minimum in the IQE (see Fig. 6.6 (a), $t = 280$). The last two morphologies are similar geometrically to those observed in the diblock situation. In the triblock as well as in diblock case we observed first bended cylinders and then straight cylinders in the last stage of the phase transformation (compare Fig. 6.2 (F,G) with Fig. 6.2 (E,F)). However, in the former case the IQE for the morphology with the bended cylinders is lower compared to the one with the straight cylinders (see Fig. 6.6 (a), $t = 290$, $t = 320$). In this situation both the CTE and EDE are higher for the morphology F with the straight cylinders. The increase in the CTE can be attributed to the same reason as for the diblock-copolymer system, i.e. field-assisted and field-impaired separation. To better understand the increase of the EDE, we analyze next the results in Fig. 6.4 (b). From the graph, we deduce that the bended cylinders are thinner in the middle, resulting in a lower interfacial area and, therefore, lower EDE compared to the straight cylinders. From the triblock-copolymer results, we conclude that the application of a DC-electric field perpendicular to the substrate has a big influence on the photovoltaic performance. By comparing the initial spherical morphology with the subsequent morphologies obtained under the influence of an electric field, we observed a drastic increase in all type of efficiencies, excepting for the structure with the broken cylinders.

To analyze the dependence of the photovoltaic performance of block-copolymer systems on the electric-field magnitude, we consider subsequently in Fig. 6.7 (a) the IQE and EDE as a function of the electric-field strength. By continuously increasing $\tilde{\alpha}$ we observe a steady decrease in the IQE, which can be attributed to the deterioration of the EDE, since the CTE oscillates around an average value of 88 % (see Fig. 6.7 (c)). Moreover, we deduce from Fig. 6.7 (b) that the interfacial area continuously decreases with increasing electric-field strength, which correlates with the decrease of the EDE curve from almost 60 % up to 55 %. To elucidate the reasons for the decrease in the interfacial area, we visualize in Fig. 6.7 (d) the AA-intersegmental spatial correlation function at different values of the electric-field strength together with the spatial distribution of the volume fractions of the A- and D-blocks for the electric-field strength $\tilde{\alpha} = 0.05$

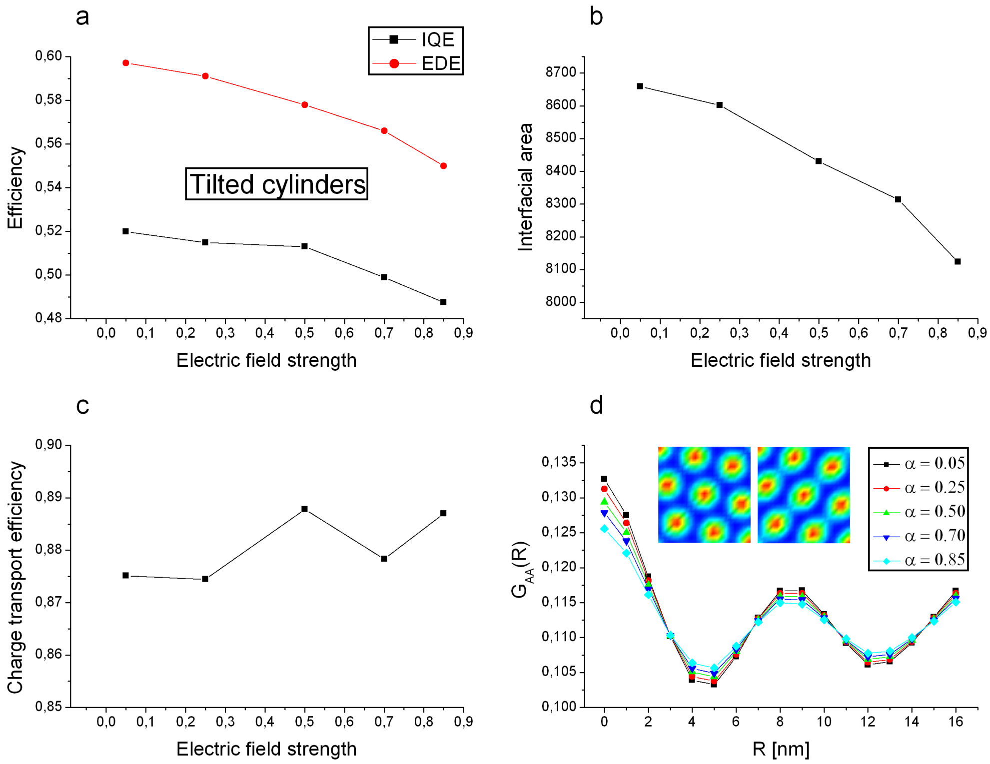

Figure 6.7: (a-c) Efficiencies of the morphology with tilted cylinders of $A_3D_{12}A_3$-triblock-copolymer system as a function of the electric field strength. (d) The spatial correlation functions calculated for different values of an electric field. The left and right sketches are the spatial distribution of the volume fractions of the A- and D-blocks for the electric field strength $\tilde{\alpha} = 0.05$ and $\tilde{\alpha} = 0.85$, respectively.

and $\tilde{\alpha} = 0.85$, respectively. We infer from the spatial correlation functions that the interdomain spacing of $D = 8.5$ nm, defined by the first two maximum, remains constant for all values of the electric-field strength, while the shape and composition of the cylinders are changing. At low electric field strength ($\tilde{\alpha} = 0.05$), we observe the largest amplitude of oscillations of the spatial correlation function. They become smaller for higher values of $\tilde{\alpha}$, due to a higher mixing of the DA-components. Moreover, from the left and right sketches of the morphologies in Fig. 6.7 (d), we conclude that the tilted cylinders become elongated in the diagonal direction and keep an ellipsoid-like form with increasing electric-field strength. This shows that the larger stress on the system causes an increased mixing between A- and D-segments, which in turn leads to the decrease of the interfacial area as a result of the trapping of the A-type segments in the donor phase. We point out that the interfacial area is decreasing, due to connection of the cylinders (see right and left sketches in Fig. 6.7 (d)), providing a lamella-like morphology. This leads to smoothing of the oscillations of the correlation functions.

6.5.3 $A_3D_{12}A_3$-triblock-copolymer systems in the presence of surface interactions

In the previous section we considered only bulk systems. In the following we investigate how the presence of surfaces (electrodes) influence the microstructure formation of block-copolymer-based solar cells and how we can improve their photovoltaic performance by means of electric field post-production treatment. For the calculations we took the triblock-copolymer system with the same parameters as mentioned previously. In these simulations the surface interaction was expressed as an effective interaction parameter $\zeta = (\chi_{AW} - \chi_{DW})$, where χ_{AW} and χ_{DW} represented the interaction energy of A-type segments or D-type segments with the wall, respectively [100]. The surface interaction was defined in such a way, so that a positive value of ζ corresponds to the attraction of D-type segments to the electrodes. We performed runs with a $\chi_{AW} = 0$ and were changing χ_{DW}. First of all, we accomplished dynamic-SCFT calculations

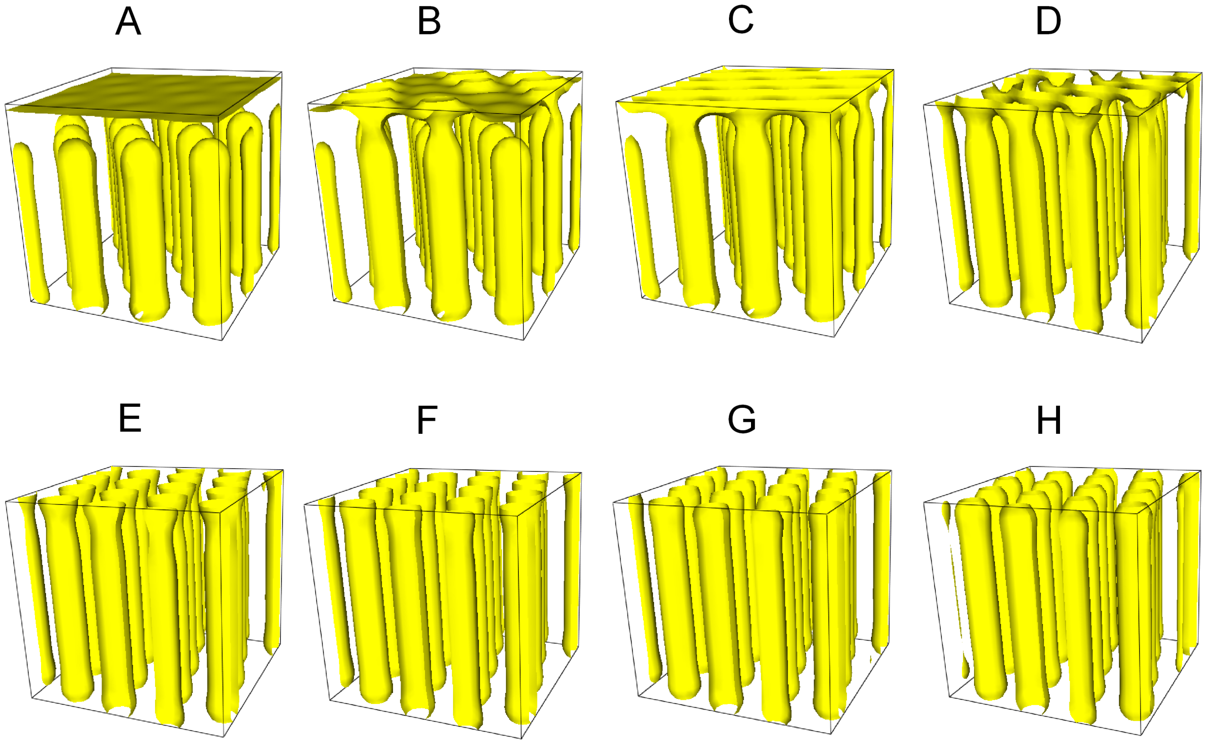

Figure 6.8: Morphologies of a system of $A_3D_{12}A_3$-triblock-copolymers, subjected to an electric-field strength of $\tilde{\alpha} = 0.5$ and a bottom surface interaction of $\zeta_1 = 0.2$, for different top surface interactions $\zeta_2 =$ (A) - 0.0; (B) - 0.01; (C) - 0.03; (D) - 0.05; (E) - 0.08; (F) - 0.12; (G) - 0.16; (H) - 0.2. Surfaces are placed normal to the z-direction of the box. Periodic boundary conditions are applied in x- and y-direction.

with only one bottom electrode possessing a surface interaction of $\zeta_1 = 0.2$. For the top surface, the Neumann boundary condition was used. In Fig. B.1 (a) we show the resulting morphology, in which layers of cylinders orient parallel to the electrodes. These findings concord with the results of Horvat *et al.* [108], who showed that cylinders start to align at the electrode/active layer interface and, then, the alignment propagates from the surface into the center of the active layer. Subsequently, we applied the second electrode on the top of the morphology and let the simulation run up to a time of $t = 3000$ under the electric-field strength $\tilde{\alpha} = 0.5$ for different top surface interactions ζ_2 (see Fig. 6.8 (A-H)). To investigate the effect of the strength of the surface interaction on the structural characteristics of the active layer, we consider the resulting morphologies, visualized in Fig. 6.8. For $\zeta_2 = 0$, we observe the formation of a wetting layer at the top surface (see Fig. 6.8 (B)). This can be explained by the fact that the enrichment of chain ends and depletion of middle segments near to the surfaces favor parallel morphologies, where chains orient mainly perpendicular to the surfaces. This effect results in an entropic attraction of the shorter A-type blocks to the neutral surface and was investigated by Meng *et al.* [110]. Moreover, by increasing the surface interaction parameter from $\zeta_2 = 0.01$ to $\zeta_2 = 0.2$, we observe a gradual enrichment of the top surface with the D-type blocks (see Fig. 6.8 (B-H)). This results in a cylindrical connection of the A-type phase to the electrode, as shown for the morphologies from E to H in Fig. 6.8, providing ideally segregated vertical cylinders with continuous pathways to the electrodes.

Next, we study the influence of the top surface interaction under a constant electric field on the photovoltaic performance. In Fig. 6.9 we consider the results for the IQE, EDE, CTE and RE as a function of the surface interaction, obtained from the DMC-SCFT simulations. In case of the morphology A in Fig. 6.8 with $\zeta_2 = 0$, we note that the cylinders do not have any connections to the upper electrode. This causes that a huge number of electrons are accumulated in the dead-end-type of defects, leading to a very high number of electron-hole recombinations (see Fig. 6.9 (a)). As a result of these charge losses, the CTE is very low. Similar observations can be made for morphology B with $\zeta_2 = 0.01$. However, in this case we observe the formation of some isolated contacts to the surface, resulting in a slightly higher CTE. Moreover, from Fig. 6.9 (a) we deduce that the EDE in both cases possesses almost the same values. This leads to the IQE's, shown in Fig. 6.9 (a), which follow the CTE dependence, but they are leveled down by the EDE. By further increasing the surface interaction parameter up to $\zeta_2 = 0.08$, we observe a growth in the CTE, due to an improved connection of the cylinders to the top surface. The maximum IQE at surface interaction of $\zeta_2 = 0.12$ is cased by further increase of the EDE up to the same strength of the surface interaction. As shown by Arias *et al.* [92], the external quantum efficiency (EQE) of a device fabricated with surface modification can be ten times higher compared to the one of a device fabricated without surface modification. Moreover, Arias *et al.* [92] and Quiles *et al.* [93] suggested that the increase in the EQE as well as in the device power conversion efficiency is a result of an optimized charge transport

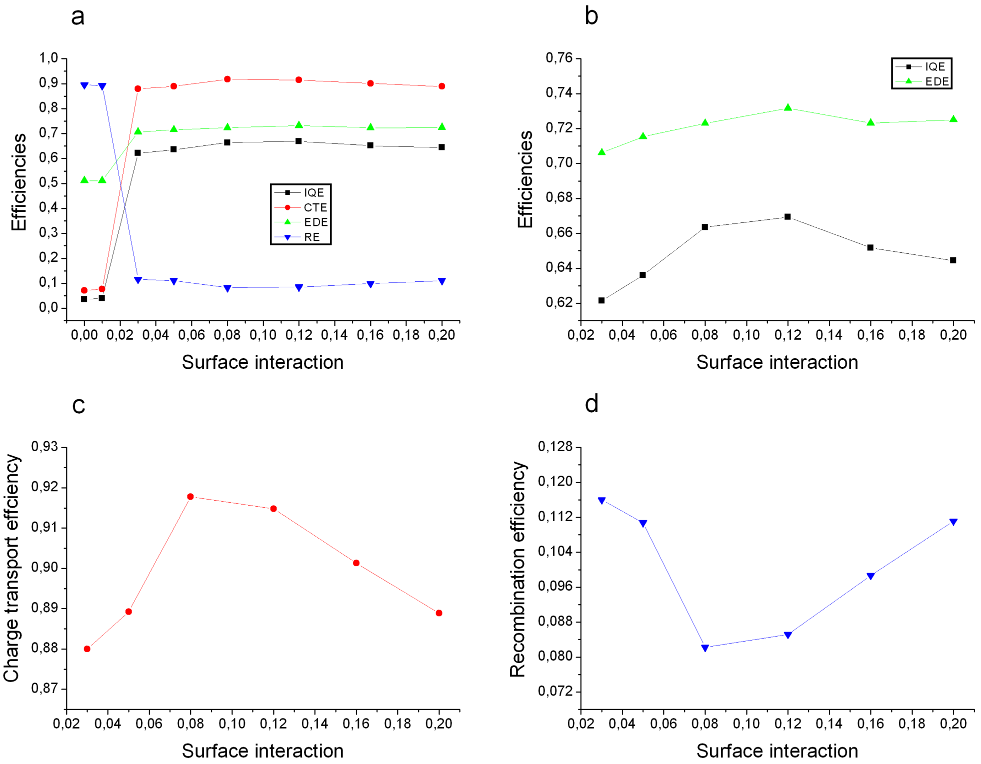

Figure 6.9: Efficiencies of a system of $A_3D_{12}A_3$-triblock-copolymers in the presence of a bottom electrode with surface interaction of $\zeta_1 = 0.2$ and electric-field strength of $\tilde{\alpha} = 0.5$ as a function of the surface interaction of the top electrode. IQE - internal quantum efficiency, CTE - charge transport efficiency, EDE - exciton dissociation efficiency, RE - recombination efficiency. For a better visualization, we show (b) IQE and EDE, (c) CTE and (d) RE in the range of surface interactions from $\zeta_2 = 0.03$ up to $\zeta_2 = 0.2$.

in vertically segregated nanodevices. This concord well with the CTE of the morphology for a surface interaction of $\zeta_2 \geq 0.03$, which is about ten times higher in comparison to the untreated one with $\zeta_2 = 0$ (see morphology A in Fig. 6.8).

In addition, after comparing morphologies E and F in Fig. 6.8, we see that the CTE is higher in the former case because of the lower RE (see Fig. 6.9, $\zeta_2 = 0.08$ and $\zeta_2 = 0.12$). This is due to the fact that for the morphology E in Fig. 6.8 the amount of the A-phase, directly contacting the top electrode, is higher compared to the morphology F. This results in a larger interface from which electrons can be extracted. In all other cases the reduction in the electron extraction area leads to a higher probability that the opposite charges can meet each other and recombine. However, we point out that a high CTE is not a sufficient requirement for the morphology E to become the most efficient of all morphologies. In our calculations the maximum of the IQE is observed for the structure with $\zeta_2 = 0.12$, where the lower CTE in comparison to the structure with $\zeta_2 = 0.08$ is compensated by the higher EDE. At higher ζ_2 the reduced contact area of the A-phase to the top electrode leads to a decrease of the CTE, while the EDE undergoes only a small change (see Fig. 6.9 (b,c)). As a consequence, we see that in this regime the IQE decreases mainly due to the decrease of the CTE.

6.6 Influence of impurities on the photovoltaic efficiency

As was mentioned previously, impurities from the Al cathode and ITO anode can diffuse through the entire active layer [86]. In the following we show how the diffusion of impurities from electrode materials can contribute to the degradation of the device performance. In Fig. 6.10 we show calculation results for the IQE and corresponding morphologies of a system of A_5D_{15}-diblock-copolymers with different number of particle impurities as a function of particle size. We see that without any particle impurity inside the morphology the structure with the straight cylinders is obtained. If we introduce at least one particle impurity into the system, we

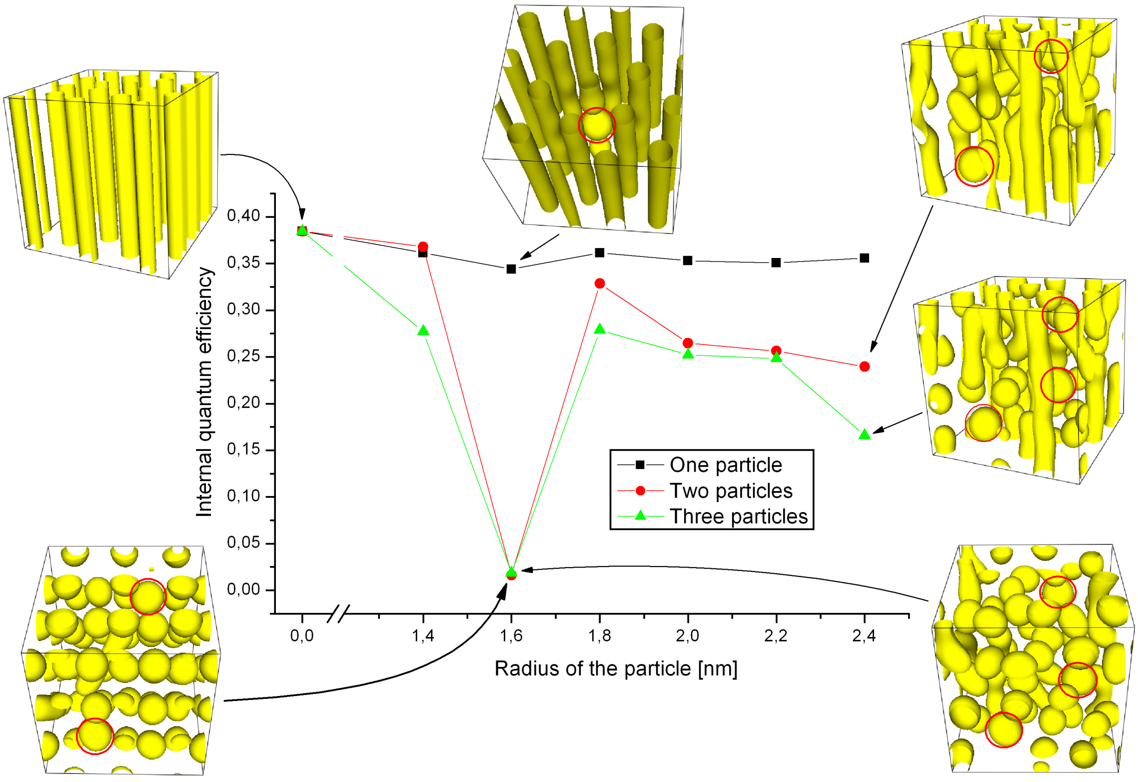

Figure 6.10: IQE and corresponding morphologies of a system of A_5D_{15}-diblock-copolymers with different number of particle impurities as a function of particle size. Number of particles embedded into the system is one (black squares), two (red circles) or three (green triangles). Red circles on the morphologies define the position of impurity particles.

observe a sever density perturbation in its surrounding. We conclude from this observation that the particles can have a very strong effect on the copolymer morphology caused by the entropic attraction of the shorter A-type blocks to the neutral hard walls of the particle impurities. Moreover, we see that the particle impurities are covered by the shorter A-type blocks of polymer chains. The effective size of these covered particles (D_A) is comparable with the size of the domain spacing $D \approx 12.5$ nm (see the $G_{AA}(R)$ spatial correlation function reported in Fig. 6.4 (c)). The largest effect is observed for the morphologies with two and three particle impurities with a particle radius of $r = 1.6$ nm, where we observe a cylinder-to-sphere phase transition. In this cases we find a major drop in the IQE, as demonstrated in Fig. 6.10. It is worth mentioning in this context that, using transmission electron microscopy (TEM), Lo *et al.* [111] determined, that the occurrence of order-order and order-disorder transitions strongly depend on the relative size between particle diameter and domain spacing. In our calculations with $D_A/D \sim 1$ we obtained almost complete transformation of the straight cylinders into spheres, which can be associated with a loss of conformational entropy due to the stretching of the polymer chains [111]. This behavior has a major impact on the photovoltaic performance, as can be concluded from

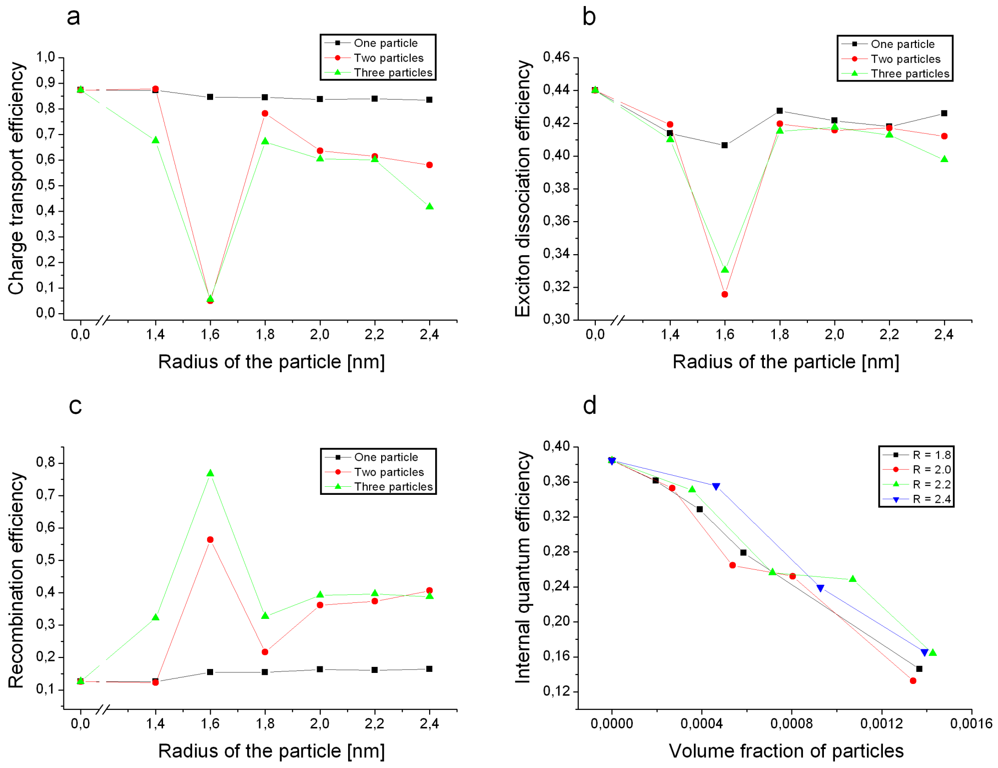

Figure 6.11: (a-c) Efficiencies of a system of A_5D_{15}-diblock-copolymers with different number of particle impurities as a function of particle size. (d) Internal quantum efficiency as a function of volume fraction of particle impurities.

Fig. 6.11 (a-c), where we show the results for the CTE, EDE and RE as a function of particle size. From these graphs we deduce that the IQE for the structures with two and three particles with a radius $r = 1.6$, exhibit a minimum, as a result of the charge losses caused by electron-hole recombinations and electron trapping in the defects. This leads to a substantial deterioration in the EDE as well as CTE. We point out that the perturbation of only one particle impurity for the whole range of particle radii is not strong enough for causing a substantial disorder of the block-copolymer morphology and, as a consequence, the IQE undergoes only minor changes (see Fig. 6.10). However, by introducing two or three impurity particles with radii in the range 1.8 - 2.4, we observe a significant change in the CTE and in the RE. By contrast, the EDE oscillates around a value of 42 % (see Fig. 6.11 (a,c)). Moreover, from Fig. 6.10, we deduce that increasing the number and size of the impurity particles leads to a stronger destruction of the nanostructure with a fewer number of continuous percolation pathways to the electrodes. This induces an increase of the number of recombinations, causing a deterioration of the CTE. These observations agree well with the experimental results obtained by Leong *et al.* [112]. They showed that the impurity particles can lead to an increase in charge carrier recombinations and affect the nanomorphology, significantly reducing the performance of the bulk heterojunction solar cells.

Finally, in Fig. 6.11 (d) we plot the dependence of the IQE on the volume fraction of the particles. Through increasing the loading of the particles, the interfacial curvature between the A- and D-domains are changing, as shown through the morphologies in Fig. 6.10, which leads to strong density fluctuations in the vicinity of the impurities, resulting in the cylinder-to-sphere transition. This causes a degradation of percolation paths to the electrodes and, as a consequence, leads to a gradual decrease in the IQE with increasing volume fraction of the impurities (see Fig. 6.11 (d)).

Chapter 7

Influence of chemical details on photovoltaic performance

7.1 Introduction

In contrast to inorganic semiconductors, in excitonic photovoltaics D/A interface plays a critical role for photogeneration of charges and efficient device performance [113]. To enhance the power conversion efficiency of PSC devices, it is necessary to control the active layer of the morphology on the nanoscale [114]. It has been shown on PFB/F8BT blend devices by both experimental and computational studies that the major part of the charge generation and charge transport takes place at the domain centers of the nanoscale morphology, due to mixing of D- and A-segments [115, 130, 131]. Another important factor limiting photovoltaic performance and long-term stability of the devices is the process of photooxidation. The photodegradation results in the formation of unwanted trap sites with systematic deterioration of the charge carrier transport to the respective electrodes. These studies demonstrate that the chemical composition of the domains and chemical details of the monomers can play crucial role in the photovoltaic performance of solar-cell nanodevices.

In this chapter we investigate the effect of mixing of the D- and A-components on the exciton dissociation and charge transport, which have a decisive impact on the performance of OPV cells. To this end, we have extended our conventional DMC-SCFT approach by parameterizing the processes associated with exciton dissociation as well as the processes associated with electron and hole transport depending on the composition of the photoactive layer. Our goal is to introduce these effects to enabling large-system size calculations at low computational costs, which will be demonstrated in chapter 8. To validate our parameterize algorithm, we present a full comparison between conventional field-based, parameterized field-based and particle-based approaches. In addition, to evaluate the influence of chemical defects, such as keto-defects, on the efficiency of PSC, we performed the parameterized field-based calculations by taking into account the effect of photooxidation of the F8BT monomers.

7.2 Parameterized field-based approach and simulation parameters

In the following we introduce the parameterized version of the field-based algorithm and compare corresponding results to the ones obtained by conventional field-based as well as by particle-based approaches. We consider the system composed of DA-homopolymer blend, where the D-polymer and A-polymer consist of PFB and F8BT, respectively. As already mentioned in section 4.3.3, the conventional field-based approach is based on combining the SCFT, to generate the morphologies, with a first reaction(FR)-type DMC method, to simulate the elementary photovoltaic processes involving the charge carriers and excitons within the particle description

[7, 69]. The excitons were created uniformly at random locations with a constant rate $\omega_{cre} = 100$ $\mathrm{s}^{-1}\mathrm{nm}^{-2}$, which has been determined from AM 1.5 solar spectrum with an illumination of 90 $\mathrm{mW/cm}^2$ and the absorption spectrum of the polymer material [121]. After creation, the excitons may diffuse, dissociate or recombine. To describe the exciton diffusion within the active layer we used the model, introduced in section 3.3.2. The exciton hopping rate from site i to a nearby site j has been calculated using the formula in Eq. (3.9). The transition energy ΔE_{ij} is determined from a Gaussian distributed density of states (DOS) of width $\sigma = 0.062$ eV. The prefactor $\omega_e r_0^6$ $= 0.3$ $\mathrm{nm}^6\mathrm{ps}^{-1}$ as well as exciton recombination rate $\omega_{dec} = 0.002$ ps^{-1} were chosen such that the excitons have a lifetime of $\sim$ 500 ps and an overall diffusion length of $\sim$ 5 nm, which is in agreement with experimental measurements [116]. In the conventional unparameterized field-based model the excitons may dissociate, as soon as they meet a sharp D/A interface, forming an electron/hole pair with a rate $\omega_{exs} = 10$ ps^{-1}, which is the inverse of the exciton dissociation time of about 100 fs [41]. We note, that in this approach the introduction of a sharp D/A interface is necessary, since the average density description of the segment distribution does not permit the explicit assignment of the D- or A-properties to the polymer chains. To this end, we assumed that the majority component at each lattice site determines whether the site is either part of the electron-conducting or hole-conducting phase. This approximation leads to the neglecting of large regions of mixing between D- and A-type polymer chains, where the major part of exciton dissociation processes occur [115]. By contrast, in the parameterized version of the field-based algorithm, the excitons are able to dissociate into free charges at any place within the active layer, due to the D/A contacts dispersed throughout the bulk, increasing the interfacial region [117]. To estimate and introduce these exciton dissociation rates into our calculations we used the functional dependence of the average frequencies of exciton dissociation as a function of the volume fraction of the donor material (ϕ_D), obtained from the particle-based approach [115]. At $\phi_A = \phi_D = 0.5$, the maximum exciton dissociation rate is defined as ω_{exs}. For all other values of volume fractions ω_{exs} is leveled down using the functional dependence previously mentioned.

Once the electron/hole pair is separated, the charge carriers may hop from site to site. To calculate the rate of hopping of electrons and holes between nearest-neighbor lattice sites, we used the formula from the Marcus-Hush formalism [118, 119]:

$$\omega_{ij} = V_{ij} \exp\left[-\frac{(\Delta E_{ij} + \lambda)^2}{4\lambda k_B T}\right], \tag{7.1}$$

where ΔE_{ij} denotes the difference between the energies of hopping sites j and i, whereas k_B is Boltzmann's constant and $\lambda = 0.25$ eV is the reorganization energy. The prefactor V_{ij} is the coupling parameter and one of the key quantities that determines the efficiency of the charge hopping. As was demonstrated in section 4.3.2, under the assumption of an iso-energetic material, the coupling parameter $V_{ij} = V_{hop}$ can be estimated using Eq. (4.14), where $\mu_{e/h} =$

10^{-8} $\mathrm{m^2V^{-1}s^{-1}}$ defines the mobility of the charges in both polymer species and is taken to be equal for both electrons and holes, whereas $a_0 = 1$ nm is the lattice constant. In addition, we ensured that the recombination may take place with the rate $\omega_{rec} = 10^{-6}$ $\mathrm{ps^{-1}}$, if an electron and a hole are located on adjacent sites.

To introduce the effect of mixing on the charge transport in the parameterized version of the field-based approach, we used the particle-based approach, in which the coupling parameter between the sites i and j was determined as follows [115, 122, 123, 124]:

$$V_{ij} = \frac{|J_{ij}|^2}{\hbar}\sqrt{\frac{\pi}{\lambda_{ij}k_B T}}, \tag{7.2}$$

where J_{ij} is a transfer integral for electron or hole transfer. To calculate the charge transfer integrals within the framework of the particle-based simulation, we used following procedure. First of all the equilibrium mesoscopic morphology was transformed into a coarse-grained (CG) representation by using the density-biased Monte-Carlo method [109] and then, to increase the system resolution to a full-atomistic description, we used the CG to fine-grained mapping technique [125]. Next, to evaluate the coupling parameter J_{ij} as a function of the mutual orientation of the monomers, we used the dimer-projection method of Valeev *et al.* [126], which relies on the concept of projecting molecular orbitals of monomers onto the manifold of the molecular orbitals of the dimer within a counterpoise basis set [125, 126, 127]. To this end, the transfer integrals were calculated using the particle-based simulations and averaged over all sampled configurations for different volume fractions of the D- or A-component. The values for the transfer integrals were then included in Eq. (7.2) to determine the coupling parameter V_{ij} and finally in Eq. (7.1) to calculate the charge transfer rates.

For the purpose of parameterization of the exciton dissociation rates as well as charge transfer rates for both electrons and holes, we used following functional dependencies represented in Fig. 7.1 (a-c), obtained from the particle-based simulations, where the interfacial mixing is taken into account by distinguishing between the D or A monomer types [115].

The charge current density at position $\mathbf{r}$ and time t was calculated through [115]:

$$\mathbf{J}(\mathbf{r},t) = \rho(\mathbf{r},t)\mathbf{v}_d(\mathbf{r},t), \tag{7.3}$$

where $\mathbf{v}_d(\mathbf{r},t)$ is the average drift velocity of the charges and $\rho(\mathbf{r},t) = q \cdot n(\mathbf{r},t)$ is the charge density with q as the charge and $n(\mathbf{r},t)$ as the number density.

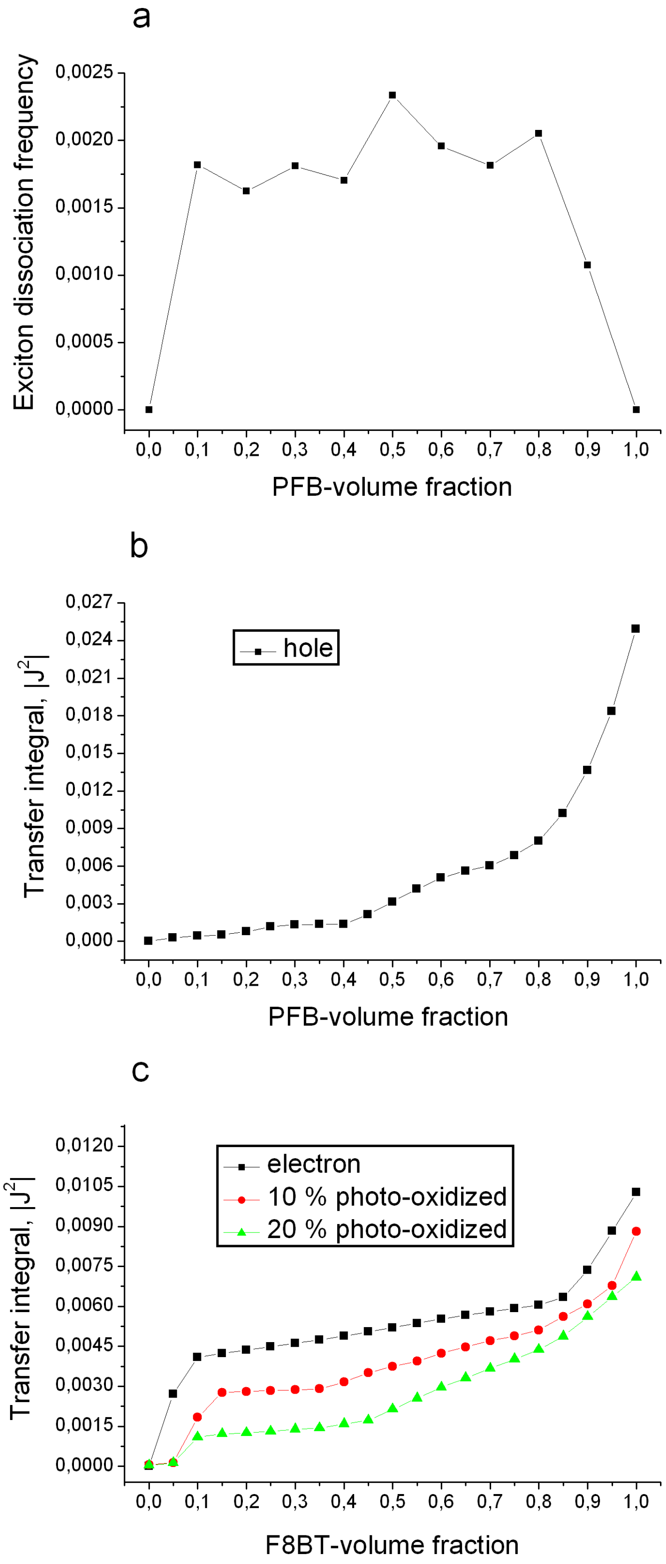

Figure 7.1: The functional dependencies of the (a) averaged exciton dissociation frequency and (b) hole transfer integral as a function of PFB-volume fraction as well as (c) electron transfer integrals as a function of F8BT-volume fraction.

In the conventional and parameterized field-based simulations we considered a system composed of ITO|PFB-F8BT|Al, where ITO and Al represent the materials of the hole- and electron-extracting electrodes, respectively. The standard deviation for the Gaussian density-of-states was chosen as $\sigma = 0.062$ eV. Moreover the Coulomb potential was cutted at $r_c = 10$ nm, whereas the difference in work functions of the electrodes was taken as $\Delta\phi_w = 0.5$ V and the relative permittivity as $\varepsilon_r = 3.5$ [7, 32]. All the simulations were run up to 100000 generated excitons. Moreover, we considered the system to be equilibrated, when the deviations in the values of the exciton dissociation efficiency, charge transport efficiency and exciton lifetime did not exceed the preset error of 0.01 % within a certain time span in the production phase of the simulation.

To generate the equilibrium lamellar morphology, we carried out static-SCFT calculation with the parameters taken from ref. [115]. For the calculation, we took a Flory-Huggins interaction parameter of $\chi_{AD} = 0.337$ and a polymer segment fraction of the A-blocks of $f_A = 0.5$, whereas the statistical segment length was taken as $b_A = b_D = b$ (that is taken to be unity). The simulation box was constituted of $11 \times 11 \times 11$ grid points with a spatial mesh width of $\Delta x = \Delta y = \Delta z = 1.0$ in units of the statistical segment length b. The periodic boundary conditions were applied along the x- , y- and z-direction. The contour-step size along the chain was chosen as $\Delta s = 0.1$ and the relative accuracy for the computed free energy as 10^{-5}. Afterwards, we applied parameterized DMC algorithm on the morphology in the field-based representation, obtained from the static-SCFT simulation.

7.3 Application to lamellar-like $D_{10}A_{10}$-homopolymer blend

7.3.1 Influence of intermixing of the D- and A-components on the device efficiency

To validate the parameterized field-based algorithm, we compare in the following the parameterized version of the field-based, conventional field-based and particle-based approaches. We begin our analysis by considering a lamellar-like blend of $D_{10}A_{10}$-homopolymers of PFB and F8BT. In Fig. 7.2 we show the resulting morphology, obtained with the static-SCFT calculation. The yellow-green region corresponds to the interface, where there is a large degree of mixing between D- and A-segments.

In table 7.1 we have reported the values of the exciton dissociation efficiencies (EDE) for the three different methods mentioned previously. By comparing the conventional field-based to atomistic calculation, we observe a pronounced discrepancy in the EDE. We notice that the conventional field-based approach provides a significantly smaller EDE than the atomistic approach, which differ by about 41 %. This results from the fact that in the atomistic approach a broad region of intermixing of the PFB- and F8BT-monomers are taken into account, enabling

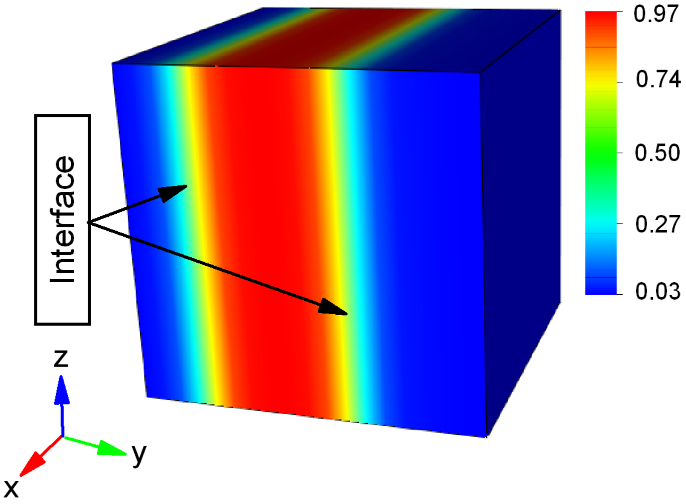

Figure 7.2: Morphology of $D_{10}A_{10}$-homopolymer blend obtained with a static-SCFT calculation [red: majority of A phase (electron-conducting); blue: majority of D phase (hole-conducting)].

exciton generation away from the interface resulting in an increased dissociation efficiency into free charges. Moreover, we deduce from table 7.1 that the value of the EDE, obtained with parameterized field-based simulation is almost 30 % greater than the one observed for the conventional simulation. As we already mentioned above, in the conventional field-based method we have a sharp D/A interface due to the assumption that the majority component determines whether the site is either part of the acceptor or donor phase. In contrast to this, in the parameterized field-based method the interface plays important role, as a result of the fact that in this region a major part of the exciton dissociation processes take place. Moreover, we note that the EDE in case of parameterized simulation differ only about 12 % in comparison to the atomistic simulation. This relates to the fact that in the atomistic approach the intermixing between PFB- and F8BT-monomers was treated explicitly, resulting in a larger number of contacts between them, increasing the exciton dissociation.

Next, we analyze the effect of mixing between D- and A-components on the charge transport efficiency (CTE). From table 7.1, we deduce that there are noticeable difference between the atomistic and field-based algorithms. The atomistic approach provides a reduction of the CTE of 30 % with regard to the conventional field-based approach, which has a CTE of 100 %. This can be explained by the fact that in the atomistic case the electrons (holes) generated in the F8BT (PFB) inclusions in the bulk of the PFB-rich (F8BT-rich) phase do not have direct percolation pathways to the respective electrodes, and are getting trapped [128]. This results in a large number of trap-limited recombinations and, ultimately, in a decreased collection of charge carriers at the electrodes. Similar behavior has been observed experimentally by Marohn *et al.* [129] on bulk heterojunction solar-cell films composed of PFB/F8BT polymer blend,

Method	EDE (%)	CTE (%)	IQE (%)
Conventional field	21.0	100.0	21.0
Parameterized field	50.2	82.5	41.4
Atomistic	61.9	70.0	43.3

Table 7.1: Exciton dissociation efficiency (EDE), charge transport efficiency (CTE), internal quantum efficiency (IQE), calculated either with the conventional field-based, parameterized field-based or atomistic approach.

using photopotential-fluctuation spectroscopy. They inferred from their investigations that the intermixing of phases leads to charge trapping and, thereby, to a decreased efficiency of the solar cell device.

Moreover, we see that in case of parameterized field-based approach we have obtained an intermediate value for the CTE, which is 12.5 % greater than the one observed for the atomistic simulation and 17.5 % lower than the one of the conventional simulation (see table 7.1). The difference of 12.5 % compared to the atomistic approach comes from the neglect of intermixing of the PFB- and F8BT-monomers and, hence, from the absence of charge-trapping sites in isolated inclusions of the minority component. This has been confirmed by Brenner *et al.* [131], who demonstrated that the intermixing between PFB- and F8BT-phases results in efficient geminate recombination and, thus, in a deteriorated charge carrier transport to the electrodes. However, it is worth mentioning that parameterization ensures a better agreement between approximate and exact treatment of the PFB/F8BT polymer blend by taking into account the effect of mixing of the D- and A-components. Moreover, we point out that in the parameterized simulation the reduction of the CTE of 17.5 % with regard to conventional approach is mainly due to the electron-hole recombinations, which are caused by the poor transfer properties of the electrons or holes in the D- or A-phase, respectively.

In the third column of table 7.1, we show the values for the internal quantum efficiency (IQE) for the different approaches. By comparing conventional and atomistic approaches we see that the IQE increases more than two times, from 21 % to 43.3 %. By contrast, the parameterized version of field-based approach provides a value of the IQE of 41.4 %, which is in good agreement with the atomistic approach. This can be explained by the lower EDE, which is compensated by the higher CTE.

7.3.2 Comparison of current densities

To further investigate the effect of parameterization on the CTE, we analyze next the electron- and hole-current densities as well as the corresponding volume fractions of the PFB-and F8BT-monomers along the y-coordinate of the box, calculated either with the conventional or parameterized field-based approach. In Fig. 7.3 (a,b) we see that for the conventional simulation the main part of the electron and hole transport take place near to the D/A interfaces. This is due to the electrostatic attraction between adjacent electrons and holes at the D/A interfaces and the neglect of intermixing of the D- and A-type of monomers [115]. In this case the charge flow is not slowed down by the intermixing of the components and this ensures an efficient collection of the charges at the electrodes. Although the parameterized field-based approach also neglects the explicit representation of the PFB- and F8BT-polymer chains, we observe that the photocurrent is preferentially generated within each polymer phase, as can be seen in Fig. 7.3 (c,d). Moreover, the electron and hole current densities are shifted to the centers of the F8BT-rich and PFB-rich domains, respectively. This can be explained by the concentration gradient, which pushes the charges toward the domain centers. This observation is consistent

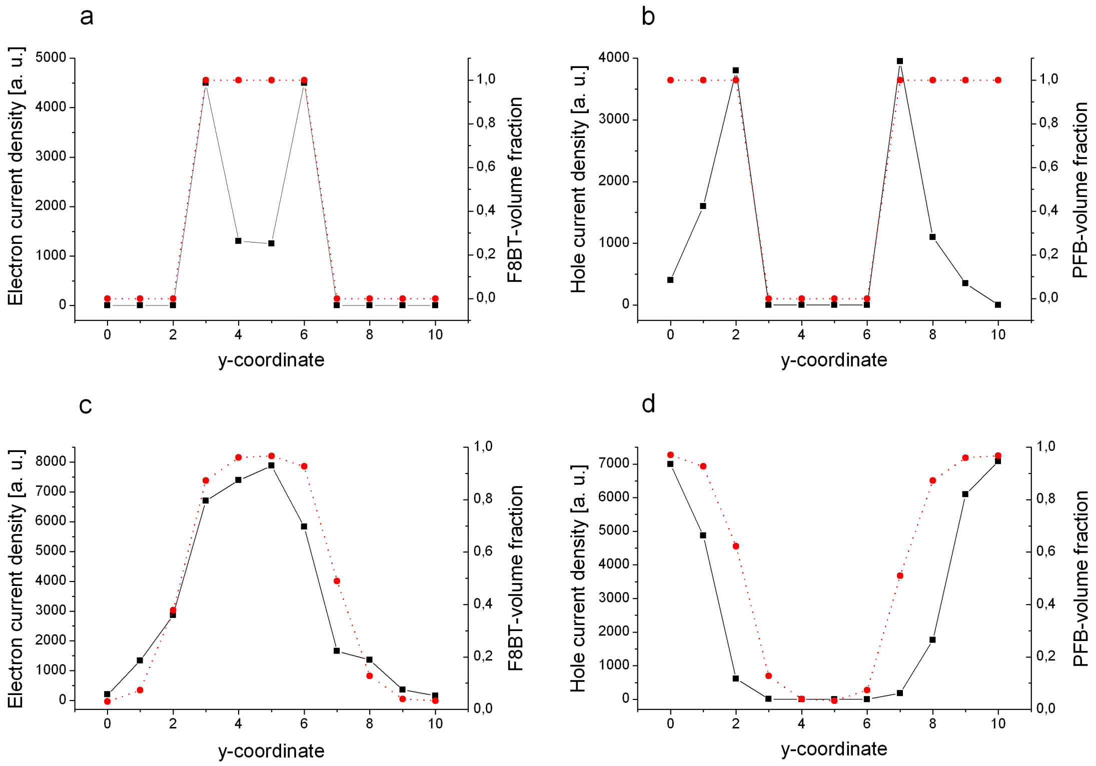

Figure 7.3: (a,c) Electron-current density (solid black line) or (b,d) hole-current density (solid black line) in conjuction with (a,c) PFB- (red dashed line) or (b,d) F8BT- (red dashed line) volume fraction as a function of the y-coordinate of the simulation box, obtained using either conventional or parameterized field-based approach. The (a) and (b) graphs correspond to the conventional field-based approach, whereas the (c) and (d) graphs to the parameterized field-based approach.

with the photocurrent microscopy measurements made by McNeill *et al.* [130] and Brenner *et al.* [131] on PFB/F8BT blend devices. In these works they showed that the current is generated within the bulk and not at the D/A interfaces. In addition, Coffey and Ginger [132], when they studied the PFB/F8BT blends using time-resolved electrostatic force microscopy, observed a slower charging near to the microscale domain boundaries and that the bulk of the photocurrent is generated in regions away from the interfaces in the domain centers. Moreover, we notice that similar conclusion were drawn by us from our atomistic simulations, where the main part of the photocurrent was pushed toward the centers of the phases, where the higher number of possible percolation paths, due to the low concentration of minority components, enables a fast relief of the charges toward the electrodes [115].

7.3.3 The effect of photo-oxidation on photovoltaic performance

To conclude this chapter, we investigate the effect of photo-oxidation of the fluorene moiety on the photovoltaic performance of the PSC. The performance of PSCs is strongly dependent on the nanoscale morphology. In particular, it has been demonstrated by Noh *et al.* [133], that UV irradiation of polyfluorenes leads to the formation of keto-defects, and, thus, to the photodegradation of semiconducting polymers. The formation of keto-defects was proved by the change of photoluminescent and Fourier transfer infrared spectra, where they observed the formation of the carbonyl-stretching peak at 1721 cm^{-1} [133]. The electron-trapping fluorenone defects can reduce charge-carrier mobility with subsequent increase of recombination losses, which leads to a decreased performance of the PSC.

To parameterize the exciton dissociation rates as well as charge transfer rates for both electrons and holes, we used the functional dependencies depicted in Fig. 7.1 (a-c), obtained from the particle-based simulations [115]. In Fig. 7.4, we have plotted the charge transport efficiencies as a function of the fraction of photo-oxidized F8BT monomers for both particle-based (atomistic) and parameterized field-based (mesoscopic) representations. The change in the fraction of photo-oxidized monomers can be associated with the dose of radiation, which leads to the formation of fluorenone defects, obtained upon the exposure of the device to the sun light. As expected, the efficiencies in both cases decrease rapidly with increasing concentration of the keto-defects. In case of the atomistic calculations, the ratio of inter-molecular to intra-molecular hops also decreases rapidly with increasing concentration of fluorenone defects, as demonstrated by us in Ref. [115]. This work revealed that, due to the keto-defects, electron transport becomes localized on the same polymer chain. This localization leads to a so-called keto-induced charge-trapping on the polymer chain, resulting in an increased number of charge losses through increased number of accumulations and recombinations [115]. Therefore, since in mesoscopic field-based calculations we used functional dependencies obtained from the particle-based simu-

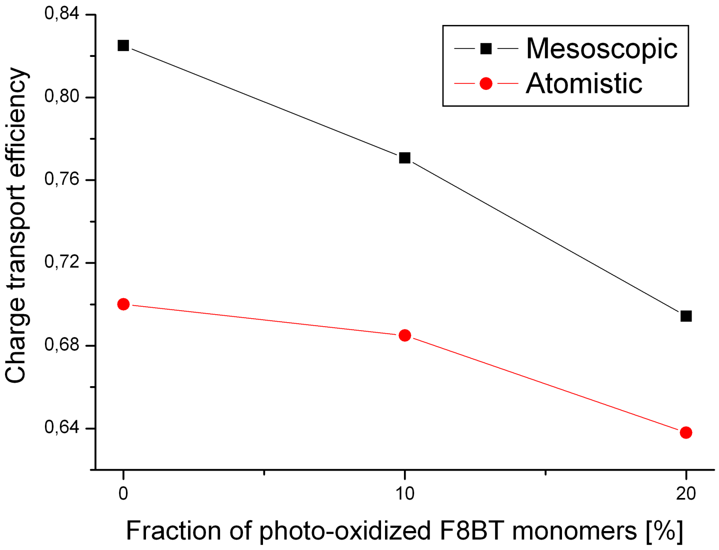

Figure 7.4: Charge transport efficiency as a function of the fraction of photo-oxidized F8BT monomers for both particle-based (atomistic) and parameterized field-based (mesoscopic) calculations.

lations, this effect is taken into account. This correlates with the decrease of the electron transfer rates of the mesoscopic calculations with increasing fraction of photo-oxidized F8BT monomers, shown in Fig. 7.1 (c). Moreover, the lowering of the electron transfer rates affect not only the electrons but also the holes in close proximity. The overall time that the electrons stay in the system before their are extracted become much higher than for the holes. In turn, this facilitates the increase of the electron concentration and, hence, gives rise to the number of recombinations between electrons and holes. As a result, this leads to a deterioration of the charge transport efficiency and, ultimately, to a lower overall device performance. These results are in agreement with the experimental study of Reid *et al.* [76], who showed through time-resolved electrostatic force microscopy that the overall device efficiency of PFB-F8BT blends decreases rapidly with increasing photooxidation. In addition, the theoretical study presented here shows that the photodegradation processes strongly reduce the long-term stability of PSCs and consequently prevents their commercial use.

Chapter 8

Full device calculations of polymer-based solar cells

8.1 Introduction

The absorption spectrum of a full photoactive device differs from the absorption spectrum of its individual morphologies in the active layer. When it is illuminated, there will be a change in refractive index at each particular interface of the semitransparent electrode and bulk heterojunction, which causes that a fraction of the light will be transmitted and the other will be reflected. Moreover, the back electrode also absorbs and reflects some portion of the light [37]. These processes affect the distribution of the optical electric field inside the device. The distribution of exciton creations within the photoactive layer, i.e. the optical absorption distribution, is directly dependent on the distribution of the optical-electric-field energy dissipation [136]. In order to gain a better understanding of the exciton- and charge-loss processes limiting the device efficiency of PSCs, the absorption profile within the photoactive layer of the device is of fundamental interest for further device optimization [134]. In this work the optical interference effects are modeled, using the transfer-matrix method, introduced in section 4.4. The optical modeling will permit to determine the regions of low and high absorption intensity within the heterojunction and to study their effect on exciton- and charge-loss processes of the full nanodevice [37]. Kimber *et al.* [37] have recently demonstrated that full optical modeling in combination with the transfer-matrix method can be a useful approach by including the optical absorption profiles of a bilayer photovoltaic device into their kinetic Monte Carlo model. They obtained calculation results in excellent agreement with the experimental values for the external quantum efficiency (EQE) and the current density. In another work, Yan *et al.* [116] used the transfer-matrix method, to determine the exciton generation profiles of a bilayer structure and introduce them into the Monte Carlo simulations, to investigate the influence of structural disorder at the D/A interface and the decrease in electron and hole mobilities with annealing. Bavel *et al.* showed through transmission electron microscopy measurements on thermally annealed P3HT/PCBM films of different thickness, that nanoscale organization of the morphology is more crucial for high efficiency of solar-cell devices than absorption alone. This implies that thicker films absorb more light, but they possess less favorable morphological characteristics and, thus, result in a poor functioning of the solar-cell devices [135]. In conclusion, it exists a tradeoff between position-dependent exciton formation with subsequent transportation to the D/A interface and optimized charge transport to the respective electrodes, providing current in the external circuit.

In the following study, we investigate the impact of the architecture and composition of the full device on its absorption efficiency and EQE. To tackle the large system sizes, we used the parameterized field-based solar-cell algorithm, to take into account the composition dependents of the exciton dissociation and charge-transfer rates, in conjunction with a modified version of the transfer-matrix method, to include the space-dependence of the absorption. To evaluate the EQE, which is the primary parameter reflecting the fundamental properties of the full photovoltaic device, we will calculate the absorption efficiencies for a series of bulk heterojunction morphologies, with different degree of phase separation. The values of the EQE will be compared with the available experimental data. Moreover, we will analyze how the degree of phase separation affects the exciton- and charge-losses, crucially influencing the EQE of the devices.

8.2 Modified transfer-matrix method for bulk heterojunctions

To perform optical modeling, optical constants are required as input for the calculations. For instance, in case of the PFB/F8BT bilayer the necessary optical constants can be taken from the experimental measurements of the pristine PFB and F8BT. Thus, the exciton creation distribution, $Q_j(z)$, can be computed using the relevant values for the optical constants and thicknesses of each layer. In our calculations the substrate thickness has been chosen large enough, so that interference effects can be neglected, and, thus, the calculation result is independent of this parameter [139]. The thicknesses for the remaining layers of the device structure were taken to be (in nm): 110 | 35 | 50 | 200. The corresponding exciton generation profile, normalized with regard to its peak value, for the PFB(25 nm)/F8BT(25 nm) bilayer morphology, is shown in Fig. 8.1.

Another difficulty with bulk heterojunctions is that their morphologies strongly depend on the chemical constitution of the polymers as well as the history of production. Therefore, the optical constants determined from experimental measurements of blends would not be much use as input for our theoretical calculations. We point out that as a first approximation Bruggeman effective medium approximation (EMA) would be useful, to combine the data for pristine PFB and F8BT. However, using the EMA or the experimental data for a related blend is not accurate, since it is practically impossible to obtain exactly the same structure. To overcome this problem, we have developed the so-called bulk heterojunction transfer-matrix method (BTM), which will be described in detail in the following. First of all, we discretized the active layer of the device with thickness z nm into $n = x \cdot y \cdot z$ subunits, each of which represented either a part of the electron- or hole-conducting phase. Thus, the total number of parallelepipeds, to which we applied the matrix formalism, was $k = x \cdot y$, each consisting of z subunits. Moreover, in order to efficiently reduce the computational costs, we have joined sequentially repeated subunits of the electron- or hole-conducting phases together, to create a sublayer with the respective thickness. For instance, if the active layer consisted of 20 subunits of PFB, 10 subunits of F8BT and again 20 subunits of PFB, it was considered as three sublayers with thicknesses of 20, 10 and 20 nm in our algorithm. We note that, since the refractive index within one phase is uniform, the grouping of different number of sublayers into bigger layers has no effect on the calculation results. Afterwards, when all exciton-generation profiles with total number k were calculated, they were introduced as input into our DMC algorithm, enabling to take into account

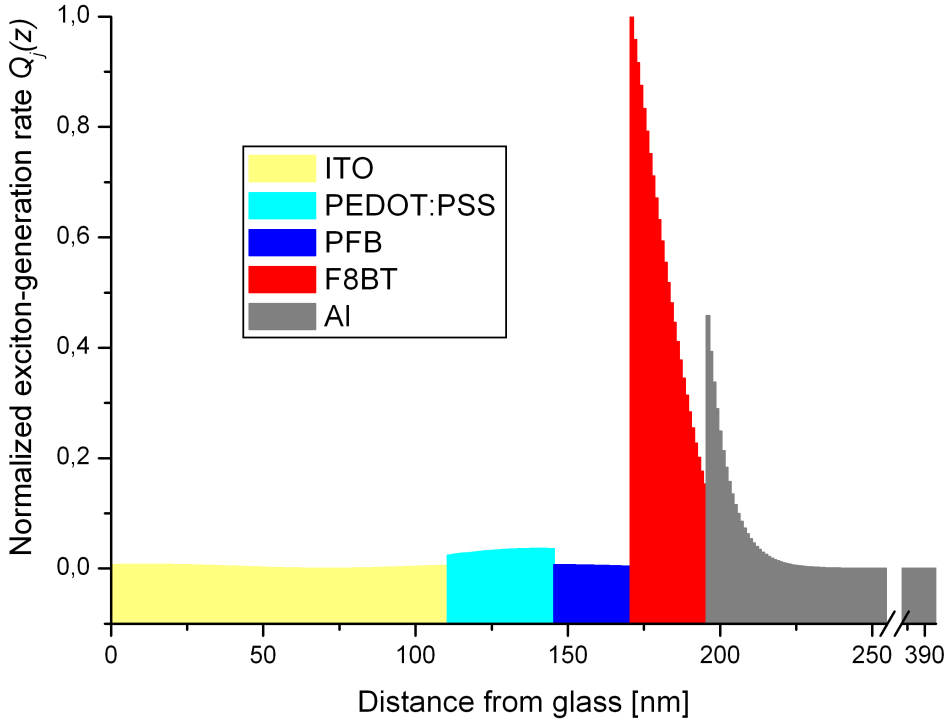

Figure 8.1: Exciton-generation profile (normalized with regard to its peak value) of the bilayer device under AM 1.5 illumination, calculated using transfer-matrix method.

the exciton-creation rates as a function of the morphological characteristics of the active layer of the full device. We call this approach the BTM-DMC-SCFT method. The new procedure permitted us to calculate the absorption efficiency, η_A, for the bulk heterojunction morphologies and, ultimately, to calculate the EQE.

8.3 Simulation details

To compute the morphologies with different degree of phase separation, generated during the production process as well as the equilibrium morphology for PFB/F8BT blends, we made use of the dynamic- as well as static-SCFT method, respectively. To this end, we considered a system, composed of $A_{20}D_{20}$-homopolymers. For the generation of the morphologies, we used a Flory-Huggins interaction parameter of $\chi_{AD} = 0.382$, which was taken from experimental results, and a polymer segment fraction of $f_A = 0.5$ [140]. The simulation box was constituted of $50 \times 50 \times 50$ grid points with a spatial mesh width of $\Delta x = \Delta y = \Delta z = 0.5$ in units of the statistical segment length b (that is taken to be unity). The periodic boundary conditions were applied along the x- , y- and z-direction. The contour-step size along the chain was chosen as $\Delta s = 0.25$ and the relative accuracy for the computed free energy as 10^{-4}. For the numerical integration, we used a time step of $\Delta t = 0.01$ and a mobility parameter of $L_K = L = 1.0$.

For the DMC-calculations, we used the same parameters as in chapter 7, with the only difference that for the full device calculations we introduced the exciton-generation profiles, as well as absorption efficiency, η_A, of the bulk heterojunctions as input into the DMC algorithm. Besides, we performed additional calculations, where we took into account the exciton-generation profiles, but neglected the effect of mixing of the D/A-components. We call this approach conventional BTM-DMC-SCFT. This allowed us to assess the influence of optical absorption in different regions of the photoactive layer on the photovoltaic performance of the devices.

8.4 Results

To study the influence of the optical absorption distribution within the bulk heterojunction on photovoltaic performance, we have computed a series of morphologies with different degree of phase separation, using either the dynamic- or static-SCFT method. In Fig. 8.2 we show them as a function of processing time and at equilibrium. By comparing these morphologies, we infer that the nanoscale phase separation improves with increasing simulation time by changing from an unordered to an ideal lamellar-like structure. Moreover, we observe that with increasing time the size of the D/A interface decreases, which is confirmed by the plot in Fig. 8.3(d), where we show the decrease of interfacial area as a function of simulation time.

Next, in Fig. 8.3 (a-c) we show the results for the IQE, EDE and CTE as a function of time, obtained with the different DMC-SCFT algorithms, described previously. By comparing the results presented in Figs. 8.3 (b) and 8.3 (d), we conclude that the EDE, obtained with all three methods, decreases with decreasing interfacial area. This indicates that PFB and F8BT are phase separated on a scale, which is significantly larger than the exciton diffusion length, leading to a large number of exciton losses. Moreover, we observe that the difference in EDE between conventional DMC-SCFT and conventional BTM-DMC-SCFT results is only small, i.e. around 1 % for all simulation times, excepting for the equilibrium. This shows that the EDE does not significantly depend on the form of the exciton creation distribution. However, we notice that there is a noticeable discrepancy between the parameterized BTM-DMC-SCFT results, where the effect of mixing of D/A-components on the exciton and charge-transfer rates has been included, and the results obtained with the other two methods previously mentioned (conventional DMC-SCFT and conventional BTM-DMC-SCFT). From these observations we conclude that the impact of mixing of the D- and A-components on the EDE is much larger than the absorption of the individual nanophases.

Next, we consider in Fig. 8.3(c), the CTE as a function of simulation time. In case of

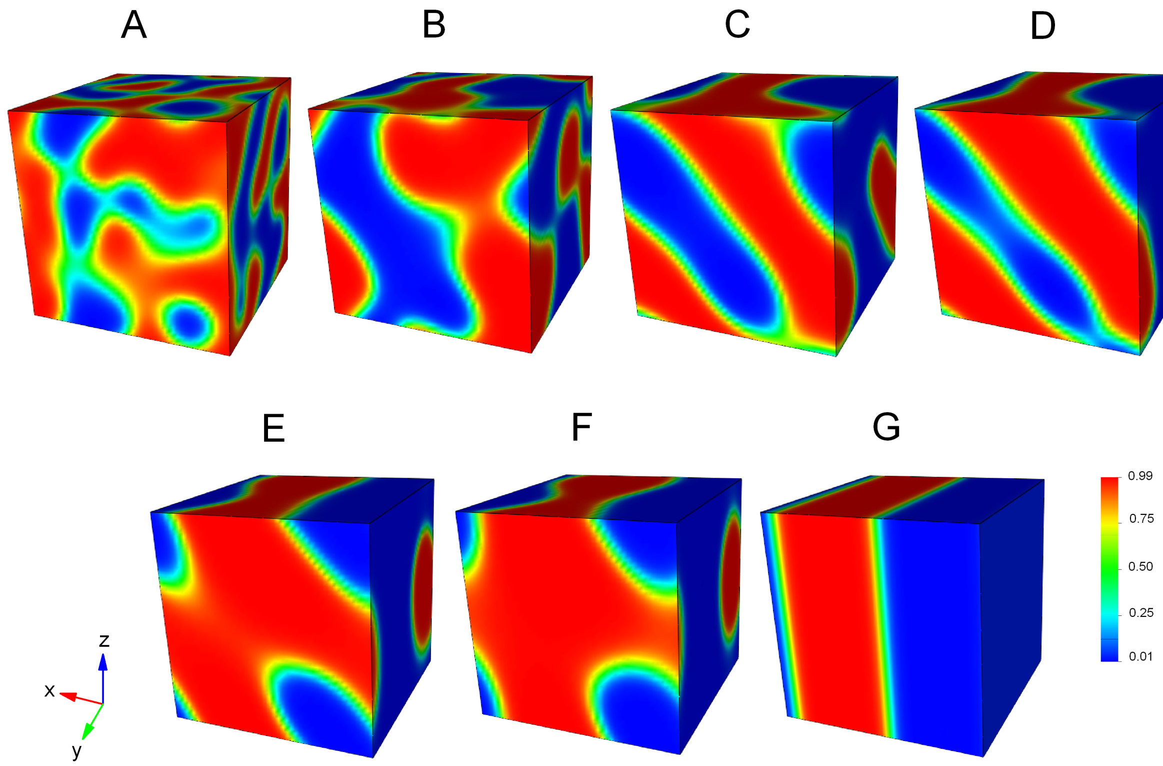

Figure 8.2: Volume fractions of the PFB/F8BT-blend system, composed of $A_{20}D_{20}$-homopolymer as a function of time, calculated either with the dynamic- or static-SCFT method. Time t = (A) 200; (B) 500; (C) 800; (D) 1100; (E) 1500; (F) 1800; (G) equilibrium structure. The direction of the axes are shown in the left bottom angle.

the conventional DMC-SCFT and the conventional BTM-DMC-SCFT methods, we observe an increase of the CTE as the processing time evolves and the degree of phase separation increases. By contrast, in case of parameterized BTM-DMC-SCFT calculations, we see that the CTE is significantly lower compared to the CTE's of the other approaches. This can be explained by the fact that the high fraction of electrons and holes will be lost through the process of electron-hole recombination, due to the low transfer rates in opposite phases. This phenomenon has been investigated by Brenner *et al.* [131], who showed using simultaneous photoluminescence and photocurrent mapping that the intermixing between PFB and F8BT phases results in efficient geminate recombination. Moreover, Snaith *et al.* [128] showed through photoluminescence and atomic force microscopy measurements that the charges generated within the bulk of PFB or F8BT do not have much influence on the device performance, while the majority of these charges undergo geminate recombination or are trapped in the bulk.

In addition, by analyzing the results in Fig. 8.3(a), we conclude that the IQE's from the conventional DMC-SCFT and conventional BTM-DMC-SCFT calculations completely follow the

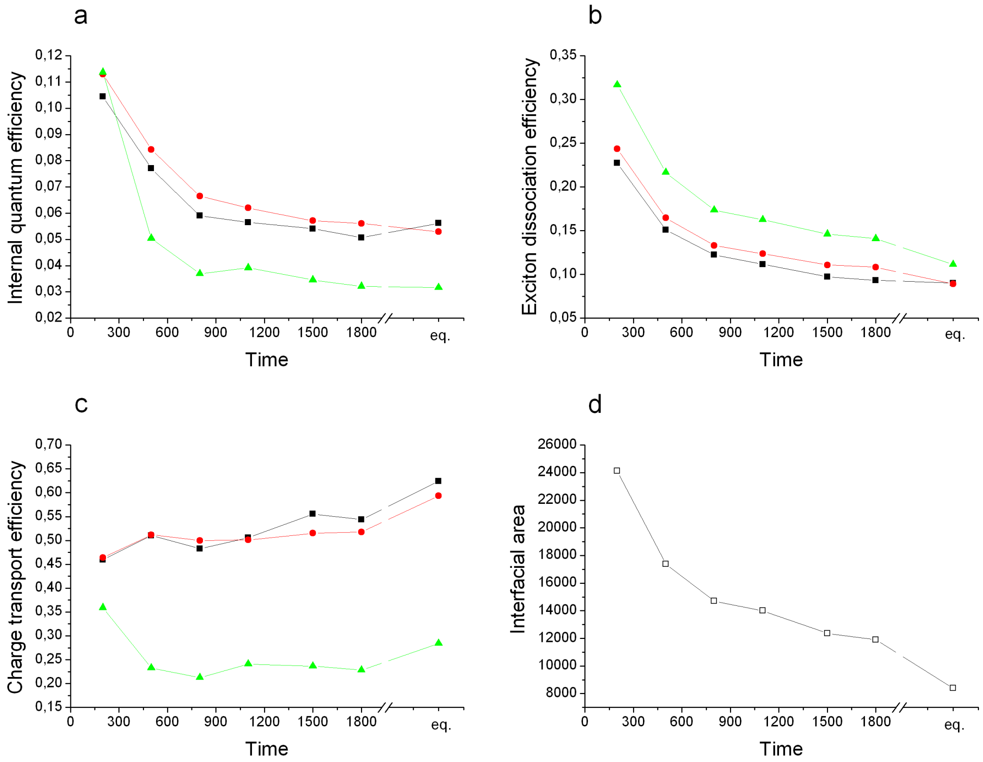

Figure 8.3: (a-c) Efficiencies of PFB/F8BT-blend system as a function of time, obtained by using the conventional DMC-SCFT (black line with squares), conventional BTM-DMC-SCFT including only exciton generation profiles without parameterization of the exciton-dissociation and charge-transfer rates (red line with circles) or parameterized BTM-DMC-SCFT (green line with triangles). (d) Interfacial area of PFB/F8BT-blend system as a function of time, using dynamic- and static-SCFT method.

functional dependence of the respective EDE's. By contrast, we observe that the parameterized BTM-DMC-SCFT method produces much lower values for the IQE. This essentially relates to the lower CTE, which is generally not compensated by the higher EDE, as can be deduced from Figs. 8.3 (b) and (c). However, we point out that the highest IQE was obtained for the parameterized BTM-DMC-SCFT calculation at time $t = 200$, where the increase of the EDE was large enough to compensate the deterioration of the CTE.

Finally, to evaluate the EQE's, which includes photon and exciton losses through interference effects caused by reflection and transmission at the D/A interfaces, we have calculated absorption efficiencies, using the BTM method previously mentioned. In Fig. 8.4 (b), we observe a gradual increase of the absorption efficiency with increasing time and degree of phase separation. The difference in absorption efficiency between structures A and G in Fig. 8.2 reach almost 30 %.

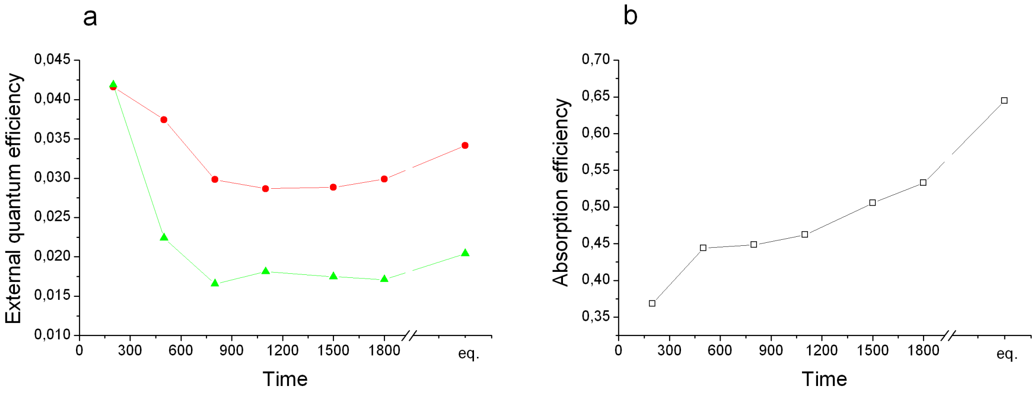

Figure 8.4: (a) External quantum efficiencies of PFB/F8BT-blend system as a function of time, obtained either with the conventional BTM-DMC-SCFT including only exciton generation profiles without parameterization of the exciton-dissociation and charge-transfer rates (red line with circles) or parameterized BTM-DMC-SCFT (green line with triangles). (b) Absorption efficiency of PFB/F8BT-blend system as a function of time, computed using the BTM method.

From these findings we conclude that the scale of phase separation of the photoactive layer not only affects the exciton-dissociation and charge-transport processes, but also the amount of photons absorbed by the device. In Fig. 8.4 (a), we visualize the values of EQE as a function of simulation time. At the beginning, the EQE quite strongly decreases from almost 4.2 % to around 1.5 %. Subsequently, the quantity oscillates around the value of 1.75 % up to the time $t = 1800$ and, ultimately, increases again to the value of 2.0 % for the equilibrium structure. This can be explained by the fact that the structural dynamic evolution between structures A and C, depicted in Fig. 8.2, leads to a significant change in the degree of phase separation, which coincides well with the drop in exciton dissociation yield. In the later stage, up to a time $t = 1800$, the system does not undergo major structural changes, resulting in a slower decrease in the EDE and to a slight improvement in the CTE. Finally, the increase in the EQE for the equilibrium morphology is mainly attributed to the high absorption efficiency. In this situation the system possesses the highest number of excitons generated for the given number of incident photons, together with an improved charge-carrier transport to the electrodes, due to a large number of direct percolations throughout the active layer. The experimental values of EQE for PFB/F8BT blends is also rather low, typically less then 4 % under short-circuit condition [141]. Moreover, it has been found experimentally that the EQE strongly depends on the morphology characteristics. For instance, McNeill *et al.* [141] observed that increasing annealing temperature of blend thin films causes a large degree of phase separation, improving the device performance substantially. Moreover, they discussed that increasing annealing temperature above 140° C leads to a deterioration of the EQE, which was attributed to a reduction in exciton dissociation yield. This concord well with the results from our parameterized BTM-DMC-SCFT method.

In conclusion we notice that the simulated EQE's in the range of 1.5 - 4 % are in good agreement with the values experimentally measured, which depend on the processing conditions influencing nanoscale phase separation, and are in the range of 1.5 - 4 % [132, 141, 142]. In addition, Coffey and Ginger [132] found through time-resolved electrostatic force microscopy on their PFB/F8BT blends a complicated relationship between the values of EQE and the blend composition. They observed that, although the EQE for the PFB/F8BT ratio of 50:50 is significantly larger than for the pure polymers and is about 2.5 %, the maximum EQE is around 3.5 % for a PFB/F8BT ratio of 35:65. To conclude, we emphasize that the parameterized BTM-DMC-SCFT method is suitable for large system-size calculations of technological relevance. Although it does not take into account the polymer structure explicitly, like the particle-based algorithm presented in section 7.2, it enables the computation of the photovoltaic behavior of PSCs with reasonable accuracy at moderate computational costs.

Chapter 9

Summary and conclusions

The goal of my thesis was to develop and apply field-based multiscale modeling techniques, to better understand and improve the performance of nanodevices, used in optoelectronic applications. A particular focus has been put on polymer solar cells, PSCs, which have attracted considerable attention in the past decade due to their easy manufacturing, high flexibility, light weight and low production costs. However, despite the significant progress in their development and experimental characterization, their power conversion efficiencies have been found to be significantly lower compared to their inorganic counterparts. In the last years it has been established by both experimental and theoretical means that the low power conversion efficiencies are related to loss phenomena of elementary particles of the photovoltaic process, which are favored by bad morphological characteristics of the donor-acceptor heterojunctions. To this day, there are many theoretical studies attempting to gain some insight into the relationship between the morphology of PSCs and their photovoltaic performance. However, the main drawback of these approaches is that the underlying techniques for morphology generation do not rely on realistic polymer models and, therefore, do not allow to introduce chemical details. Another difficulty is that some of the algorithms for simulating photovoltaic behavior do not take into account all the elementary processes, associated with excitons or charges. Moreover, most of them do not consider the structural heterogeneity of polymeric morphologies, which has recently been found to be of great importance for PSCs.

To overcome these problems, we proposed in this thesis a coupled multiscale method based on combining the SCFT method, for computing the polymeric morphologies with arbitrary chain architecture and topology, with a suitable DMC algorithm, to simulate the photovoltaic processes at different level of description. The application of this coupled multiscale approach enabled us to treat a large variety of polymer systems of large system size at low computational costs.

To reach these goals, we started in Chapter 2 with a detailed description of the static- and dynamic-SCFT method, allowing the determination of polymer morphologies at different stages of the phase separation process and at equilibrium under different external conditions, encountered in standard experimental investigations. Subsequently, in Chapter 3 we introduced theories, which were used in the DMC algorithms for describing the creation and transport of the elementary particles within the active layer of OPV devices. To describe the exciton transport within the material, we used the Förster resonance energy transfer theory, whereas to describe the charge transport we used the Marcus theory. To close the theoretical part, in Chapter 4 we provided a detailed description of the DMC model and its coupling with the SCFT method. Moreover, in the last section of this chapter we introduced the transfer-matrix method, which was used to determine the absorption efficiency, depending on the structural characteristics of the polymer heterojunction, by taking into account optical interference effects.

In the subsequent part of this thesis, we presented and discussed the results, generated with the DMC-SCFT algorithms introduced previously. In Chapter 5 we have investigated the causes affecting the photovoltaic performance of block-copolymer systems with changing chemical characteristics and mechanical load, which might be useful in flexible applications. Moreover, we have studied the suitability of block-copolymer systems for the use as charge storage devices. Our multiscale DMC-SCFT approach, employed in these applications, was based on combining the static-SCFT method, to generate the equilibrium nanostructured morphologies, with a version of the DMC algorithm, where interfacial mixing of the donor and acceptor components have been neglected. We applied this approach on systems composed of $A_{20}D_{20}$-diblock- and $A_{10}D_{20}A_{10}$-triblock-copolymers, where the A- and D-blocks consisted of (alkyl)-substituted poly(perylene diimide-alt-dithienothiophene) alkyl-substituted PPDI-DTT and (alkyl)-substituted bis (thienylene vinylene) - substituted polythiophene alkyl-substituted biTV-PT, respectively. We found that in the range from low up to intermediate χ-parameters an increasing number of continuous percolation paths are formed for both block-copolymer systems. The morphologies with a high degree of phase separation and with the largest number of continuous percolation paths to the electrodes possess the highest CTE and IQE. Moreover, we found that the maxima in the CTE and IQE for these morphologies correlate well with the minima in the number of charge losses, resulting from electron-hole recombinations. By further increasing the interaction strength between the monomers, we observed an increase in the total number of defects, i.e. bottlenecks and dead ends, causing a rise in the number of locations, where charge losses, due to charge recombination and charge accumulation, can occur. The increase in charge accumulations as well as the decrease of the interfacial length with increasing χ-parameter for both block-copolymer systems are the primary factors for the deterioration of the EDE, leading to substantial charge carrier loss. From these observations, we concluded that the charge-loss mechanisms, mentioned previously, result in a significant drop in the CTE and IQE for both types of block-copolymer systems in this parameter range. Moreover, we observed that the diblock-copolymer system possesses a slightly higher IQE than the triblock-copolymer system over the whole range of χ-parameters. This essentially relates to its larger CTE, which is not compensated by the higher EDE in the triblock-copolymer case. By analyzing the impact of mechanical loads on the photovoltaic performance of the triblock-copolymer morphology with the highest IQE, we observed a successive degradation in the performance of the solar cell with increasing external mechanical stress. We found that the degradation relates to the local deformation of the nanophases, caused by the different mechanical loads, imposed on the system. From the study, we concluded that the deterioration in the IQE results from the growing number of charge losses, due to charge recombination and charge accumulation, in the deformed nanophases. Finally, we have also demonstrated the suitability of triblock-copolymer systems for charge storage applications. We found that the captured charges can be stored for a certain period of time and, then, regained by changing the polarity of the electrodes. Moreover, we observed a fast decay of charges at the beginning of the uncharging process. In the final stage of the uncharging process the curve attained a plateau, which shows that some of the charges remain trapped in the defects and, thus, cause a decrease of the charge storage efficiency of the device.

In Chapter 6 we studied the influence of external effects and impurities on the active layer, encountered in realistic photovoltaic applications. In the first part of this chapter we investigated the usefulness of a well-established post-production technique, known as electric-field alignment, to improve the photovoltaic performance of PSCs. To this end, we used the same DMC-SCFT approach as mentioned previously, however, by focusing on systems composed of A_5D_{15}-diblock- and $A_3D_{12}A_3$-triblock-copolymers. Our simulation results revealed that the electric-field post-production technique has a huge influence on their photovoltaic performance. We explained these findings by the formation of an increased number of ideal continuous percolation paths to the electrodes with growing strength of the electric field. The electric field caused a reorientation of the nanophases with respect to the electric-field lines, improving charge separation at the D/A interface and charge diffusion to the electrodes. In the subsequent part we studied the influence of surface interactions, originating from the electrodes, on the photovoltaic performance of PSCs. These have been found of crucial importance for their device efficiency in recent experimental works. From our calculation results, we inferred that the CTE of the morphologies with a surface interaction of $\zeta_2 \geq 0.03$ increases more than ten times with regard to the morphology without surface interaction. This showed that by changing the surface interaction it is possible to obtain an optimized morphology with direct contacts between the nanophases and the electrodes. Furthermore, we have studied the influence of impurity particles, which might result from the diffusion of electrode material into the active layer, on the stability and performance of diblock-copolymer solar cells. From our calculations, we concluded that even trace impurities can significantly affect the morphology of the active layer of the device and, thus, significantly reduce its photovoltaic performance. In particular for the case of two and three impurity particles with a radii of $r = 1.6$ nm, we observed a complete phase transformation of straight cylinders into spheres, which can be attributed to the loss of conformational entropy due to the stretching of the polymer chains. In addition, by increasing the loading of the particles, we observed a degradation of the percolation pathways to the electrodes and, thus, a gradual decrease in the

IQE with increasing volume fraction of the impurities.

In Chapter 7 we have investigated the effect of mixing of the D- and A-components on the performance of PSCs, using a field-based multiscale solar-cell algorithm. To this end, we have extended our conventional DMC-SCFT approach, where the effect of mixing of the D- and A-components has been neglected, by introducing the composition dependence of the exciton-dissociation frequency and charge-transfer integrals into the algorithm. The new method was called the parameterized field-based multiscale solar-cell algorithm. Using this algorithm, we studied polymer blends, composed of poly(9,9-dioctyl fluorene-co-bis-N,N-(4-butylphenyl)-bis-N,N-phenyl-1,4-phenylene-diamide) PFB and poly(9,9-dioctyl-co-benzo-thiadiazole) F8BT. Our simulation results revealed that the mixing of the D- and A-components at the D/A interface of the PFB/F8BT blends provides a substantial contribution to the EDE, which has a strong influence on the photovoltaic performance of PSCs. Moreover, we found that it has also a major impact on the CTE, caused by a reduced charge mobility as well as an increased number of charge recombinations, induced by poor charge transfer properties of the electrons and holes in the D- and A-phases. Overall, we noticed that the parameterized field-based approach provides a value for the IQE, which is two times higher than the one provided by the conventional field-based approach, but is in good agreement with the one provided by the atomistic approach, reflecting the realistic situation. By analyzing the electron- and hole-current densities, we showed in addition that in the parameterized field-based approach, in contrast to the conventional field-based approach, the photocurrent is preferentially generated within the polymer nanophases and that the major part of the charge transport takes place at the phase centers, similar as in the atomistic particle-based solar-cell approach. Finally, we investigated the effect of photo-oxidation of the fluorene moieties of the F8BT phase on the photovoltaic performance of the PSCs. It has been found in previous experimental investigations that the photodegradation processes strongly reduce the long-term stability of PSCs, preventing their commercial use. With increasing fraction of the photo-oxidized F8BT monomers, we observed a lowering of the electron transfer rates, which favors electron-hole recombination. This caused a deterioration of the CTE and, ultimately, a lowering of the device performance.

To conclude, we studied in Chapter 8 the impact of the architecture and composition of the full nanodevice on its absorption efficiency and EQE. For this purpose, we combined the parameterized field-based solar-cell algorithm with a modified version of the transfer-matrix method, which was employed to determine the optical absorption distribution within the photoactive layer of PFB/F8BT blends. This enabled us to take into account all major effects, affecting the performance of full nanodevices, at moderate computational costs. By analyzing a series of bulk heterojunction morphologies with different degree of phase separation, we found that the absorption efficiency of the individual nanophases has no significant influence on the EDE of the device, in contrast to the mixing of the D- and A-components. The latter effect directly correlates with the scale of phase separation, which has been found to play an important role in the device performance of PSCs in previous experimental investigations. However, we point out that the amount of photons absorbed by the device, has a direct influence on the EQE. Overall, we found that the simulated EQE's in the range of 1.5 - 4 % were in good agreement with the experimentally measured values, which strongly depend on the processing conditions affecting the scale of phase separation of the nanostructured morphologies.

In conclusion, in this thesis we have introduced various field-based multiscale solar-cell algorithms for simulating photovoltaic processes in PSCs. To take into account the major effects, affecting their photovoltaic performance, we have continuously improved these techniques, to enable large system-size calculations of full nanodevices at moderate computational costs. To this end, we proposed an extension of the conventional DMC-SCFT approach by parameterizing the processes associated with exciton dissociation as well as charge transport depending on the composition of the photoactive layer. In a future work we plan to extend the range of applicability for the parameterized DMC-SCFT approach through further algorithmic developments. In particular, throughout this thesis we assumed that the built-in electric field from the electrodes is uniform. This is an approximation and could be improved by supplementing the DMC algorithm with an additional step, where the Poisson equation is solved [143]. Another improvement, which would extend the range of applicability of our DMC-SCFT approach to a broader class of solar-cell materials, would be to modify the underlying SCFT method, described in chapter 2, for computing morphologies consisting of semicrystalline polymer materials. Semicrystalline PSCs have been found to reach efficiencies on the order of 6 % [145, 146]. Finally, it would also be of great interest to investigate in more detail the influence of processing conditions, such as solvent evaporation rate and annealing conditions, as well as additives, on the performance and stability of the PSC devices [116, 135, 144].

Appendix A

Supporting material to chapter 5

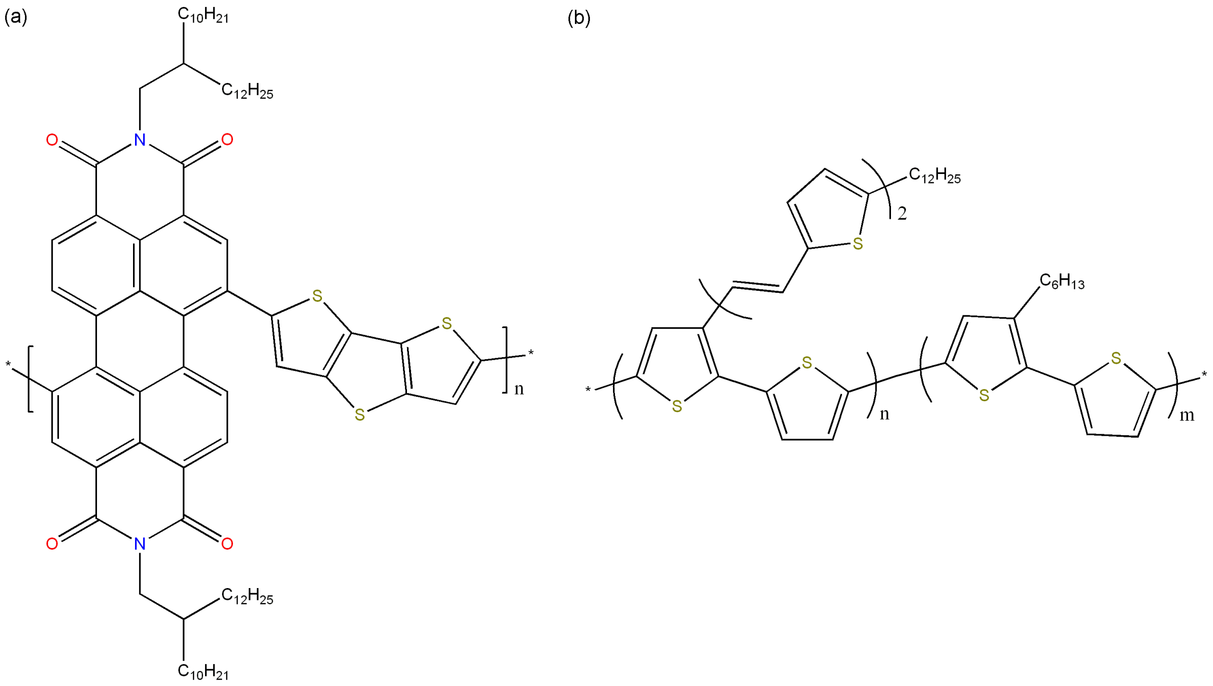

Figure A.1: Chemical structures of the *D*- and *A*-type monomers composed of blocks of (a) (R1,R2)-substituted poly(perylene diimide-alt-dithienothiophene) and (b) (R1,R3)-substituted bis(thienylenevinylene)-substituted poly-thiophene.

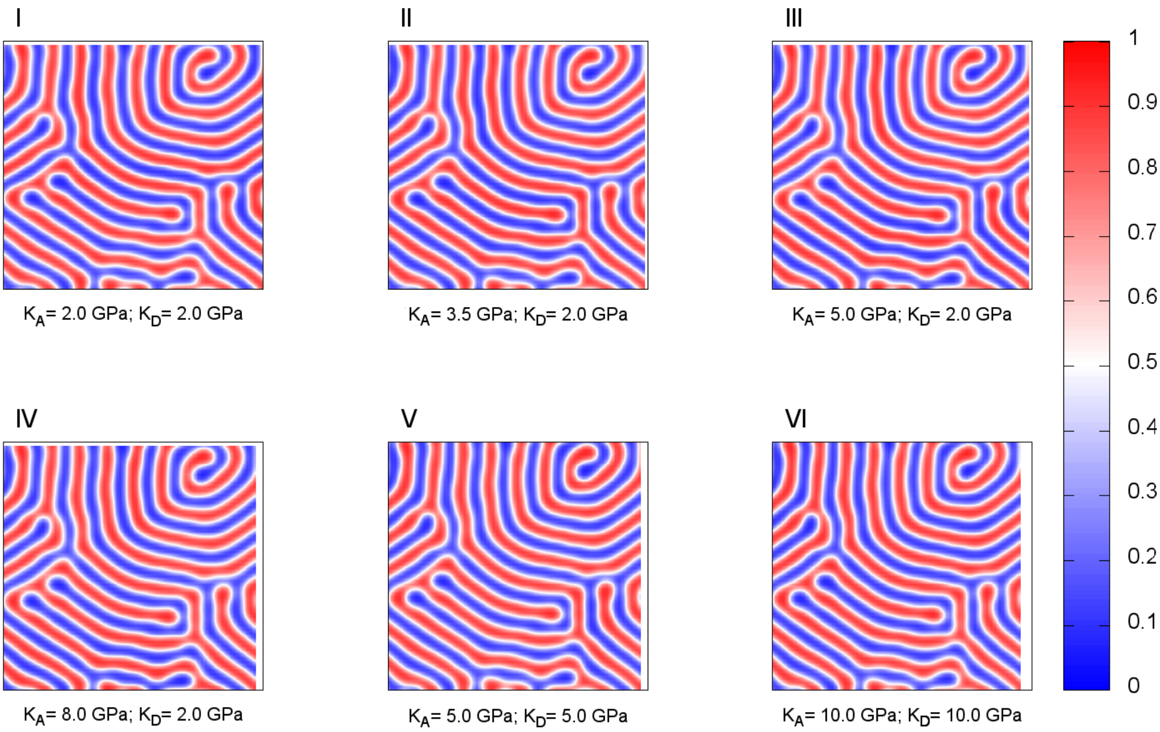

Figure A.2: Volume fractions of the strained $A_{10}D_{20}A_{10}$-triblock copolymer morphologies at mechanical load of 0.1 N/m^2 for different values of bulk moduli of acceptor ($\mathrm{K_A}$) and donor ($\mathrm{K_D}$) phases [red: majority of A phase (electron-conducting); blue: majority of D phase (hole-conducting)].

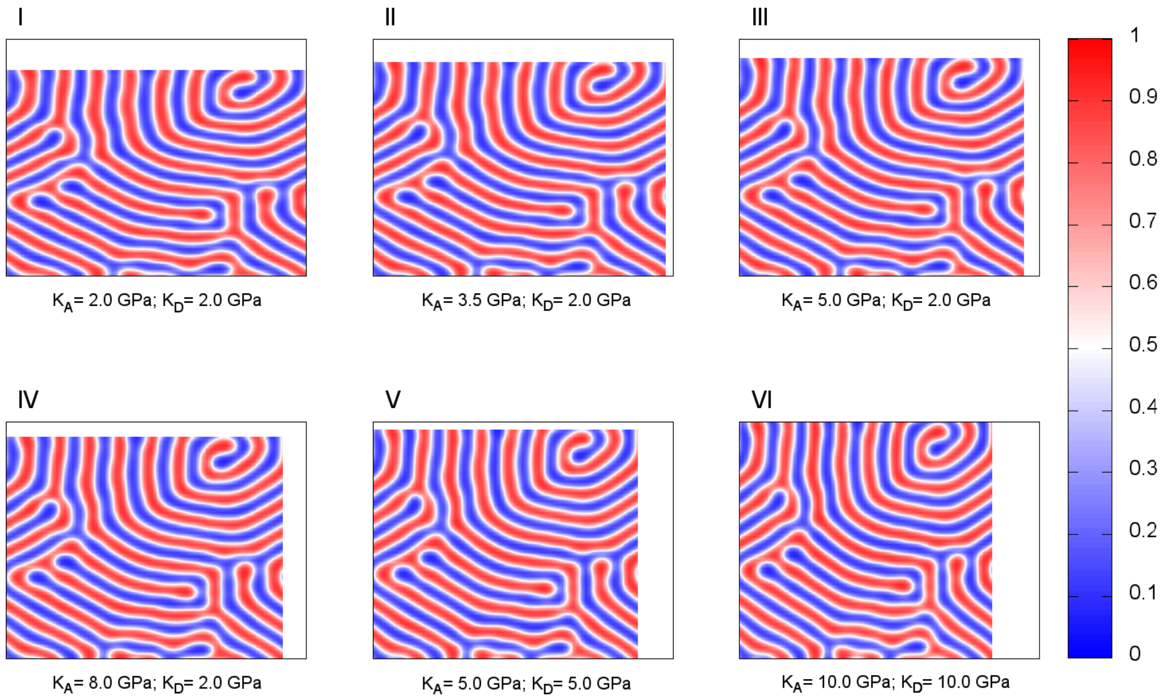

Figure A.3: Volume fractions of the strained $A_{10}D_{20}A_{10}$-triblock copolymer morphologies at mechanical load of 0.5 $\mathrm{N/m^2}$ for different values of bulk moduli of acceptor ($\mathrm{K_A}$) and donor ($\mathrm{K_D}$) phases [red: majority of A phase (electron-conducting); blue: majority of D phase (hole-conducting)].

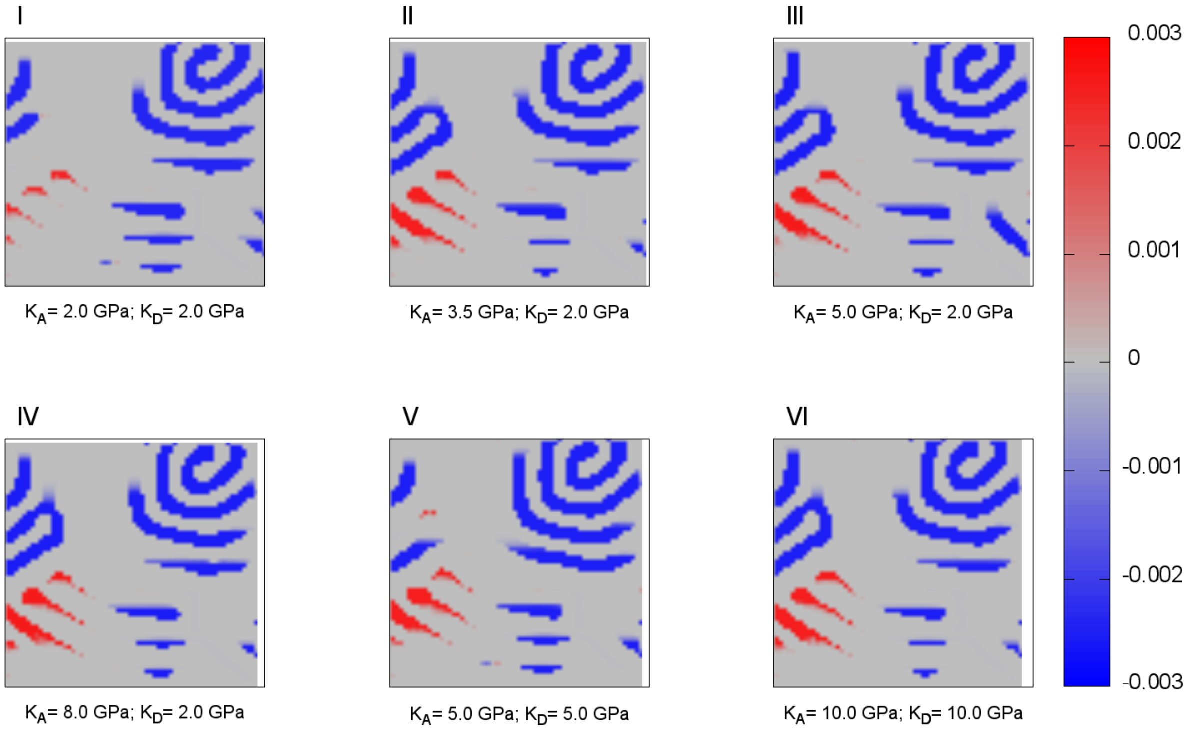

I: K_A= 2.0 GPa; K_D= 2.0 GPa

II: K_A= 3.5 GPa; K_D= 2.0 GPa

III: K_A= 5.0 GPa; K_D= 2.0 GPa

IV: K_A= 8.0 GPa; K_D= 2.0 GPa

V: K_A= 5.0 GPa; K_D= 5.0 GPa

VI: K_A= 10.0 GPa; K_D= 10.0 GPa

Figure A.4: Charge density distributions of the strained $A_{10}D_{20}A_{10}$-triblock copolymer morphologies at mechanical load of 0.1 N/m^2 for different values of bulk moduli of acceptor ($\mathrm{K_A}$) and donor ($\mathrm{K_D}$) phases [blue: negative charge (electron); red: positive charge (hole)].

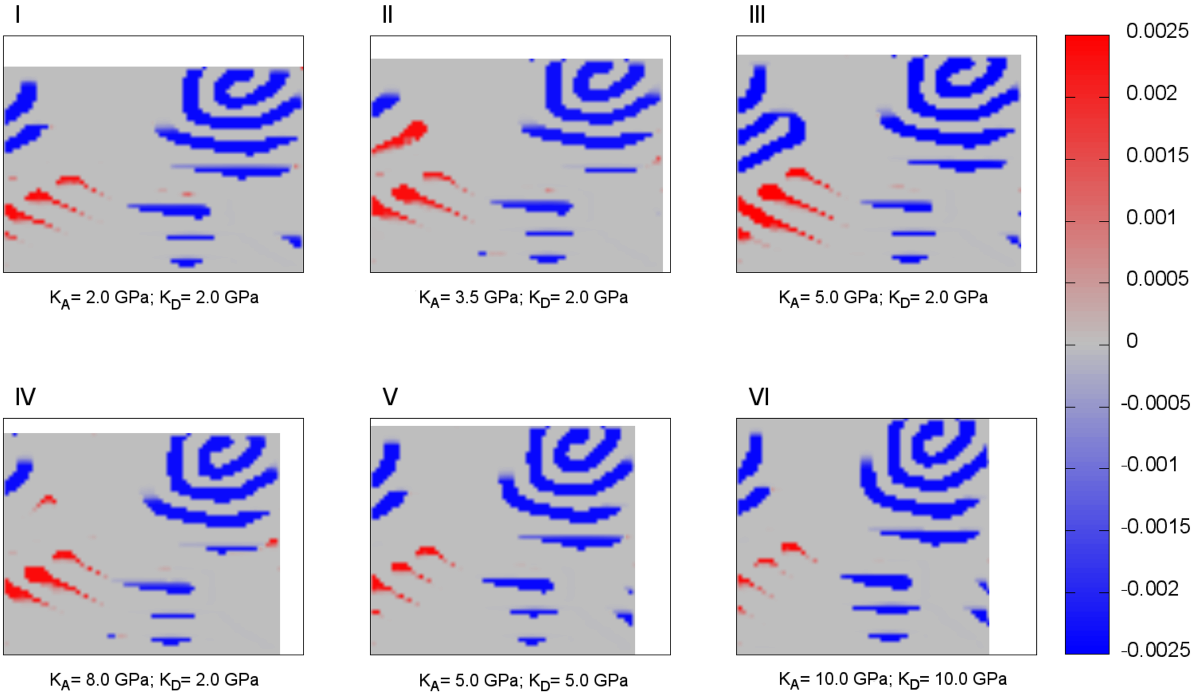

Figure A.5: Charge density distributions of the strained $A_{10}D_{20}A_{10}$-triblock copolymer morphologies at mechanical load of 0.5 N/m^2 for different values of bulk moduli of acceptor ($\mathrm{K_A}$) and donor ($\mathrm{K_D}$) phases [blue: negative charge (electron); red: positive charge (hole)].

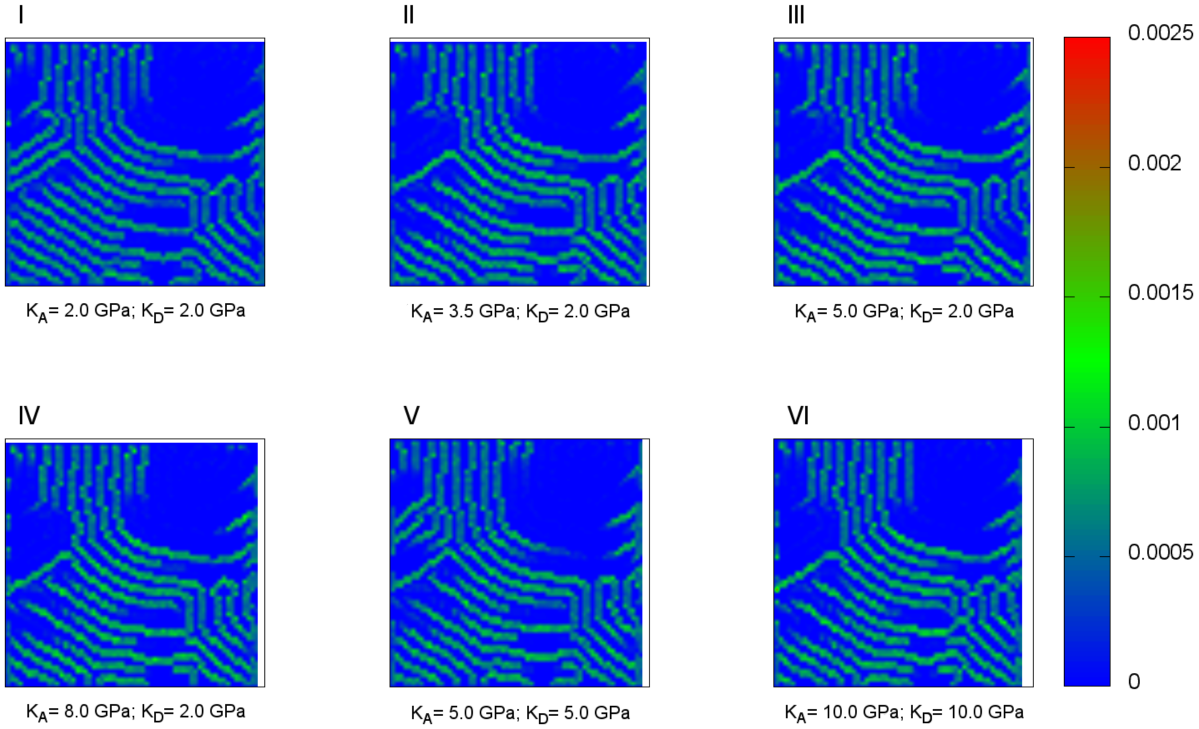

K$_A$= 2.0 GPa; K$_D$= 2.0 GPa
K$_A$= 3.5 GPa; K$_D$= 2.0 GPa
K$_A$= 5.0 GPa; K$_D$= 2.0 GPa
K$_A$= 8.0 GPa; K$_D$= 2.0 GPa
K$_A$= 5.0 GPa; K$_D$= 5.0 GPa
K$_A$= 10.0 GPa; K$_D$= 10.0 GPa

Figure A.6: Frequencies of exciton dissociation of the strained $A_{10}D_{20}A_{10}$-triblock copolymer morphologies at mechanical load of 0.1 N/m^2 for different values of bulk moduli of acceptor (K$_\mathrm{A}$) and donor (K$_\mathrm{D}$) phases.

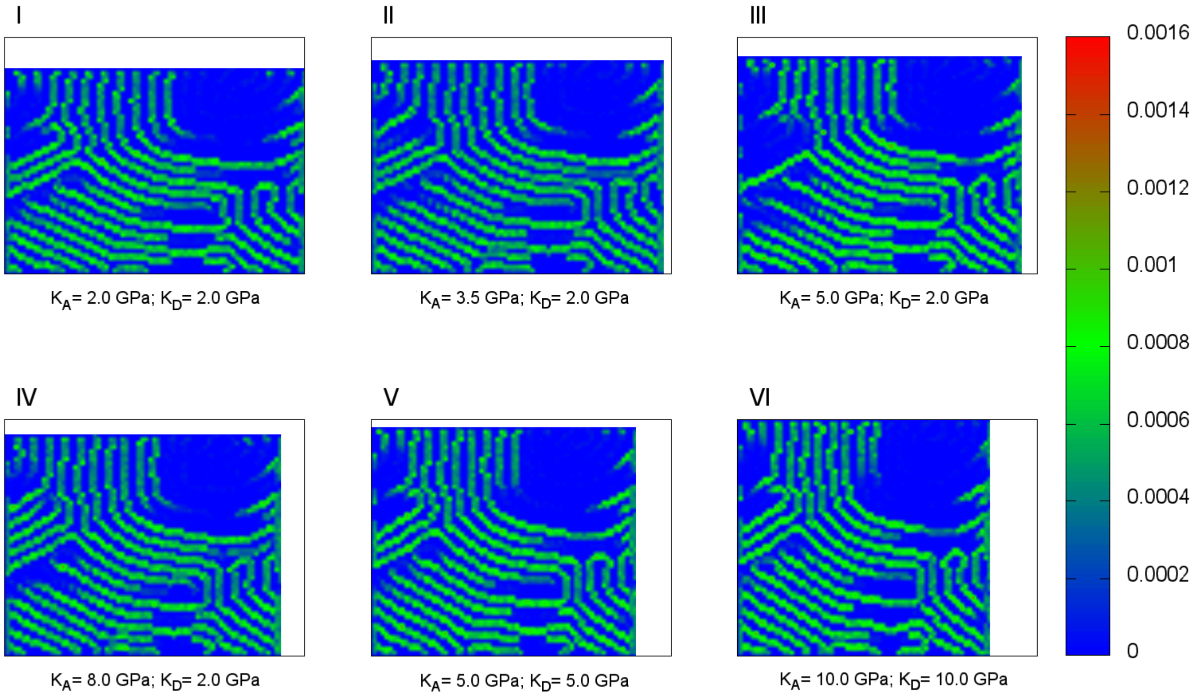

I: K_A= 2.0 GPa; K_D= 2.0 GPa

II: K_A= 3.5 GPa; K_D= 2.0 GPa

III: K_A= 5.0 GPa; K_D= 2.0 GPa

IV: K_A= 8.0 GPa; K_D= 2.0 GPa

V: K_A= 5.0 GPa; K_D= 5.0 GPa

VI: K_A= 10.0 GPa; K_D= 10.0 GPa

Figure A.7: Frequencies of exciton dissociation of the strained $A_{10}D_{20}A_{10}$-triblock copolymer morphologies at mechanical load of 0.5 N/m^2 for different values of bulk moduli of acceptor ($\mathrm{K_A}$) and donor ($\mathrm{K_D}$) phases.

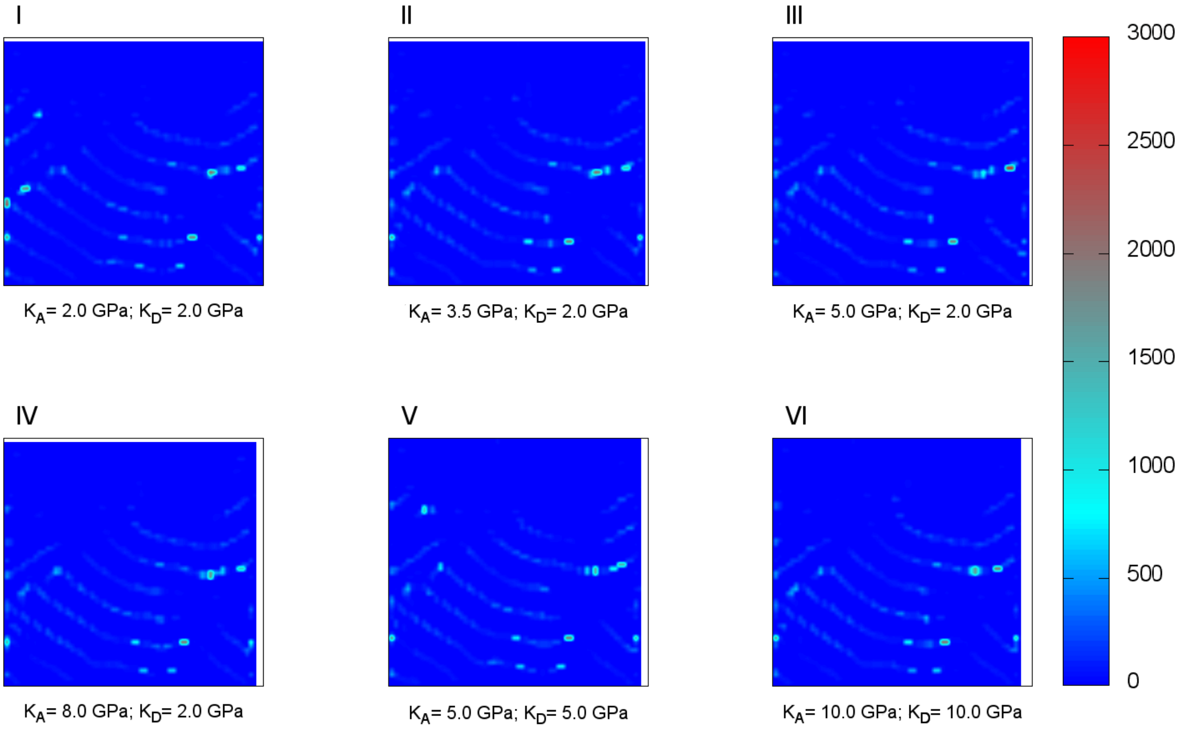

Figure A.8: Charge recombination number distribution of the strained $A_{10}D_{20}A_{10}$-triblock copolymer morphologies at mechanical load of 0.5 $\mathrm{N/m^2}$ for different values of bulk moduli of acceptor ($\mathrm{K_A}$) and donor ($\mathrm{K_D}$) phases.

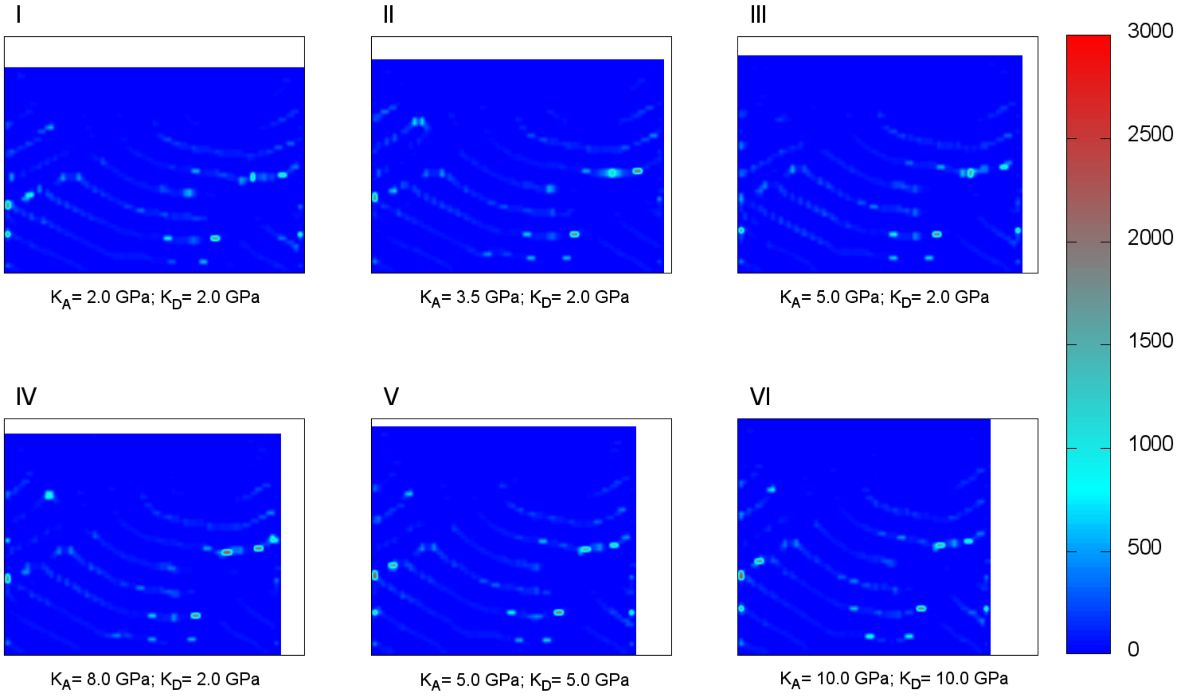

K_A= 2.0 GPa; K_D= 2.0 GPa

K_A= 3.5 GPa; K_D= 2.0 GPa

K_A= 5.0 GPa; K_D= 2.0 GPa

K_A= 8.0 GPa; K_D= 2.0 GPa

K_A= 5.0 GPa; K_D= 5.0 GPa

K_A= 10.0 GPa; K_D= 10.0 GPa

Figure A.9: Charge recombination number distribution of the strained $A_{10}D_{20}A_{10}$-triblock copolymer morphologies at mechanical load of 0.5 N/m^2 for different values of bulk moduli of acceptor ($\mathrm{K_A}$) and donor ($\mathrm{K_D}$) phases.

Appendix B

Supporting material to chapter 6

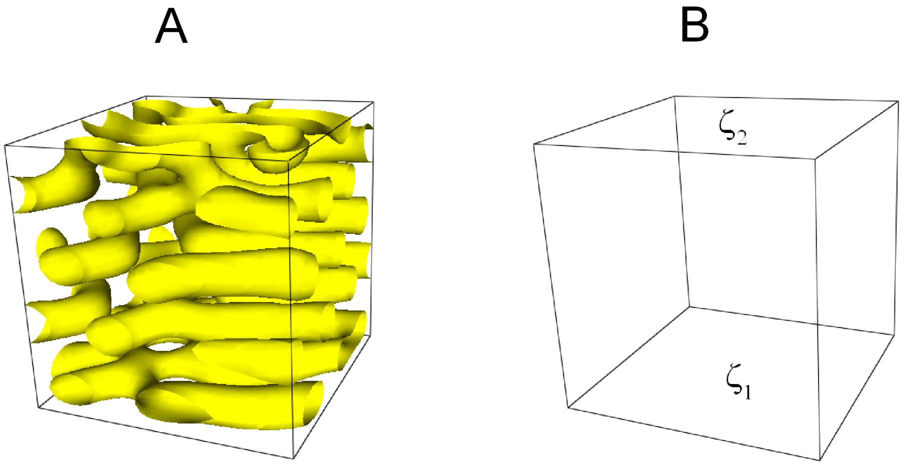

Figure B.1: (a) Morphology of $A_3D_{12}A_3$ triblock-copolymer thin film before applying an electric field with $\zeta_1 = 0.2$ to the bottom electrode and with the Neumann boundary condition for the top surface. (b) Schematic representation of the simulation box.

References

[1] L. M. Flora, N. Arokia, W. Yiliang and O. S. Beng: *Organic Thin Film Transistors Integration: A Hybrid Approach* (Wiley-VCH Verlag, Weinheim, 2011)

[2] K. Yoshino, Y. Ohmori, A. Fujii and M. Ozaki, Japanese J. Appl. Phys. **46**, 5655 (2007).

[3] O. D. Jurchescu: Large-Area Organic Electronics: Inkjet Printing and Spray Coating Techniques, in *Organic Electronics: Emerging Concepts and Technologies*, eds. F. Cicoira and C. Santato (Wiley-VCH Verlag, Weinheim, 2013)

[4] E. D. Glowacki, N. S. Sariciftci, C. W. Tang: Organic Solar Cells, in *Encyclopedia of Sustainability Science and Technology*, ed. R. A. Meyers (Springer+Business Media, New York, 2012)

[5] M. A. Green, K. Emery, Y. Hishikawa, W. Warta and E. D. Dunlop, Prog. Photovolt: Res. Appl. **22**, 1 (2013).

[6] G. Chidichimo and L. Filippelli, Int. J. Photoenergy **2010**, ID 123534 (2010).

[7] S. Donets, A. Pershin, M. J. A. Christlmaier and S. A. Baeurle, J. Chem. Phys. **138**, 094901(12) (2013).

[8] Z. M. Beiley, E. T. Hoke, R. Noriega, J. Dacuna, G. F. Burkhard, J. A. Bartelt, A. Salleo, M. F. Toney and M. D. McGehee, Adv. Energy Mater. **1**, 954 (2011).

[9] F. Yang and S. R. Forrest, Am. Chem. Soc. Nano **2**, 1022 (2008).

[10] G. A. Buxton and N. Clarke, Phys. Rev. B **74**, 085207 (2006).

[11] G. H. Fredrickson: *The Equilibrium Theory of Inhomogeneous Polymers* (Oxford University Press, New York, 2006)

[12] T. Kawakatsu: *Statistical Physics of Polymers: An Introduction* (Springer-Verlag, Berlin, Heidelberg, 2004)

[13] M. Doi and S. F. Edwards: *The Theory of Polymer Dynamics* (Oxford University Press, New York, 1998)

[14] M. W. Matsen: Self-Consistent Field Theory and Its Applications, in *Soft Matter, Volume 1: Polymer Melts and Mixtures*, eds. G. Gompper and M. Schick (Wiley-VCH, Weinheim, 2007)

[15] T. Honda and T. Kawakatsu: Computer Simulations of Nano-Scale Phenomena Based on the Dynamic Density Functional Theories: Applications of SUSHI in the OCTA System, in *Nanostructured Soft Matter, Theory, Simulation and Perspectives*, ed. A.V. Zvelindovsky (Springer-Verlag, Dordrecht, 2007)

[16] T. Honda and T. Kawakatsu, Macromolecules **39**, 2340 (2006).

[17] T. Honda, H. Kodama, J.-R. Roan, H. Morita, S. Urashita, R. Hasegawa, K. Yokomizo, T. Kawakatsu: *OCTA Integrated simulation system for soft materials: Simulation Utilities for Soft and Hard Interfaces (SUSHI). User's Manual, version 8.1* (OCTA, Nagoya, Japan, 2010)

[18] P. G. Nicholson and F. A. Castro, Nanotechnology **21**, 492001 (2010).

[19] C. Yumusak and D. A. M. Egbe: Organic Bulk Heterojunction Solar Cells Based on Poly(p-Phenylene-Vinylene) Derivatives, in *Solar Cells - New Aspects and Solutions*, ed. L. A. Kosyachenko (InTech, 2011)

[20] C. W. Tang, Appl. Phys. Lett. **48**, 183 (1986).

[21] G. Yu, J. Gao, J. C. Hummelen, F. Wudl, A. J. Heeger, Science **270**, 1789 (1995).

[22] F. C. Krebs, Sol. Energ. Mat. Sol. C **93**, 394 (2009).

[23] G. Kopp and J. L. Lean, Geophys. Res. Lett. **38**, 01706 (2011).

[24] P. Würfel: *Physics of Solar Cells: From Principles to New Concepts* (Wiley-VCH Verlag, Weinheim, 2005)

[25] American Society for Testing and Materials (ASTM) Terrestrial Reference Spectra for Photovoltaic Performance Evaluation (http://rredc.nrel.gov/solar/spectra/am1.5/).

[26] D. D. S. Fung and W. C. H. Choy: Introduction to Organic Solar Cells, in *Organic Solar Cells: Materials and Device Physics*, ed. W. C. H. Choy (Springer-Verlag, London, 2013)

[27] H. Hoppe, N. S. Sariciftci, Adv. Polym. Sci. **12**, 121 (2007).

[28] A. J. Pearson, T. Wang and D. G. Lidzey, Rep. Prog. Phys. **76**, 022501 (2013).

[29] S. Y. Leblebici, T. L. Chen, P. Olalde-Velasco, W. Yang and B. Ma, Appl. Mater. Interfaces **5**, 10105 (2013).

[30] P. Peumans, A. Yakimov and S.R. Forrest, J. Appl. Phys **93**, 3693 (2003).

[31] T. L. Benanti and D. Venkataraman, Photosynthesis Research **87**, 73 (2006).

[32] M. Casalegno, G. Raos, and R. Po, J. Chem. Phys. **132**, 094705 (2010).

[33] P. J. Hesketh and D. Misra, The Electrochemical Society *Interface*, 61 (2012).

[34] P. Atkins and J de Paula: *Physical Chemistry, 8th Edition* (Oxford University Press, New York, 2006)

[35] K. M . Molapo, P. M. Ndangili, R. F. Ajayi, G. M. Mbambisa, S. M. Mailu, N. Njomo, M. Masikini, P. Baker and E. I. Iwuoha, Int. J. Electrochem. Sci. **7**, 11859 (2012).

[36] C. Deibel, V. Dyakonov, Rep. Prog. Phys. **73**, 096401 (2010).

[37] R. G. E. Kimber: *Charge and Energy Transport in Organic Semiconductors*; (University of Bath, Bath, 2011)

[38] I. N. Hulea, H. B. Brom, A. J. Houtepen, D. Vanmaekelbergh, J. J. Kelly and E. A. Meulenkamp, Phys. Rev. Lett. **93**, 166601 (2004).

[39] S. Athanasopoulos, E. Hennebicq, D. Beljonne and A. B. Walker, J. Phys. Chem. **112**, 11532 (2008).

[40] M. R. Narayan and J. Singh, Eur. Phys. J. B **86**, 47 (2013).

[41] R. G. E. Kimber, A. B. Walker, G. E. Schrder-Turk and D. J. Cleaver, Phys. Chem. Chem. Phys. **12**, 844 (2010).

[42] K. Feron, X. Zhou, W. J. Belcher and P. C. Dastoor, J. Appl. Phys. **111**, 044510 (2012).

[43] K. Feron, W. J. Belcher, C. J. Fell and P. C. Dastoor, Int. J. Mol. Sci. **13**, 17019 (2012).

[44] T. Förster, Ann. Phys. **437**, 55 (1948).

[45] P. Ceroni, V. Balzani: Photoinduced Energy and Electron Transfer Processes, in *The Exploration of Supramolecular Systems and Nanostructures by Photochemical Techniques*, Lecture Notes in Chemistry, **78**, 21 (2012).

[46] S. C. J. Meskers, J. Hübner, M. Oestreich and H. Bässler, J. Phys. Chem. B **105**, 9139 (2001).

[47] R. R. Lunt, N. C. Giebink, A. A. Belak, J. B. Benziger and S. R. Forrest, J. Appl. Phys. **105**, 053711 (2009).

[48] F. Fennel and S. Lochbrunner, Phys. Rev. B **85**, 094203 (2012).

[49] I. A. Howard, R. Mauer, M. Meister and F. Laquai, J. Am. Chem. Soc. **132**, 14866 (2010).

[50] A. Miller and E. Abrahams, Phys. Rev. **120**, 745 (1960).

[51] N. Tessler, Y. Preezant, N. Rappaport and Y. Roichman, Adv. Mater. **21**, 2741 (2009).

[52] D. A. da S. Filho, Y. Olivier, V. Coropceanu, J.-L. Bredas and J. Cornil: Theoretical Aspects of Charge Transport in Organic Semiconductors: A Molecular Perspective, in *Organic Field-Effect Transistors*, eds. Z. Bao and J. Locklin (CRC Press, 2007)

[53] Y. H. Park, Y.-H. Kim, S. K. Kwon, I. S. Koo and K. Yang, Bull. Korean Chem. Soc. **31**, 1649 (2010).

[54] G. Grampp, Angew. Chem. Int. Ed. Engl. **32**, 691 (1993).

[55] M. Casalegno, A. Bernardi and G. Raos, J. Chem. Phys. **139**, 024706 (2013).

[56] J. J. M. van der Holst: *Three-dimensional modeling of charge transport, injection and recombination in organic light-emitting diodes*; (Eindhoven University of Technology, Eindhoven, 2010)

[57] C. Groves, R. G. E. Kimber and A. B. Walker, J. Chem. Phys. **133**, 144110 (2010).

[58] D. T. Gillespie, J. Comp. Phys. **22**, 403 (1976).

[59] D. T. Gillespie, Annu. Rev. Phys. Chem. **58**, 35 (2007).

[60] L. Meng, Y. Shang, Q. Li, Y. Li, X. Zhan, Z. Shuai, R. G. E. Kimber, and A. B. Walker, J. Phys. Chem. B **114**, 36 (2010).

[61] X. Zhan, Z. Tan, B. Domercq, Z. An, X. Zhang, S. Barlow, Y. Li, D. Zhu, B. Kippelen, and S. R. J. Marder, J. Am. Chem. Soc. **129**, 7246 (2007).

[62] U. Wolf, V. I. Arkhipov and H. Bässler, Phys. Rev. B **59**, 7507 (1999).

[63] J. J. M. van der Holst, M. A. Uijttewaal, B. Ramachandhran, R. Coehoorn, B. A. Bobbert, G. A. de Wijs and R. A. de Groot, Phys. Rev. B **79**, 085203 (2009).

[64] G. Li, R. Zhu and Y. Yang, Nature Photonics **6**, 153 (2012).

[65] A. C. Arias, J. D. MacKenzie, I. McCulloch, J. Rivnay and A. Salleo, Chem. Rev. **110**, 3 (2010).

[66] Y.-W. Su, S.-C. Lan and K.-H. Wei, Org. Photovolt. **15**, 554 (2012).

[67] Y. Sun, S.-C. Chien, H.-L. Yip, K.-S. Chen, Y. Zhang, J. A. Davies, F.-C. Chen, B. Lin and A. K.-Y. Jen, J. Mater. Chem. **22**, 5587 (2012).

[68] S.-S. Sun, C. Zhang, A. Ledbetter, S. Choi, K. Seo and J. Haliburton, Appl. Phys. Lett. **90**, 043117 (2007).

[69] A. Pershin, S. Donets and S. A. Baeurle, J. Chem. Phys. **136**, 194102 (2012).

[70] S. Sun, Z. Fan, Y. Wang and J. Haliburton, J. Mater. Sci. **40**, 1429 (2005).

[71] G. L. C. Paulus, S. Shimizu, J. T. Abrahamson, J. Zhang, A. J. Hilmer and M. S. Strano, AIChE Journal **57**, 1104 (2011).

[72] O. V. Mikhnenko, F. Cordella, A. B. Sieval, J. C. Hummelen, P. W. M. Blom and M. A. Loi, J. Phys. Chem. B **112**, 11601 (2008).

[73] F. Cordella, R. Orru, M. A. Loi, A. Mura and G. Bongiovanni, Phys. Rev. B **68**, 113203 (2003).

[74] S. R. Cowan, N. Banerji, W. L. Leong and A. J. Heeger, Adv. Funct. Mater. **22**, 1116 (2012).

[75] A. Pivrikas, G. Juska, A. J. Mozer, M. Scharber, K. Arlauskas, N. S. Sariciftci, H. Stubb and R. Osterbacka, Phys. Rev. Lett. **94**, 176806 (2005).

[76] O. G. Reid, G. E. Rayermann, D. C. Coffey and D. S. Ginger, J. Phys. Chem. C **114**, 20672 (2010).

[77] S. A. Baeurle, J. Math. Chem. **46**, 363 (2009).

[78] See http : //octa.jp/OCTA/presen/muffin_eng.pdf for information about software tool MUFFIN/Elastica within the OCTA program.

[79] S. A. Baeurle, G. H. Fredrickson and A. A. Gusev, Macromolecules **37**, 5784 (2004).

[80] M. Kaltenbrunner, M. S. White, E. D. Glowacki, T. Sekitani, T. Someya, N. S. Sariciftci and S. Bauer, Nat. Commun. **3**, 770 (2012).

[81] S. A. Baeurle, Phys. Rev. Lett. **89**, 080602 (2002).

[82] M. Doi, Macromol. Symposia **195**, 101 (2003).

[83] See http://octa.jp/ for information about OCTA program.

[84] M. C. Scharber, N. S. Sariciftci, Prog. Polym. Sci **In Press**, (2013).

[85] J. Nelson, Cur. Op. Sol. St. Mat. Sci. **6**, 87 (2002).

[86] F. Krebs and K. Norrman, Prog. Photovolt: Res. Appl. **15**, 697 (2007).

[87] C. J. Brabec, M. Heeney, I. McCulloch and J. Nelson, Chem. Soc. Rev. **40**, 1185 (2010).

[88] S. S. van Bavel, E. Sourty, G. de With and J. Loos, Nano. Lett. **9**, 507 (2009).

[89] C.-C. Lin, Y.-Y. Lin, S.-S. Li, C.-C. Yu, C.-L. Huang, S.-H. Lee, C.-H. Du, J.-J. Lee, H.-L. Chen and C.-W. Chen, Energy Environ. Sci. **4**, 2134 (2011).

[90] F. Padinger, R. S. Rittberger and N. S. Sariciftci, Adv. Funct. Mater. **13**, 85 (2003).

[91] Shou-Yuan Ma, Yu-Min Shen, Po-Ching Yang, Chao-Shuo Chen, Ching-Fuh Lin, Organic Electronics **13**, 297 (2012).

[92] A. C. Arias, N. Corcoran, M. Banach, R. H. Friend and J. D. MacKenzie, Appl. Phys. Lett. **80**, 1695 (2002).

[93] M. Campoy-Quiles, T. Ferenczi, T. Agostinelli, P. G. Etchegoin, Y. Kim, T. D. Anthopoulos, P. N. Stavrinou, D. D. C. Bradley and J. Nelson, Nature Materials **7**, 158 (2008).

[94] X. Bulliard, S.-G. Ihn, S. Yun, Y. Kim, D. Choi, J.-Y. Choi, M. Kim, M. Sim, J.-H. Park, W. Choi and K. Cho, Adv. Func. Mat. **20**, 4381 (2010).

[95] M. W. Matsen, Macromolecules **39**, 5512 (2006).

[96] A. Chervanyov and A. C. Balazs, J. Chem. Phys. **119**, 3529 (2003).

[97] T. Xu, J. Wang and T. P. Russell; In *Nanostructured Soft Matter: Experiment, Theory, Simulation and Perspectives*; Springer: Dordrecht, 2007.

[98] T. Xu, A. V. Zvelindovsky, G. J. A. Sevink, K. S. Lyakhova, H. Jinnai and T. P. Russell, Macromolecules **38**, 10788 (2005).

[99] Dung Q. Ly, T. Honda, T. Kawakatsu and A. Zvelindovsky, Macromolecules **40**, 2928 (2007).

[100] Dung Q. Ly, T. Honda, T. Kawakatsu and A. Zvelindovsky, Macromolecules **41**, 4501 (2008).

[101] Dung Q. Ly, T. Honda, T. Kawakatsu and A. Zvelindovsky, Soft Matter **5**, 4814 (2009).

[102] A. V. Zvelindovsky, G. J. Sevink, Phys. Rev. Lett. **90**, 049601 (2003).

[103] G. J. A. Sevink, A. V. Zvelindovsky, B. A. C. van Vlimmeren, N. M. Maurits, J. G. E. M. Fraaije, J. Chem. Phys. **110**, 2250 (1999).

[104] G. J. Fleer, S. M. A. Cohen, J. M. H. M. Scheutjens, T. Cosgrove, B. Vincent, *Polymers at Interfaces*; Chapman and Hall: London, 1993, p. 156.

[105] K. S. Lyakhova, A. V. Zvelindovsky and G. J. Sevink, Macromolecules **39**, 3024 (2006).

[106] T. Honda and T. Kawakatsu, J. Chem. Phys. **129**, 114904(8) (2008).

[107] M. W. Matsen, Macromolecules **45**, 2161 (2012).

[108] A. Horvat, K. S. Lyakhova, G. J. A. Sevink, R. Magerle and A. V. Zvelindovsky, J. Chem. Phys. **120**, 1117 (2004).

[109] T. Aoyagi and T. Honda, J. Chem. Phys. **117**, 8153 (2002).

[110] D. Meng and Q. Wang, J. Chem. Phys. **126**, 234902(10) (2007).

[111] C.-T. Lo, Y.-C. Chang, S.-C. Wu, C.-L. Lee, Colloids and Surfaces A: Physicochem. Eng. Aspects **368**, 6 (2010).

[112] W. L. Leong, G. C. Welch, L. G. Kaake, C. J. Takacs, Y. Sun, G. C. Bazan and A. J. Heeger, Chem. Sci. **3**, 2103 (2012).

[113] C. Guo, Y.-H. Lin, M. D. Witman, K. A. Smith, C. Wang, A. Hexemer, J. Strzalka, E. D. Gomez and R. Verduzco, Nano. Lett. **13**, 2957 (2013).

[114] I. Botiz, R.D. Schaller, R. Verduzco and S. B. Darling, J. Phys. Chem. C **115**, 9260 (2011).

[115] A. Pershin, S. Donets and S. A. Baeurle, Submitted for publication.

[116] H. Yan, S. Swaraj, C. Wang, I. Hwang, N.C. Greenham, C. Groves, H. Ade and C. R. McNeill, Adv. Func. Mater. **20**, 4329 (2010).

[117] H. Hoppe and N. S. Sariciftci, J. Mater. Res. **19**, 1924 (2004).

[118] R. A. Marsh, C. Groves, and N. C. Greenham, J. Appl. Phys. **101**, 083509 (2007).

[119] R. A. Marcus, Rev. Mod. Phys. **65**, 599 (1993).

[120] K. Seki and M. Tachiya, Phys. Rev. B **65**, 014305 (2001).

[121] P. K. Watkins, A. B. Walker, and G. L. B. Verschoor, Nano. Lett. **5**, 1814 (2005).

[122] A. Van Vooren, J.-S. Kim and J. Cornil, ChemPhysChem. **9**, 989 (2008).

[123] J. Kirkpatrick, V. Marcon, J. Nelson, K. Kremer and D. Andrienko, Phys. Rev. Lett. **98**, 227402 (2007).

[124] J. L. Bredas, D. Beljonne, V. Coropceanu and J. Cornil, Chem. Rev. **104**, 4971 (2004).

[125] A. Pershin, S. Donets and S. A. Baeurle, Polymer **55**, 1507 (2014).

[126] E. F. Valeev, V. Coropceanu, D. A. da Silva Filho, S. Salman and J.-L. Bredas, J. Am. Chem. Soc. **128**, 9882 (2006).

[127] B. Baumeier, J. Kirkpatrick, D. Andrienko, Phys. Chem. Chem. Phys. **12**, 11103 (2010).

[128] H. J. Snaith, A. C. Arias, A. C. Morteani, C. Silva and R. H. Friend, Nano. Lett. **2**, 1353 (2002).

[129] J. L. Luria, N. Hoepker, R. Bruce, A. R. Jacobs, C. Groves and J. A. Marohn, ASC Nano **6**, 9392 (2012).

[130] C. R. McNeill, H. Frohne, J. L. Holdsworth and P. C. Dastoor, Nano. Lett. **4**, 2503 (2004).

[131] T. J. K. Brenner and C. R. McNeill, J. Phys. Chem. C **115**, 19364 (2011).

[132] D. C. Coffey and D. S. Ginger, Nat. Mater. **5**, 735 (2006).

[133] Y.-Y. Noh, D.-Y. Kim, Y. Yoshida, K. Yase, B.-J. Jung, E. Lim, H.-K. Shim, R. Azumi, J. Appl. Phys. **97**, 104504 (2005).

[134] H. Hoppe, N. Arnold, N. S. Sariciftci, D. Meissner, Sol Energ Mat Sol Cells **80**, 105 (2003).

[135] S. van Bavel, E. Sourty, G. de With, K. Frolic and J. Loos, Macromolecules **42**, 7396 (2009).

[136] L. A. A. Pettersson, L. S. Roman and O. Inganäs, J. Appl. Phys. **86**, 487 (1999).

[137] G. F. Burkhard, E. T. Hoke and M. D. McGehee, Adv. Mater. **22**, 3293 (2010).

[138] C. M. Ramsdale and N. C. Greenham, J. Phys. D: Appl. Phys. **36**, L29 (2003).

[139] G. F. Burkhard, E. T. Hoke and M. D. McGehee: *Transfer Matrix Optical Modeling* (McGehee Group (Stanford Univ.), Stanford, 2011)

[140] S. Nilsson, A. Bernasik, A. Budkowski and E. Moons, Macromolecules **40**, 8291 (2007).

[141] C. R. McNeill, S. Westenhoff, C. Groves, R. H. Friend and N. C. Greenham, J. Phys. Chem. C **111**, 19153 (2007).

[142] A. C. Arias, J. D. MacKenzie, R. Stevenson, J. J. M. Halls, M. Inbasekaran, E. P. Woo, D. Richards and R. H. Friend, Macromolecules **34**, 6005 (2001).

[143] L. Meng, D. Wang, Q. Li, Y. Yi, J.-L. Bredas and Z. Shuai, J. Chem. Phys. **134**, 124102 (2011).

[144] A. Ng, Y. C. Sun, M. K. Fung, A. M. C. Ng, Y. H. Leung, A. B. Djurisic, W. K. Chan: Influence of the polymer processing conditions on the performance of bulk heterojunction solar cells, in *Organic Photonic Materials and Devices XIV*, eds. C. Tabor, F. Kajzar, T. Kaino and Y. Koike (American Institute of Physics, 2012)

[145] J. W. Jung, F. Liu, T. P. Russell and W. H. Jo, Energy Environ. Sci. **6**, 3301 (2013).

[146] W. Lee, G.-H. Kim, S.-J. Ko, S. Yum, S. Hwang, S. Cho, Y.-H. Shin, J. Y. Kim and H. Y. Woo, Macromolecules **47**, 1604 (2014).

Eidesstattliche Erklärung

Ich erkläre hiermit an Eides statt, dass ich die vorliegende Arbeit ohne unzulässige Hilfe Dritter und ohne Benutzung anderer als der angegebenen Hilfsmittel angefertigt habe; die aus anderen Quellen direkt oder indirekt übernommenen Daten und Konzepte sind unter Angabe des Literaturzitats gekennzeichnet.

Sergii Donets